Air Force Institute of Technology

AFIT Scholar

Theses and Dissertations | Student Graduate Works

3-2020

Effects of High Freestream Turbulence and Conduction on Film Cooling Effectiveness of Shaped Holes

Richard A. Macias Jr.

Follow this and additional works at: https://scholar.afit.edu/etd

 Part of the Heat Transfer, Combustion Commons

Recommended Citation

Macias, Richard A. Jr., "Effects of High Freestream Turbulence and Conduction on Film Cooling Effectiveness of Shaped Holes" (2020). *Theses and Dissertations*. 3216.
https://scholar.afit.edu/etd/3216

This Thesis is brought to you for free and open access by the Student Graduate Works at AFIT Scholar. It has been accepted for inclusion in Theses and Dissertations by an authorized administrator of AFIT Scholar. For more information, please contact AFIT.ENWL.Repository@us.af.mil.

EFFECTS OF HIGH FREESTREAM TURBULENCE AND CONDUCTION ON FILM COOLING EFFECTIVENESS OF SHAPED HOLES

THESIS

Richard A. Macias Jr., Second Lieutenant, USAF

AFIT/ENY/MS/20-M-270

DEPARTMENT OF THE AIR FORCE
AIR UNIVERSITY

AIR FORCE INSTITUTE OF TECHNOLOGY

Wright-Patterson Air Force Base, Ohio

DISTRIBUTION STATEMENT A
APPROVED FOR PUBLIC RELEASE; DISTRIBUTION UNLIMITED.

The views expressed in this document are those of the author and do not reflect the official policy or position of the United States Air Force, the United States Department of Defense or the United States Government. This material is declared a work of the U.S. Government and is not subject to copyright protection in the United States.

AFIT/ENY/MS/20-M-270

EFFECTS OF HIGH FREESTREAM TURBULENCE AND CONDUCTION ON FILM COOLING EFFECTIVENESS OF SHAPED HOLES

THESIS

Presented to the Faculty

Department of Aeronautics and Astronautics

Graduate School of Engineering and Management

Air Force Institute of Technology

Air University

Air Education and Training Command

in Partial Fulfillment of the Requirements for the

Degree of Master of Science in Aeronautical Engineering

Richard A. Macias Jr., B.S.

Second Lieutenant, USAF

March 2020

DISTRIBUTION STATEMENT A
APPROVED FOR PUBLIC RELEASE; DISTRIBUTION UNLIMITED.

AFIT/ENY/MS/20-M-270

EFFECTS OF HIGH FREESTREAM TURBULENCE AND CONDUCTION ON FILM COOLING EFFECTIVENESS OF SHAPED HOLES

Richard A. Macias Jr., B.S.
Second Lieutenant, USAF

Committee Membership:

Dr. Marc D. Polanka
Chairman

Dr. Mark F. Reeder
Member

Lt Col James L. Rutledge, PhD
Member

AFIT/ENY/MS/20-M-270

Abstract

With technological advancements allowing higher turbine temperatures, film cooling continues to be an important research area. The Film Cooling Rig (FCR) was fitted with a turbulence generator to vary freestream turbulence intensity and length scale, enabling the effects of high freestream turbulence on overall effectiveness to be studied. A cylindrical hole and laidback fan-shaped hole were investigated over a range of Advective Capacity Ratio (ACR) for freestream turbulence intensities of 2%, 10%, and 15%. For a given ACR, increasing the turbulence intensity resulted in lower overall effectiveness values due to the larger heat transfer coefficient that comes from turbulent flow. As expected, the laidback fan-shaped hole resulted in increased overall effectiveness values compared to the cylindrical hole due. This was the result of the laidback fan-shaped hole's ability to keep the coolant jet closer to the surface. Increasing Reynolds number also decreased the overall effectiveness due to the increased external heat transfer coefficient. A new equation for overall effectiveness predicted the change in overall effectiveness from increasing parameters such as the external and internal heat transfer coefficients. For a given ACR, increasing the internal heat transfer coefficient resulted in increased overall effectiveness due to the lower temperatures in the coolant channel drawing heat from the external surface. Increasing the coolant flow rate in the channel, and decreasing the temperature in the coolant channel, resulted in lower airfoil temperatures upstream and downstream of the channel due to an increase in conductive heat flux through the airfoil. Conduction in the rig caused the temperature of the coolant to dramatically increase within a short distance. This implies that in a turbine engine, the density of the coolant entering the cooling holes is significantly lower than the density in the coolant line.

Acknowledgements

I would like to start by thanking God for everything. Without him, none of this would be possible. I would like to thank Captain Ryan Lynch for making the transition from his work to mine as smooth as possible. You made it very easy for me to pick up where you left off by showing me how to run the rig, take data, and process the data. Processing the data would have been extremely confusing without the tutorial that you gave me. I would like to also thank Andrew Hatton for all of his hard work during the design phase of this process. Your CAD skills were invaluable and made building the new rig very easy. Thank you to Dr. Polanka for your guidance and support as my advisor. Even though you went to that school in Austin, I could not have asked for a better advisor. Thank you to Dr. Reeder and Lt Col Rutledge for your guidance in the classroom and for supporting this research. Thank you to the AniMaL additive manufacturing lab and AFIT model shop for all of your help getting this experiment going. This investigation would not have been possible without you. Thank you to Josh, Mike, Keith, and Jamie for all of your help inside the lab. You guys were always there to save the day if anything in the lab ever broke. Thanks to Major Thomas and Josh for helping me set up the hotwire and teaching me how to use the data acquisition system. Thank you to all my friends and family for your support during my time here at AFIT. Finally, I would like to thank my wonderful wife, Amanda, for everything that you do for me.

Richard A. Macias Jr.

Table of Contents

Page

List of Figures

Figure Page

List of Tables

List of Abbreviations

Abbreviation		Page
FCR	Film Cooling Rig	6
AFIT	Air Force Institute of Technology	6
AVH	Anti-Vortex Hole	17
SMS	Square Mesh Array of Square Bars	23
SMR	Square Mesh Array of Round Bars	23
IR	Infrared Radiaiton	27
CTA	Constant-Temperature Anemometer	32
COAL LAB	Combustion Optimization and Analysis Laser Laboratory	34
RTV	Room-Temperature-Vulcanizing	45

List of Symbols

Symbol Page

EFFECTS OF HIGH FREESTREAM TURBULENCE AND CONDUCTION ON FILM COOLING EFFECTIVENESS OF SHAPED HOLES

I. Introduction

Gas turbine engines have been used to power jet aircraft for over seventy years. The Junkers Jumo 004, the world's first successful axial turbojet, successfully powered a Messerschmitt ME 262 in 1942 [1]. With advancements in technology, the combustors in turbine engines are able to reach higher and higher temperatures. As the turbine inlet temperature increases, so does the power output of the engine [2]. While this makes high turbine inlet temperatures attractive, the limiting factor is often the durability of the turbine blades. Cooling techniques for turbine airfoils allow the airfoils to operate in environments with temperatures that exceed the allowable metal temperature [3]. Film cooling works by routing cooler compressor air internal to the airfoil and injecting the air out of small holes along the airfoil. This process both cools the internal surfaces of the airfoil and reduces the temperature of the fluid directly above the surface, decreasing the potential for convective heat transfer to occur. Freestream turbulence is one of the biggest factors that affects the effectiveness of a film cooling scheme, with the source of the freestream turbulence being the combustor that is upstream of the high-pressure turbine. The combustor produces varying levels of freestream turbulence with different turbulent scales depending on the operating condition of the turbine. This investigation used the Film Cooling Rig (FCR) at the Air Force Institute of Technology (AFIT) to investigate the effects of high freestream turbulence and conduction on the film cooling effectiveness of shaped holes.

1.1 Motivation

The constant desire to increase the power output of turbine engines demands that combustor temperatures continue to rise. This requires cooling methods to continue to advance so that the turbine blades can operate in extreme temperatures. Understanding the effects of high freestream turbulence on the film cooling effectiveness of film cooling holes allows the development of new cooling schemes that increase the operating temperature of turbine blades. Overall effectiveness is a common parameter used to measure the effectiveness of a cooling scheme. Overall effectiveness, as opposed to adiabatic effectiveness, takes into account conduction within the model and evaluates the effectiveness of both internal and external cooling methods. The inclusion of conduction within overall effectiveness results in the need to understand the impact of conduction on cooling schemes for a turbine vane. The high temperatures experienced in a typical turbine engine make it difficult to evaluate overall effectiveness at engine conditions. To evaluate overall effectiveness at lower temperatures, key non-dimensional parameters must be matched between test conditions and engine conditions so that the results can be scaled up. A true-scale turbine vane configuration with a Biot number that matches that of a typical turbine vane allows the results taken at lower temperatures to be scaled up to engine temperatures. With a matched Biot number model, the effects of internal convection, external convection, and conduction within the model can be used to predict film cooling performance at engine conditions.

Vorgert [4] performed film cooling experiments with the FCR and found that the surface temperature of the airfoil did not decrease proportionally with the coolant temperature. Vorgert theorized that the temperature of the test plate was not governed solely by the freestream and coolant, but that the heat from the test section was conducting out into the room. Vorgert [4] saw that there was a non-zero overall

effectiveness when there was no coolant flowing through the airfoil. The non-zero overall effectiveness was due to the heat flowing through the many conduction paths in the FCR. Vorgert found that with carbon dioxide as the coolant, a blowing ratio of 0.5 produced higher overall effectiveness values than a blowing ratio of 2.0. Lynch [5] sought to investigate this phenomenon by studying the internal flow within the FCR coolant channel, but leakage issues with the cooling assembly did not allow the investigation to be completed.

1.2 Objectives

This investigation had three main objectives. The first objective was to study the effects of high freestream turbulence on the overall effectiveness of film cooling holes. A sub-objective of this was to investigate the effect that the integral length scale has on the overall effectiveness. The second objective was to study the effects of Reynolds number and freestream temperature on the overall effectiveness. The third objective was to investigate the effects of internal convection within the coolant channel and how conduction through the model affects the overall effectiveness.

1.2.1 Impacts of Freestream Turbulence on Overall Effectiveness

Performing investigations at different levels of freestream turbulence intensity and different turbulent length scales allows the effects on overall effectiveness to be studied. A freestream turbulence generator was designed and installed in the FCR to study film cooling performance at various levels of freestream turbulence intensity. The turbulence generator was capable of generating a variety of freestream turbulence intensities with different integral length scales. A standard cylindrical hole and a laidback fan-shaped hole were tested at Advective Capacity Ratios ranging from 0-2.0 at freestream turbulence intensities ranging from 2% to 15% to study the effects

on overall effectiveness.

1.2.2 Impacts of Reynolds Number and Freestream Temperature on Overall Effectiveness

Flow conditions in a turbine engine vary depending on the engine's operating condition. The freestream flow rate changes the freestream Reynolds number and therefore changes the external heat transfer coefficient for the airfoil. Conducting film cooling experiments at different Reynolds numbers allows the external heat transfer coefficient to be adjusted so that the effects on overall effectiveness can be studied. The freestream flow controllers were used to produce freestream Reynolds numbers of $10k$ and $15k$ based on the airfoil's leading edge diameter. This investigation was also conducted with freestream temperatures of $450K$, $550K$, and $650K$ to study the impact of the air's thermal properties on film cooling effectiveness. Changing the freestream temperature allows different density ratios (DR) and advective capacity ratios (ACR) to be studied without changing the coolant flow rate.

1.2.3 Impacts of Internal Heat Transfer Coefficient and Conduction on Overall Effectiveness

Conduction within a test model keeps the surface temperature from becoming uniform with the freestream temperature. The surrounding metal of a test rig, and in a real turbine engine, has the effect of keeping the surface temperature lower than the freestream temperature due to the many conduction paths. This is the reason for the overall effectiveness settling at a value that is non-zero when there is no coolant flowing within the model. This investigation sought to study the effects of internal convection and conduction within the airfoil on the overall effectiveness of the cooling scheme. The airfoil used in this investigation had an internal coolant channel that was

representative of a serpentine channel found in a typical turbine blade. The effects of convection within the channel was studied by simulating extra rows of cooling holes. Simulating extra rows of cooling holes allowed the coolant flow within the passage to be increased, thus increasing the internal heat transfer coefficient, while keeping the same ACR out the holes. This allowed the impacts of internal cooling and conduction within the model on overall effectiveness to be investigated.

As previously mentioned [4], conduction paths within the rig keep the airfoil surface temperature from reaching the freestream temperature even when there is no coolant flow. This investigation compared the surface temperatures upstream of the film cooling holes for cases with no coolant flow and for cases with coolant flow To investigate the impact of axial conduction. Any changes in surface temperature, and therefore overall effectiveness, in this region were due to conduction within the airfoil because there was no external coolant upstream of the holes.

1.3 Thesis Chapter Layout

Chapter 2 reviews the relevant literature and background information about previous film cooling investigations that allowed the objectives of this investigation to be completed. Chapter 3 covers the lab setup and experimental methods used to complete this research. Chapter 4 discusses the testing performed to accomplish the objectives. Specifically, it covers the effects of high freestream turbulence on film cooling effectiveness along with the effects of Reynolds number, freestream temperature, internal heat transfer coefficients, and conduction on overall effectiveness. Lastly, Chapter 5 summarizes the findings of this investigation and provides recommendations for future work.

II. Literature Review

The Film Cooling Rig (FCR) at the Air Force Insititute of Technology (AFIT) is a true-scale rig that has been used to study the scaling of film cooling performance between ambient and elevated temperature conditions. The current research focused on studying the effect that freestream turbulence has on the film cooling effectiveness of various hole shapes over a range of freestream temperatures up to 650K. The fundamentals of film cooling must be understood before conducting research and are discussed in Section 2.1. Section 2.2 provides an overview of various film cooling parameters that are important in the current research. The effects of hole geometry on film cooling effectiveness are discussed in Section 2.3, and the effects of freestream turbulence on film cooling effectiveness are examined in Section 2.4. The fundamentals behind grid-generated turbulence, used to design a turbulence generator for the current FCR, are discussed in Section 2.5. Finally, Section 2.6 explains the measurement techniques that were used to measure temperatures and freestream turbulence levels.

2.1 Fundamentals of Film Cooling

When hot combustor air enters the turbine, heat is transferred to the airfoil through convection, as seen in Equation 1,

$$q'' = h(T_{ref} - T_s) \tag{1}$$

where q'' is the heat flux to the airfoil, h is the heat transfer coefficient, T_s is the surface temperature of the airfoil, and T_{ref} is an appropriate reference temperature. The first cooling methods for turbine blades involved routing bleed air from the compressor to the internal side of the blades. As turbine inlet temperatures increased and more

cooling was required, various methods of cooling were developed. Film cooling is one of the most common methods of cooling and involves drilling small holes into the airfoils to create a passageway for the coolant, which is typically bleed air from the compressor. As the coolant exits the holes, it creates a "film" of cooler air between the airfoil surface and the combustion gases. As seen in Figure 1, the three temperatures of interest for a film-cooled turbine airfoil are the temperature of the freestream gas, T_g, the temperature of the coolant, T_c, and the temperature of the airfoil surface, T_w [3].

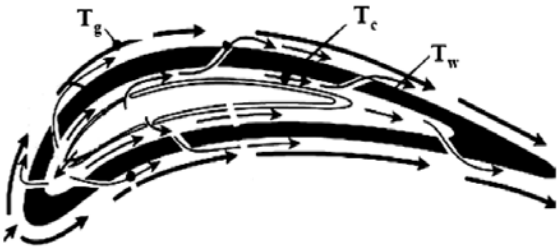

Figure 1. Diagram of a typical film-cooled turbine airfoil depicting the three temperatures of interest. Adapted from Bogard and Thole [3].

The driving factor for convective heat transfer to occur is the difference between the surface temperature and the reference temperature. As coolant exits the coolant hole and mixes with the hot freestream gas, the local fluid temperature varies along the surface of the airfoil. In Equation 1, h is a function of the flowfield and the temperatures of the coolant and the freestream. More specifically, h is determined by the Nusselt number, which is a function of the Reynolds Number and Prandtl Number [6]. The Reynolds number and Prandtl number both require properties from within the boudnary layer. These properties are functions of temperature and as a result, a temperature between the surface temperature and the temperature of the coolant should be used to evaluate the properties. To obtain a heat transfer coefficient that is accurate with the presence of film cooling, the reference temperature in Equation 1 should be the temperature of the fluid directly above the surface [3]. When doing

so, Equation 1 becomes:

$$q''_f = h_f(T_{aw} - T_s) \tag{2}$$

where T_{aw} is the adiabatic wall temperature, q''_f is the heat flux to the airfoil with film cooling present, and h_f is the heat transfer coefficient with film cooling present. The adiabatic wall temperature differs from the surface temperature in Equation 1 in that it is the temperature of the surface if the surface were adiabatic. In other words, the adiabatic wall temperature represents the temperature of the fluid directly above the surface of the airfoil if there were no heat transfer. Numerous ways have been developed to quantify the effect that cooling techniques have on the airfoil. One of these ways is the adiabatic effectiveness, η, shown in Equation 3,

$$\eta = \frac{T_\infty - T_{aw}}{T_\infty - T_{c,e}} \tag{3}$$

where $T_{c,e}$ is the temperature of the coolant at the exit of the cooling hole. The adiabatic effectiveness is a useful tool to study the effects of external cooling. Due to the adiabatic effectiveness being a non-dimensional temperature, η has a value between 0 and 1, with larger values indicating an improved cooling performance.

Although the adiabatic effectiveness is a useful way of evaluating the performance of an external cooling scheme, it does not accurately assess the performance of cooling schemes for real engine parts. Real engine components are not adiabatic, and the surfaces have temperature gradients. In a real engine component, there are multiple ways for heat transfer to occur. Figure 2 shows the paths for heat transfer in a real engine component. External convection occurs as the freestream gasses, with velocity U_∞ and temperature T_∞, travel along the external surface of the airfoil, with temperature $T_{w,e}$. There is also internal convection as the coolant, with velocity U_c

and temperature T_c, travels along the internal surface of the airfoil, with temperature $T_{w,i}$. In addition to the internal convection and external convection, there is convection within the cooling holes, conduction within the surface, and radiation exchange between the surface and its surroundings.

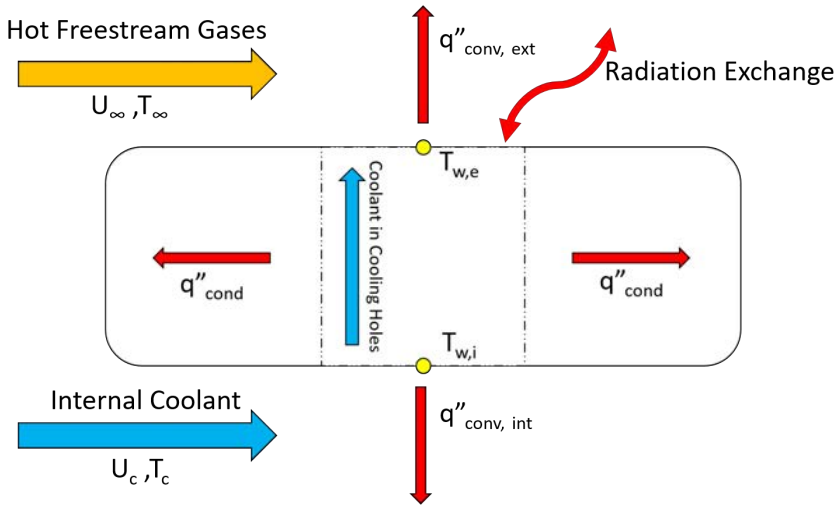

Figure 2. Modes of heat transfer in a cooled engine component.

To capture these additional heat transfer paths, a commonly used measurement of film cooling performance is the overall effectiveness, ϕ, as seen in Equation 4,

$$\phi = \frac{T_\infty - T_s}{T_\infty - T_{c,i}} \tag{4}$$

where $T_{c,i}$ is the temperature of the coolant before entering the film-cooling holes. The overall effectiveness, also referred to as the nondimensional surface temperature, takes into account all three cooling methods: external cooling, internal cooling, and convection within the cooling holes [7]. The overall effectiveness normalizes the difference between the freestream temperature and the surface temperature by the difference between the freestream temperature and the internal coolant temperature. Using the internal coolant temperature acknowledges the fact that the coolant entering the coolant hole is not at the same temperature as the coolant exiting the coolant

hole.

The surface temperature of the airfoil is a function of both the external convective boundary conditions and the internal cooling arrangement [8]. As a result, an energy balance between the convective heat flux and the conduction through the material is required to properly analyze the surface temperature. Following the derivation found in Rutledge et al.[8], an alternate expression for the overall effectiveness can be developed:

$$\phi = \frac{\chi\eta(Bi + \frac{h_f}{h_c}) + 1}{\frac{h_f}{h_c} + Bi + 1} \tag{5}$$

This version takes into account the Biot number, Bi, the adiabatic effectiveness, the coolant warming factor, χ, and the ratio of external to internal heat transfer coefficients, $\frac{h_f}{h_c}$. This equation shows that the overall effectiveness will be matched between experimental and engine conditions if the Biot number, adiabatic effectiveness, and the ratio of external to internal heat transfer coefficients are also matched [9]. This can be used to predict how a cooling scheme, tested at low freestream temperatures, will perform at engine conditions. The Biot number is shown in Equation 6

$$Bi = \frac{h_f L}{K_w} \tag{6}$$

where L is the thickness of the wall, and K_w is the thermal conductivity of the wall.

2.2 Film Cooling Parameters

The high temperatures that are experienced at engine conditions make it difficult to investigate the effectiveness of film cooling techniques. This has led to experiments being conducted at lower temperatures, with the results being scaled up to engine conditions with the use of non-dimensional parameters. The first important param-

eter to mention is the mass flux ratio, M, also referred to as the blowing ratio. The blowing ratio is shown in Equation 7, where ρ_c is the coolant density, U_c is the coolant velocity, ρ_∞ is the freestream density, and U_∞ is the freestream velocity.

$$M = \frac{\rho_c U_c}{\rho_\infty U_\infty} \tag{7}$$

It should be noted that the blowing ratio is the product of the density ratio (DR) and the velocity ratio (VR), shown in Equations 8 and 9, respectively.

$$DR = \frac{\rho_c}{\rho_\infty} \tag{8}$$

$$VR = \frac{U_c}{U_\infty} \tag{9}$$

Another common parameter is the momentum flux ratio, I, shown in Equation 10. The momentum ratio has a strong effect on the effectiveness because it determines whether or not the coolant jet will fully separate from the surface.

$$I = \frac{\rho_c U_c^2}{\rho_\infty U_\infty^2} \tag{10}$$

Coolant jets tend to separate from the surface downstream of the cooling holes, and then either reattach or stay separated. A study by Thole et al.[10] measured the thermal profiles along the centerline of cooling jets to examine the coolant distribution along the surface. For $I < 0.4$, the jets stayed fully attached to the wall. For $0.4 < I < 0.8$, the jets initially separated and then reattached further downstream. For $I > 0.8$, the jets separated and then never reattached [10].

Jet separation and cooling effectiveness are also effected by the density ratio. Eberly and Thole [2] conducted film-cooling studies at low and high density ratios. While both the high density ratio and low density ratio jets both detached as the

blowing ratio and momentum ratio increased, the low density ratio tests showed more blowoff than the high density ratio tests [2]. Their study also showed that for a given blowing ratio, test cases with higher density ratios resulted in increased spreading of the coolant. As a result of the increased spreading, the adiabatic effectiveness tended to increase. In a typical turbine engine, the density ratio is usually around two [3].

It is important to note that if the density ratio is not matched, the blowing ratio and momentum ratio cannot be simultaneously matched. Matching the density ratio that is typically found at engine conditions is often hard to achieve in an experimental setting, meaning that a choice between matching I and matching M has to be made.

Previous experiments have put much effort into matching density ratio to scale results from experimental conditions to engine conditions, but matching density ratio may not be the answer to scaling. Rutledge and Polanka [11] studied the effects of matching the Reynolds Number Ratio and a new parameter defined by the authors as the Heat Capacity Ratio, now known as the Advective Capacity Ratio (ACR). The Advective Capacity Ratio, shown in Eq. 11, includes the ratio of specific heats between the coolant and the freestream. Results showed that thermal properties can play an important role in matching film cooling results. While they showed that density effects still dominate film cooling performance, variations in conductivity and heat capacity, c_p, resulted in changes in excess of 10% in the heat flux to the surface when scaling from experimental conditions to near-engine conditions [11].

$$ACR = \frac{c_{p_c}\rho_c U_c}{c_{p_\infty}\rho_\infty U_\infty} \tag{11}$$

Wiese et al. [12] compared ϕ distributions for different coolant gases with a variety of different properties and found that the heat capacity of the coolant influenced the temperature distribution of the coolant. This affected the adiabatic effectiveness and set the driving temperature for the heat transfer into the surface. They also showed

that the thermal conductivity of the external coolant influenced the amount of heat that was transferred into the surface from the freestream [12].

Fischer et al. [13] measured adiabatic effectiveness on a flat plate with a single 7-7-7 hole and used several coolant gases to obtain a wide range of property variations. Results showed that ACR scaled adiabatic effectiveness results for cases when the coolant jet was fully attached ($I < 0.5$). For larger values of I, ACR became less effective at scaling η due to coolant jet separation. The inclusion of c_p allows ACR to account for the coolant's ability to cool the surface, and was what resulted in matched η profiles [13]. This is significant due to the fact that in a real engine, the specific heat of the coolant is significantly lower than that of the freestream gas.

Contour plots of η for a blowing ratio of 0.25, shown in Figure 3, reveal noticeably different levels of effectiveness for each gas. Using Helium, the gas with the highest specific heat, as a coolant produced higher η values than the other three gases, with Argon, the gas with the lowest specific heat, performing the worst. This reinforces the need to account for the specific heat of the coolant.

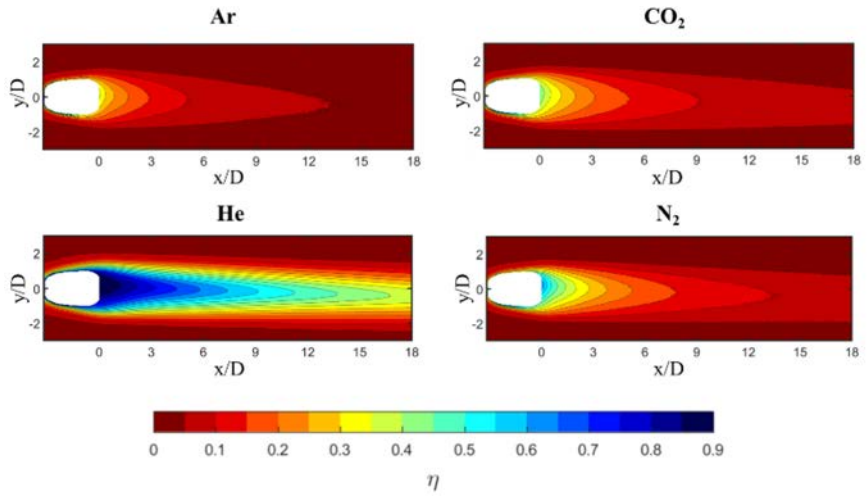

Figure 3. Contours of η at $M = 0.25$, $Tu = 0.67\%$ [13]

Contour plots of η for the four gases with a matched ACR are shown in Figure 4. Comparing the contours to Figure 3 reveals the superiority of the scaling capability

of ACR compared to M [13]. Even though each gas had a different specific heat, matching ACR resulted in matched adiabatic effectiveness contours for the four gases.

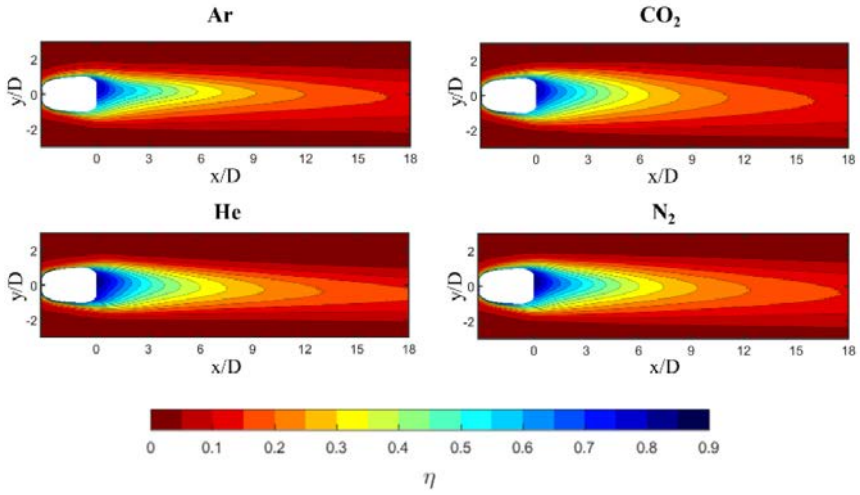

Figure 4. Contours of η at $ACR = 0.50$, $Tu = 0.67\%$ [13]

Further tests revealed that ACR will almost exactly scale adiabatic effectiveness results for cases when the coolant jet is fully attached ($I < 0.5$). Figure 5 shows area-averaged adiabatic effectiveness plotted against ACR for all data points collected by Fischer et al. [13]. For the low ACR values, all of the data points followed the same curve until the effectiveness values for each gas started to stray from the trend. The dashed arrows indicate the momentum ratio where each gas started to deviate from the trend. For larger values of I, ACR became less effective at scaling η due to coolant jet separation. These results showed that accurate predictions of η can be made for low values of I without matching the density ratio [13].

2.2.1 Scaling Overall Effectiveness

As mentioned in Section 2.1, overall effectiveness will be matched between test and engine conditions if the Biot Number, adiabatic effectiveness, and ratio of external to internal heat transfer coefficients are matched. Polanka et al. [14] measured the overall effectiveness on a full-scale metallic vane ring at low temperatures, and cor-

rected the data to engine conditions. The data showed that the expected ϕ values at engine-representative temperatures were within 3% of the experimental ϕ values when the Biot numbers were matched within 25%. This result shows that the Biot numbers do not have to be exactly matched to accurately simulate an engine's environment at experimental conditions [14].

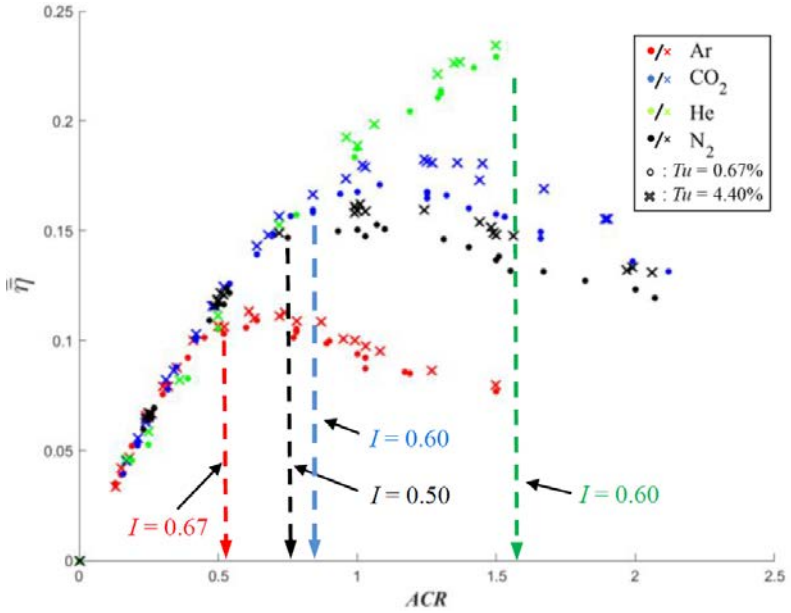

Figure 5. Area-averaged adiabatic effectiveness vs. ACR for all test cases [13].

2.3 Effects of Hole Geometry

The geometry of the cooling hole is a factor that affects the film cooling effectiveness. Gritsch et al. [15] measured the film cooling effectiveness for a cylindrical hole, a fanshaped hole, and a laidback fanshaped hole. The three hole geometries are shown in Figure 6. The study revealed that the two fanshaped holes provided significantly more thermal protection of the surface downstream of the hole exit [15], shown by the η contours in Figure 7. The contours show that the laidback fanshaped hole provided more lateral spreading of the coolant jet than the fanshaped hole. As a result of the increased spreading, the laidback fanshaped hole resulted in increased

laterally averaged adiabatic effectiveness [15].

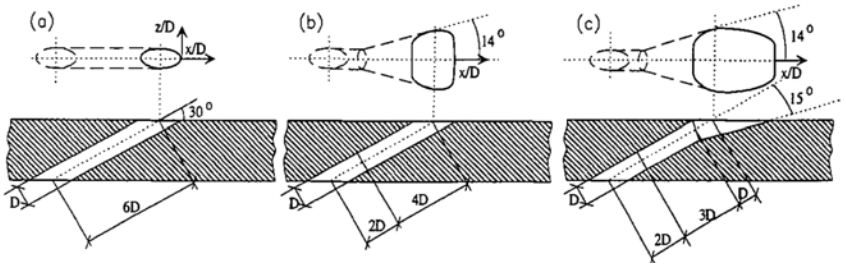

Figure 6. The three hole shapes studies by Gritsch et al. [15]: cylindrical, fanshaped, and laidback fanshaped.

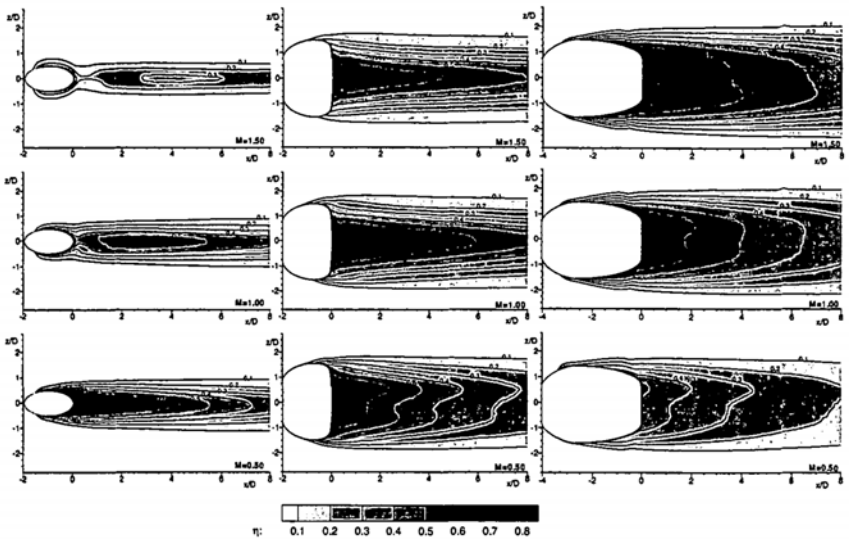

Figure 7. Adiabatic effectiveness contours for the cylindrical, fanshaped, and laidback fanshaped hole [15].

Schroeder and Thole [16] offered the film cooling community a shaped hole design to serve as a baseline hole shape. With a widely accepted baseline hole, future experiments would have the same reference to compare data to. The baseline hole, referred to as the 7-7-7 hole, is shown in Figure 8 and is expanded seven degrees in each lateral direction and laidback seven degrees. A full description of the hole geometry is shown in Table 1.

Two issues with standard hole geometries are the liftoff that occurs as the coolant jet exits the cooling hole and the formation of vortices that entrain the hot freestream

gas along the airfoil surface [17]. These kidney-shaped vortices, shown in Figure 9, rotate in such a way that one vortex lifts the other off the surface [18]. The combination of the coolant liftoff and the gas entrainment degrades the effectiveness of a cooling scheme. Shaped holes and multi-hole designs are used to reduce the strength of the vortices and decrease the coolant jet velocity out of the hole by increasing the exit area, reducing the jet liftoff [17].

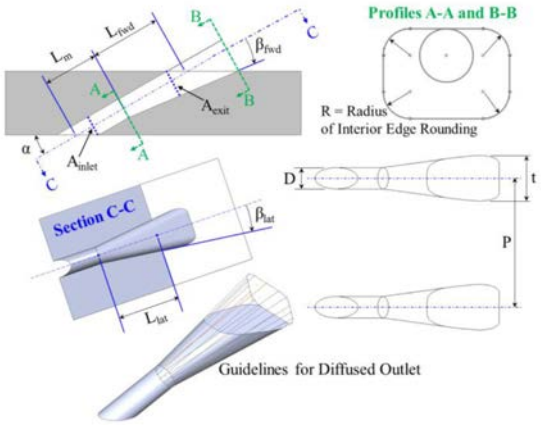

Figure 8. Baseline 7-7-7 hole design [16].

Table 1. Geometric parameters for 7-7-7 hole [16].

	Range Common in Literature	7-7-7 Shaped Hole
Injection Angle, α	30 to 55°	30°
L_m/D	1 to 4	2.5
L_{lat}/D, L_{fwd}/D	1.6 to 9.5	3.5
L/D	2.8 to 11.5	6
Laidback Angle, β_{fwd}	2 to 25°	7°
Lateral Angle, β_{lat}	2 to 18°	7°
P/D	2.8 to 8	6
Coverage Ratio, t/P	0.3 to 0.8	0.35
Area Ratio, AR	2.5 to 4.7	2.5
Sharpness of Inlet and Breakout Edges	Usually Sharp	Sharp
Rounding of Four Edges Inside Diffuser, R/D	0 to 0.5	0.5

Hayes et al. [17] investigated the effectiveness of a multi-hole concept, the anti-vortex hole (AVH). The AVH, shown in Figure 10, consists of a main cooling hole with two sister holes that branch out from the main hole [17]. Heidmann and Ekkad [19]

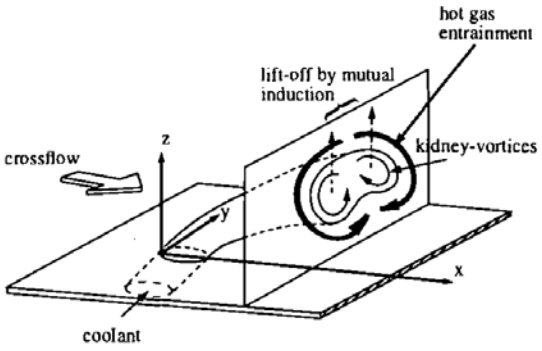

Figure 9. Kidney-shaped vortices that form as a result of the interaction between the coolant jet and the freestream gas [18].

computationally compared heat transfer coefficients and film effectiveness values for the AVH and cylindrical hole configuration. The AVH configuration showed improved film-cooling performance for a blowing ratio of 1.0 on a flat plate compared to a standard cylindrical hole. Computational fluid dynamics predicted an improvement in area-averaged film effectiveness of about 0.2 and a net heat flux reducion (NHFR) of about 0.2 for the AVH when compared to the round hole for density ratios of 1.0 and 2.0 [19].

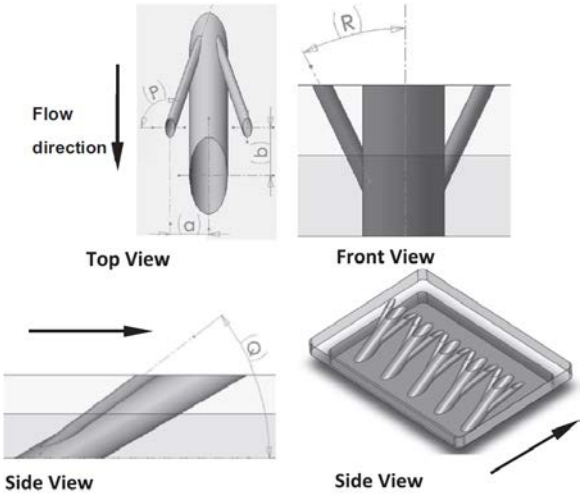

Figure 10. Example drawing of an AVH configuration [20].

2.4 Effects of Freestream Turbulence on Film Cooling Effectiveness

Freestream turbulence is one of the most dominating effects on film-cooling performance [3]. The source of the freestream turbulence is the combustor, with the turbulence level and turbulent eddy size varying with the turbine operating condition. The turbulence level of the freestream is quantified by the root-mean-square velocity, u_{rms}, divided by the magnitude of the mean velocity, U.

$$Tu = \frac{u_{rms}}{U} \tag{12}$$

Representative turbulence intensities for gas turbine engines are around twenty percent [3]. Several studies have been conducted with non-reacting and reacting combustors to investigate the freestream turbulence characteristics exiting the combustor. Ames and Moffat [21] experimentally studied turbulence in a non-reacting combustor simulator and measured turbulence intensity levels up to 19%. Cameron et al. [22] studied swirl-driven inlet flow in reacting combustors and measured turbulence levels near 25%.

The turbulent length scales are quantified by measurements of the integral length scale, which is a measure of the largest turbulent length scale. A common way to calculate the integral length scale is to first calculate the integral time scale, the interval between statistically uncorrelated samples, and then use Taylor's frozen hypothesis to switch from a time scale to a length scale. The integral time scale can be computed from the autocorrelation function, shown in Equation 13:

$$\rho(s) = \frac{< u(t)u(t+s) >}{< u(t)^2 >} \tag{13}$$

where $u(t) = U(t) - U$ is the fluctuation, $< u^2 >$ is the variance, and $< u(t)u(t+s) >$ is the autocovariance [23]. The autocorrelation function, the correlation coefficient

between a function at times t amd $t+s$, starts at a value of one and diminishes. The autocorrelation function usually decreases rapidly enough that the integral converges and the integral time scale, τ, is [23]:

$$\int_0^\infty \rho(s)ds \tag{14}$$

The effect of freestream turbulence on film cooling effectiveness depends on the momentum flux ratio of the coolant. Schmidt and Bogard [24] ran experiments with a DR of two, typical of a real turbine engine, and measured heat transfer coefficients and adiabatic effectiveness for freestream turbulence levels of 0.3%, 10%, and 17%. They found that for low to moderate momentum flux ratios, $0.1 < I < 0.5$, high freestream turbulence reduced the adiabatic effectiveness by more than 50% at the cooling hole. The decrease in effectiveness was worse as the downstream distance from the hole increased. This decrease in adiabatic effectiveness at the cooling hole was a result of the increased external heat transfer coefficient, which increased the heat flux to the airfoil, and the increased lateral dispersion of the coolant. Figure 11 shows lateral effectiveness values at three downstream distances for $I = 0.5$. At zero lateral distance from the hole, $z/D = 0$, the adiabatic effectiveness decreased as Tu increasesd for each downstream distance. At $x/D = 10$, the increase in lateral dispersion due to increased Tu is indicated by the increase in η away from the jet center [24].

For large momentum flux ratios, $I > 1$, Schmidt and Bogard observed that the trend reversed and the high freestream turbulence levels caused the adiabatic effectiveness to increase [24]. Figure 12 shows laterally averaged adiabatic effectiveness versus momentum flux ratio at three downstream distances from the cooling hole. The laterally averaged values of η are higher for the high freestream turbulence cases when $I > 1$. The coolant jets normally detach for these momentum flux ratios, so the high

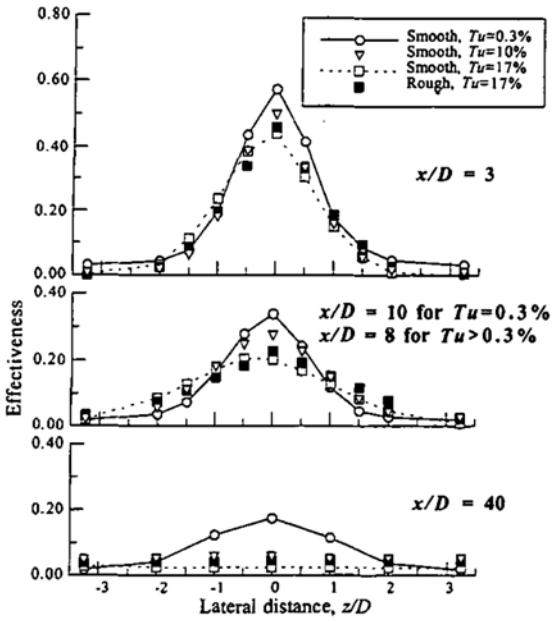

Figure 11. Freestream turbulence effects on lateral adiabatic effectiveness at $I = 0.5$, $M = 1.0$ [24].

freestream turbulence levels either resulted in less detachment of the jet or caused the detached coolant to move back to the surface [24]. The optimum range of momentum flux ratio for the low freestream turbulence levels was found to be $0.1 < I < 0.5$, while the optimum range of momentum flux ratio for the high freestream turbulence levels was found to be $1 < I < 2$ [24].

Hayes et al. [17] studied the film cooling effectiveness by varying blowing ratio and freestream turbulence intensity for a conventional straight hole and an AVH. The data showed improved cooling performance for the AVH compared to the straight hole at low levels of freestream turbulence intensity. The data also showed that high levels of freestream turbulence intensity improved the cooling performance of the AVH. For all turbulence levels tested, increasing the blowing ratio resulted in improved film cooling effectiveness [17].

Schroeder and Thole [16] measured adiabatic effectiveness at different levels of freestream turbulence for a laidback fanshaped hole and found that increasing the

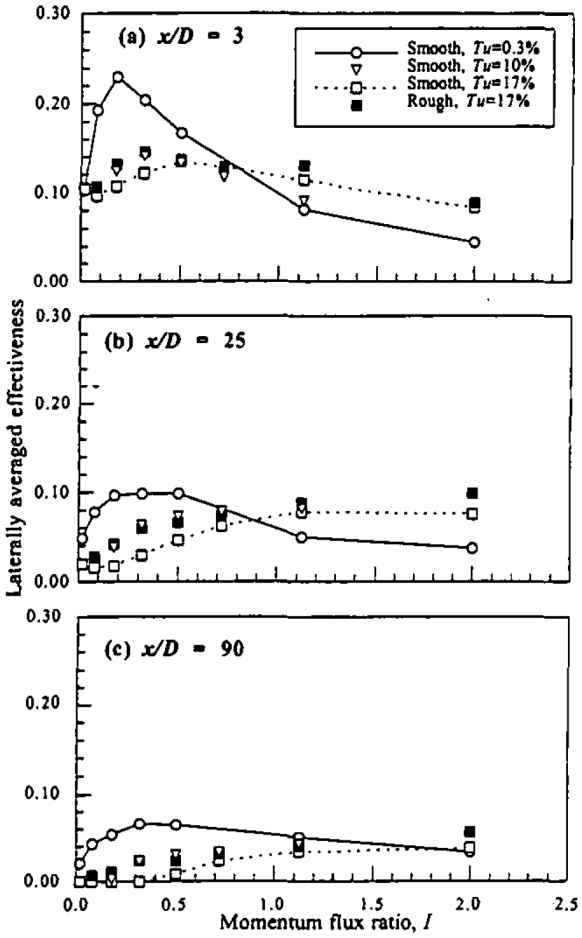

Figure 12. Freestream turbulence effects on laterally averaged adiabatic effectiveness as a function of I [24].

freestream turbulence from 0.5% to 5% resulted in an approximate 50% widening of the coolant jet for blowing ratios of 2.0 and 3.0. They also found that area-averaged adiabatic effectiveness decreased as much as 10% for blowing ratios of 0.5 and 1.0. [16].

2.5 Grid-Generated Turbulence

High levels of freestream turbulence are guaranteed to be present in a real engine, resulting in a desire to produce realistic levels of freestream turbulence in lab environments. There are many ways of generating freestream turbulence. In most

experimental configurations, freestream turbulence is generated using a biplanar grid of bars, where the eddies are on the order of the size of the bars [3]. Various levels of Tu, including low levels, must be generated to effectively study the effects of freestream turbulence.

A common way of generating different levels of freestream turbulence is by using a combination of screens and honeycombs. Screens can be used for the production of high Tu levels and low Tu levels [25]. The geometry of the screen can be modified by changing the pattern of the screen or by changing the dimensions of the pattern elements. Screen dimensions are normally defined by the solidity ratio, S, shown in Equation 15

$$S = 1 - A_o/A_t \tag{15}$$

where A_o is the open area of the screen and A_t is the total area of the screen. A solidity ratio of zero corresponds to no screen at all, while a solidity ratio of one corresponds to a solid plate. Two common types of screens are the square mesh array of square bars (SMS), and the square mesh array of round bars (SMR). Two important characteristics of the grids, shown in Figure 13, are the rod size, b, and the space between the rod centers, M.

In their investigation of flow through screens, Baines and Peterson [25] studied the characteristics of screen-generated turbulence. They examined seven SMS screens, each with different values of M and b. They found that the flow downstream of a screen displayed a region of flow establishment and a region of established flow. In the region of flow establishment, the anisotropic turbulence generated from each grid cell diffused inward toward the centerline and outward toward the neighboring jets. In the next region, the flow was established and exhibited isotropic turbulence decay. Figure 14 is a plot of turbulence intensity versus downstream distance from the screen and

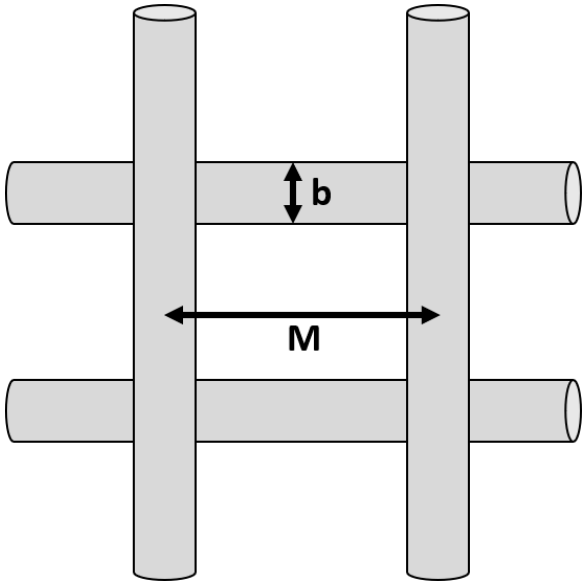

Figure 13. Example square-mesh array of round bars.

shows the two regions mentioned. The turbulence intensity rose in the region of flow establishment, labeled region A, and then decayed in the region of established flow, labeled region B. These results are in line with jet diffusion theory because screens are modeled as a series of neighboring jets [25]. Another useful takeaway from Figure 14 is the curve fit for the region of established flow. The curve fit is a powerful tool that allows the turbulence intensity downstream of a screen to be estimated if b and the downstream distance, x, are known. This is useful when designing ways to generate various levels of freestream turbulence intensity for an experimental setup.

Roach [26] conducted a similar experiment with several types of grids, including SMS grids and SMR grids. The SMS data, shown in Figure 15, closely lined up with Baines and Peterson. The difference between the two curve fits is the constant in front of the exponential term, which is less than one percent different. This reinforces the idea that these curve fits can be used to predict Tu downstream of screens.

Roach conducted the same experiment with SMR grids and compared the generated turbulence to that of the SMS grids. Figure 16 shows that Tu decayed at the same rate for both types of grids. The difference in the curve fits is the constant in

front of the equation.

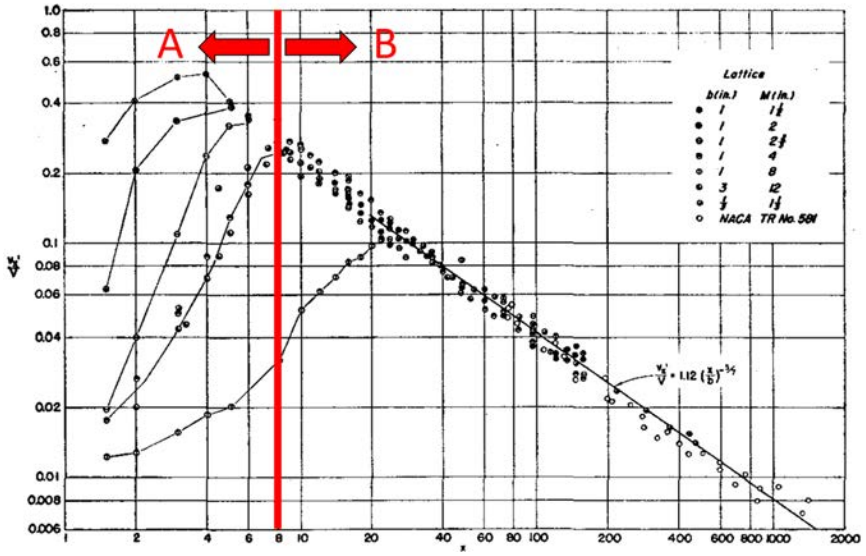

Figure 14. Decay of turbulence intensity downstream of SMS grids. Adapted from Baines and Peterson [25]. Curve fit: $Tu = 1.12(x/b)^{-5/7}$

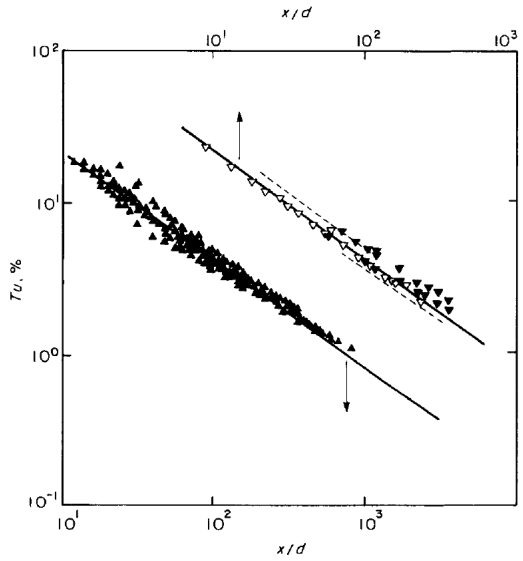

Figure 15. Decay of turbulence intensity downstream of SMS Grids. Curve fit: $Tu = 1.13(x/d)^{-5/7}$ **[26].**

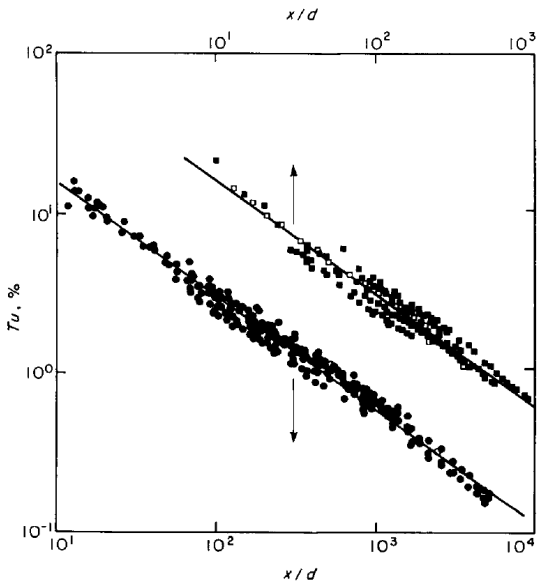

Figure 16. Decay of turbulence intensity downstream of SMR grids. Curve fit: $Tu = 0.8(x/d)^{-5/7}$ **[26].**

2.5.1 Honeycombs

Honeycombs are useful devices that straighten the incoming flow, suppress the intensity of incoming turbulence, and generate new turbulence with length scales characteristic of the shear layers present in the near wake [27]. The suppression of the incoming turbulence is due to the constraint of the lateral components of the fluctuating velocity, while the new turbulence is due to shear layer instabilities and growing turbulent Reynolds stresses. Loehrke and Nagib [27] used hot wire anemometry to study the effects of honeycombs of different lengths on freestream turbulence. They determined that the turbulence generated by honeycombs dissipates rapidly, resulting in a net suppression of the freestream turbulence intensity. They also showed that "the level, structure, and decay of the turbulence downstream of the honeycomb can be easily modified by placing a fine mesh screen in close proximity downstream of it" [27]. Their results showed that the optimum way to suppress freestream turbulence levels is by using a combination of honeycombs and screens, with the first screen positioned near the downstream end of the honeycomb [27].

2.6 Measurement Techniques

This section discusses measurement techniques that have been used in FCR research. Infrared thermography, discussed in Section 2.6.1, is a useful non-intrusive technique for measuring surface temperatures and determining ϕ. Hotwire anemometry, discussed in Section 2.6.2, was used to measure the intensity and length scales of the freestream turbulence.

2.6.1 Infrared Thermography

Infrared Thermography is an important meaurement technique because it allows a temperature measurement to be taken without being intruding into the test environment. Whereas thermocouples must be physically touching the target object and can affect the conduction heat transfer, Infrared Radiation (IR) cameras measure temperature without ever touching the target object. This is important in film cooling because any disturbance to the freestream flow or coolant flow can affect the film cooling effectiveness.

2.6.1.1 Basics of Infrared Thermography

Infrared radiation is not visible to the human eye and covers the portion of the electromagnetic spectrum from wavelengths of about 0.9 μm to wavelengths of about 14 μm. IR cameras convert infrared radiation to a visible image that depicts thermal variations across an object or scene [28]. Any object that has a temperature above absolute zero emits thermal radiation. As seen in Eq. 16, the amount of radiation emitted increases as the temperature of the object increases. E_b is the blackbody emissive power, σ is the Stefan-Boltzmann constant and has a value of $5.67*10^{-8}\frac{W}{m^2K^4}$, and n is the refractive index of the medium. The refractive index of the medium is very close to one for air and is oftentimes left out of the equation when air is considered.

$$E_b(T) = n^2 \sigma T^4 \tag{16}$$

A blackbody is an ideal object for several reasons. Blackbodies absorb and emit radiation diffusely, meaning that the amount of thermal energy released and absorbed by a blackbody is independent of direction. The radiation absorbed by a blackbody is also independent of the wavelength of the absorbed radiation. Finally, due to the combination of these aspects, no object can emit more energy than a blackbody for a specified temperature and wavelength [29]. This is an important idea when taking thermal measurements with an IR camera and is discussed in more depth later this section.

By the definition of a blackbody, real surfaces always have a lower emissive power than blackbodies. For a real surface, the Stefan-Boltzmann law becomes:

$$E(T) = \epsilon E_b(T) \tag{17}$$

where ϵ is the emissivity of a real body, or the ratio of the total emissive power of a real surface to the total emissive power of a blackbody at the same temperature [6].

When a surface is impacted by thermal radiation, the irradiation can be reflected, absorbed, or transmitted by the surface. The reflectance, ρ, is the ratio of the reflected part of the incoming radiation to the total incoming radiation. The absorptance, α, is the ratio of the absorbed part of the incoming radiation to the total incoming radiation. The transmittance, τ, is the ratio of the transmitted part of the incoming radiation to the total incoming radiation. As seen in Eq. 18, the above definitions and the conservation of energy dictate that the sum of these parts be equal to unity.

$$\rho + \alpha + \tau = 1 \tag{18}$$

The sum of the emitted radiation and reflected radiation for a surface is known as the radiosity, J, and is the total amount of radiation leaving a body,

$$J = \epsilon E_b(T) + \rho H \tag{19}$$

where H represents the irradiation hitting a surface. This is important because the IR camera only measures the radiosity. The amount of radiation that the camera detects coming off of the target object consists of the radiation emitted by the object and the radiation from outside sources that has been reflected off of the object.

The main components of an IR camera are the lens, the detector, and the electronics/software. The lens focuses the IR onto the detector, which consists of a focal plane array (FPA) of pixels. The pixels are usually one micrometer in length and are made of materials that are sensitive to IR wavelengths [28].

When IR travels from an object to the camera, the IR is attenuated by the atmosphere. The atmosphere attenuates the radiation by scattering the particles and absorbing some of the radiation. Just as clouds and fog limit how well we see objects that are far away, the same thing happens to infrared radiation. The atmosphere can affect a temperature measurement by limiting the amount of thermal radiation that is emitted by an object from reaching the camera lens. If the attenuation is not taken into account, then the camera will measure the object at a lower temperature than it actually is. The software built into most IR cameras accounts for the attenuation by the atmosphere [28].

The radiation that hits the lens of an IR camera consists of three different sources: emission from the target object, radiation reflected off of the surface of the target object, and emission from the medium between the target object and the camera. With this in mind and denoting I as the radiation power seen by the camera [28], the total radiation power received by the lens can be written as:

$$I_{tot} = \epsilon * \tau_{atm} * E_{b,obj} + \rho_{obj} * \tau_{atm} * E_{b,amb} + (1 - \tau_{atm}) * E_{b,atm} \tag{20}$$

where τ_{atm} is the transmissivity of the atmosphere, ϵ is the emissivity of the target object, $E_{b,amb}$ is the effective emissive power of the object's surroundings, $E_{b,atm}$ is the emissive power of the atmosphere, and I_{tot} is the total radiation detected by the IR camera. If the emissivity of the object, the transmissivity of the atmosphere, the effective temperature of the object's surroundings, and the temperature of the atmosphere are all inputted into the IR camera software, the $E_{b,obj}$ can be determined. By using Eq. 16, the temperature of the object can then be determined [28].

It is important to note that the accuracy of the temperature measured by the camera is extremely dependent on the properties listed above. If the camera is not using the right values of emissivity, transmissivity, and reflectivity, then the temperature measurement will be inaccurate. For this reason, it is common to paint an object with black paint when using an IR camera to record its temperature. This is done to create an object that is nearly a blackbody because blackbodies are perfect absorbers and perfect emitters. As a result of Eq. 18, blackbodies do not reflect radiation. Painting the surface of the object black limits the amount of radiation that is reflected off of the object, allowing the camera to acquire a more accurate measurement of the radiation being emitted by the object. The surroundings can also be painted black for the same reasons. Limiting the amount of radiation that is reflected off of the surroundings will further increase the accuracy of the target object's emitted radiation counts [28].

2.6.1.2 IR Camera Calibration Methods

As a result of the many sources of radiation that must be accounted for to achieve an accurate measurement of an object's temperature, it is often easier to calibrate

the IR camera with the use of embedded thermocouples. The embedded thermcouples provide reference temperatures to compare the radiation counts to, and allow a relationship between radiation counts and surface temperature to be established. Martiny et al. [30] used Planck's law, shown in Equation 21, to relate the spectral infrared radiation and the temperature of an object.

$$q"(\lambda) = \epsilon(\lambda)\frac{c_1\lambda^{-5}}{e^{\frac{c_2}{\lambda T}}-1} \tag{21}$$

where λ is the wavelength, and c_1 and c_2 are constants. If the emissivity and wavelength are known, the temperature could then be directly solved for:

$$T = \frac{c_2/\lambda}{ln(\frac{\epsilon(\lambda)*c_1*\lambda^{-5}}{q"+1})} \tag{22}$$

Martiny et al. [30] suggested the use of an empirical relationship based off of Planck's law. The relationship that they came up with, shown in Equation 23, directly relates the radiation detected by the IR camera, I, to the temperature of the object.

$$I = \frac{R}{e^{B/T} - F} \tag{23}$$

Rearranging to solve for T gives:

$$T = \frac{B}{ln(R/I + F)} \tag{24}$$

where R, B, and F can be determined by solving a non-linear system of three equations [30].

A different in-situ calibration method has been used several times in AFIT's FCR [5, 31]. This method uses the relationship between radiative heat flux and the temperature of an object, as seen in Equation 17. Like the previously discussed technique,

this method uses an IR camera and thermocouples to establish a relationship between the radiation hitting the radiation sensor and the temperature of the surface. As a result of the fourth-order nature of radiative heat transfer, the relationship is:

$$T = aJ_{rad}{}^{1/4} + b \tag{25}$$

where J_{rad} is the radiosity coming off of the object, and a and b are constants. These constants are determined by a curve fit that is produced from data collected at different surface temperatures. A sample IR calibration curve is shown in Figure 17 [31].

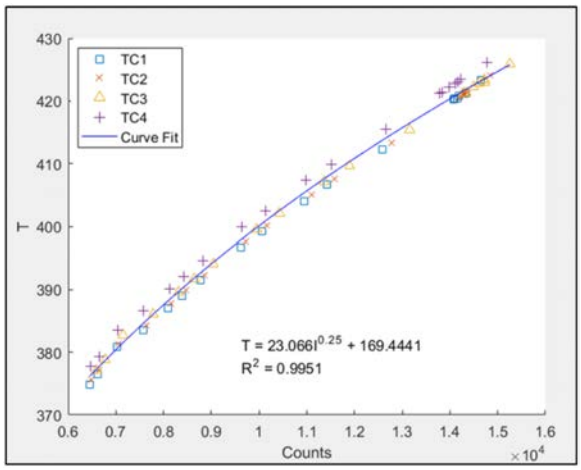

Figure 17. Sample IR calibration curve developed using AFIT's in-situ technique [31].

2.6.2 Hotwire Anemometry

A common way to measure freestream turbulence levels in a lab environment is through the use of hotwire anemometers, often called constant-temperature anemometers (CTA) because the wire is held at a constant elevated temperature. CTA anemometers are able to measure fine velocity fluctuations and high frequencies due to the small size of the wire sensors and the electronics that are used [32].

Hotwires are placed in one arm of a Wheatstone bridge, shown in Figure 18,

opposite a variable resistor. When the bridge is in balance, no voltage difference exists across the diagonal [32]. As air flows across the wire, the wire's temperature drops due to convection and as a result, the resistance of the wire decreases.

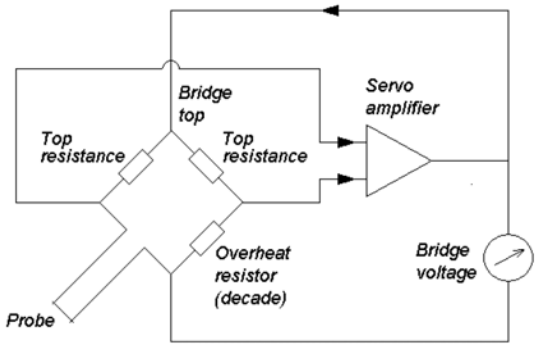

Figure 18. Principle diagram of a CTA anemometer [32].

To maintain the wire at a constant temperature, the rate of electrical energy supplied to the wire must be equal to the rate that heat is transferred from the wire to the surrounding fluid [32]. The probe current is represented by the voltage drop across the bridge and the squared output voltage, represented as E^2 in Equation 26, directly represents the heat loss from the wire [32].

$$P = i^2R = E^2 = hA(T_s - T_\infty) \tag{26}$$

The CTA system outputs the voltage, E, which is a function of the fluid velocity. A sample CTA calibration curve fit is shown in Equation 27.

$$U = C_0 + C_1E + C_2E^2 + C_3E^3 + C_4E^4 \tag{27}$$

where C_0, C_1, C_2, C_3, and C_4 are calibration constants.

III. Experimental Methodology

This research required the Film Cooling Rig (FCR) within the Combustion Optimization and Analysis Laser Laboratory (COAL LAB) at AFIT to be modified. Section 3.1 describes the FCR facility and the equipment used to complete the investigation. While previous research with the FCR has focused on reacting flows and scaling, the current research was focused on studying the effects of high freestream turbulence and conduction on film cooling effectiveness. Due to the nature of the previous research, the FCR was not equipped to study different levels of freestream turbulence. Section 3.2 details the changes made to the FCR, including the addition of a flow straightener and a turbulence generator to allow for variable freestream turbulence in the test section. Section 3.3 discusses the test section of the FCR, including the geometry of the various hole shapes that were studied. Section 3.4 details the test setup and computational analysis while Section 3.6 details the development of a new equation for overall effectiveness. Lastly, Section 3.7 details repeatability and Section 3.8 provides an uncertainty analysis.

3.1 Film Cooling Rig Facility

The FCR was designed to simulate a cooled turbine vane downstream of a combustor. This investigation utilized infrastructure that was developed in previous experiments [4, 5, 31]. Section 3.1.1 details the air supply for the FCR, while Sections 3.1.2 and 3.1.3 describe the equipment used to control the freestream and coolant flows, respectively. Section 3.1.4 discusses the previous FCR test section while Section 3.1.5 describes the cooling assembly used in previous FCR research.

3.1.1 FCR Air Supply

There were two possible sources of air for the FCR: an AFIT shared building air line and compressor dedicated to the COAL Lab. The AFIT shared air was supplied by two Kaeser BSD-50 air compressors and the COAL Lab air was supplied by an Ingersoll Rand H50A-SD compressor, the details of which are found in Tewaheftewa [31]. The air flow path for the rig is shown in Figure 19.

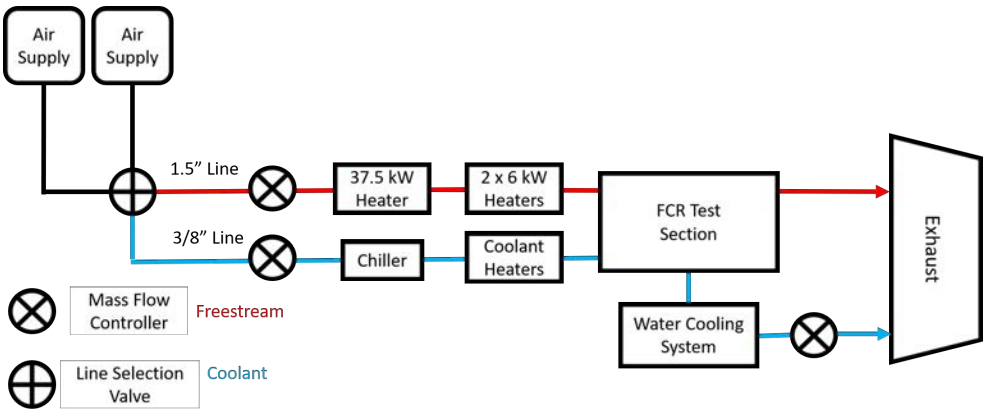

Figure 19. FCR air flow diagram.

The air source for the FCR was chosen by arranging the air flow valves, shown in Figure 20, to the desired configuration. Once the air supply was selected, air was routed to the FCR through two lines. The freestream air was routed through the 1.5" air line to the heaters, and the coolant air was routed through the 3/8" air line to a chiller. The COAL Lab air supply was typically chosen over the AFIT shared air supply because the Ingersoll compressor provided a more consistent air flow than the shared compressors.

3.1.2 Freestream Flow Control

The freestream air was controlled by the same control setup used by Lynch [5] and Tewaheftewa [31]. The setup, shown in Figure 21, consisted of an air-powered solenoid valve, a Fisher 299h pressure regulator, a Fox Thermal Instrument, Inc. FT2

flow meter, and a FlowServe MaxFlo 3 control valve. The air traveled from the air supply through the solenoid to the pressure regulator, which established the pressure necessary for the desired mass flow, and was controlled by the control valve, rated for a maximum flow rate of 0.3 kg/s [5, 31].

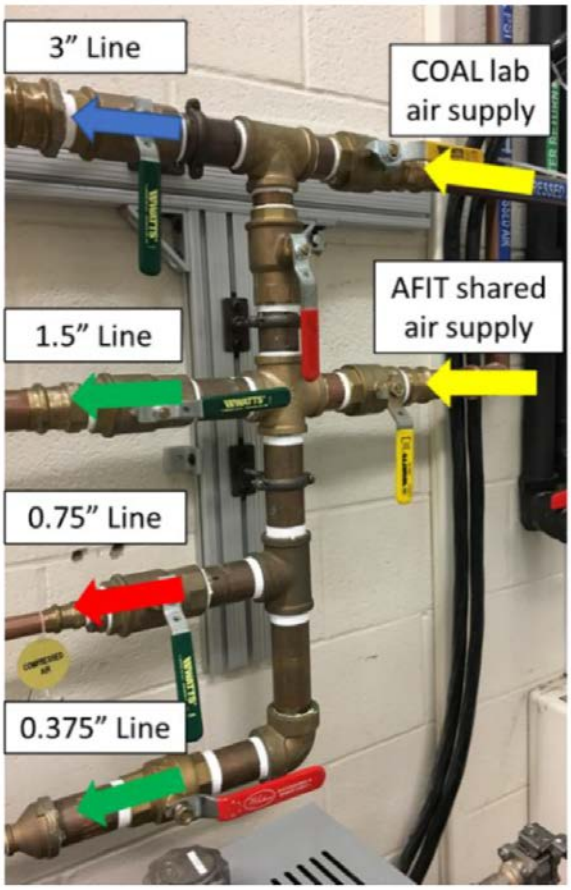

Figure 20. Main air flow manifold [31].

Before entering the FCR test section, the freestream air traveled through the 1.5" line to a series of heaters to heat the air to the desired freestream temperature. The air first passed through a 37.5 kW Gaumer Process heater mounted on the wall, shown in Figure 21, which heated the air to about 420 K. The Gaumer heater was powered and controlled by a control box mounted on the wall. Instead of entering the desired temperature, the heater was controlled by entering the desired percent of full power. This type of input resulted in different freestream temperatures depending on the air

flow through the heater. Consequently, the FCR took a longer time than would be desired, sometimes over an hour, to reach a steady state freestream temperature.

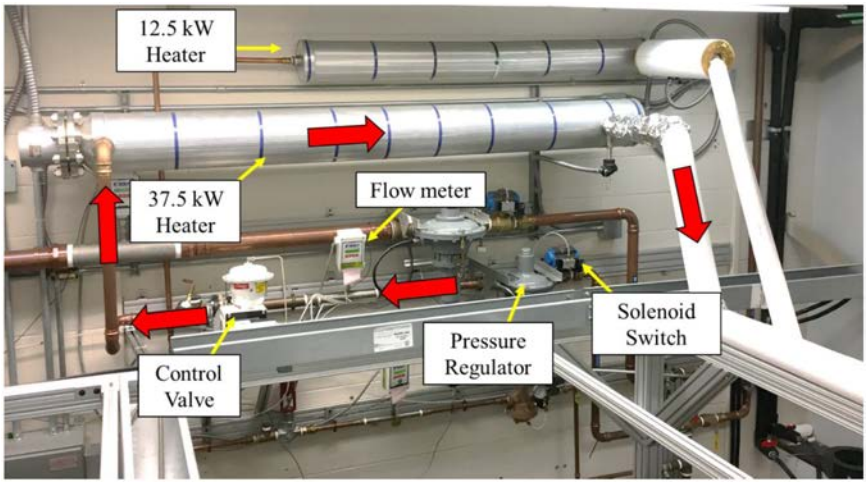

Figure 21. FCR freestream support equipment [31].

After passing through the Gaumer heater, the freestream air flowed through two 6 kW Osram Sylvania electric heaters, shown in Figure 22. The Osram heaters were located just before the FCR test section and further heated the air to the desired freestream temperature. Previous research with the FCR projected that the heaters were capable of heating the freestream air from 420 K to 650 K before entering the test section [31].

The two Osram heaters were controlled by an Athena digital temperature control that displayed the real time and set temperature. These heaters adjusted themselves automatically to achieve the desired freestream temperature using feedback from a 0.125 diameter thermocouple placed behind one of the heaters.

After traveling through the Osram heaters, the freestream air traveled through a 45.7 cm long flexline and through the toroid bypass, shown in Figure 23, as described by Lynch [5] and Tewaheftewa [31]. The air then entered an aluminum transition stack, shown in Figure 24. The transition stack served the purpose of changing the duct's cross section from a 49.5 mm diameter circular pipe to a 50.8 mm wide and

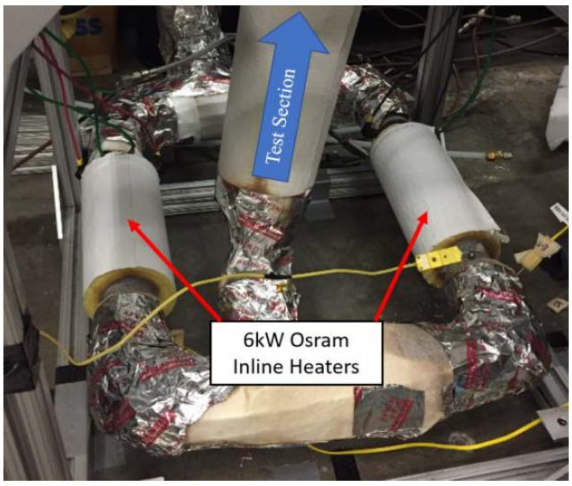

Figure 22. Osram heaters used to heat FCR freestream [5].

25.4 mm tall rectangular duct. After passing through the transition stack, the air entered the newly installed flow straightener, described in Section 3.2.1.

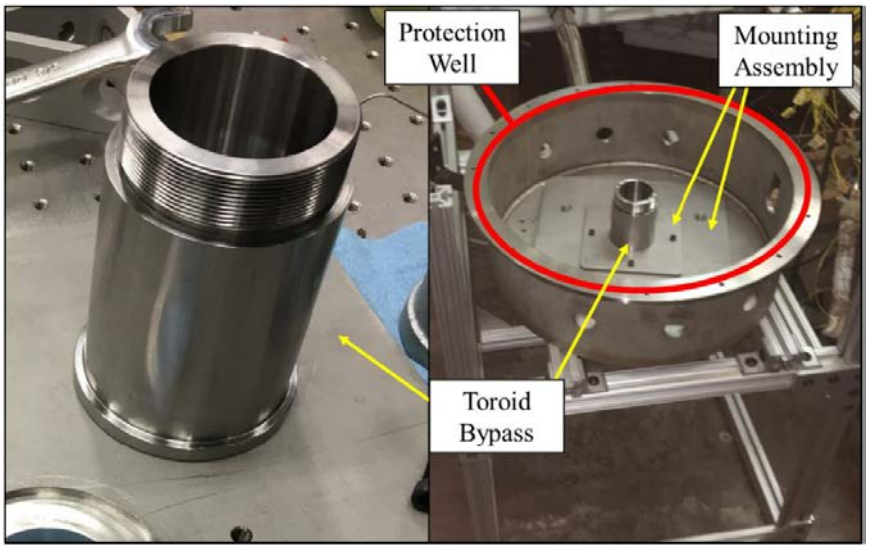

Figure 23. FCR toroid bypass (left) and mounting assembly (right) [31].

3.1.3 Coolant Flow Control

The 3/8" line, shown in Figures 19 and 20, was used as the coolant supply line. The air pressure was controlled by a Valtek pressure regulator and the flow rate was controlled by a MKS MC20A mass flow controller. The inlet coolant temperature

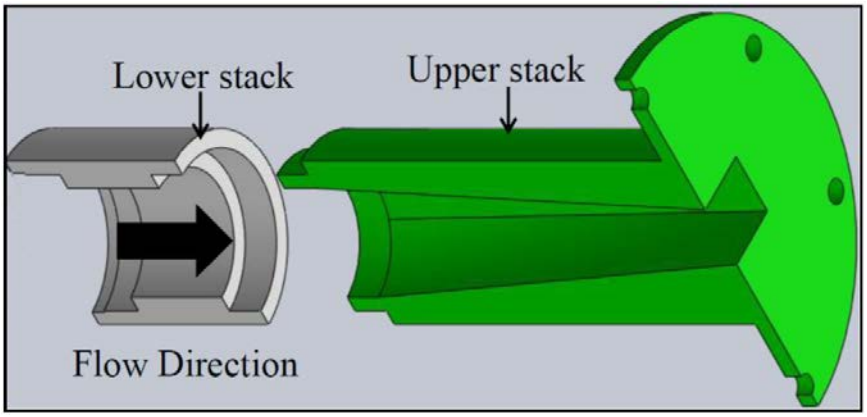

Figure 24. FCR aluminum transition stack [31].

was controlled by two inline electric heaters and a chiller. The details of the heaters and heater controllers can be found in Lynch [5]. The coolant directly entered the coolant assembly, shown in Figure 25, traveled along the coolant channel, discussed in Section 3.1.5, and exited the block.

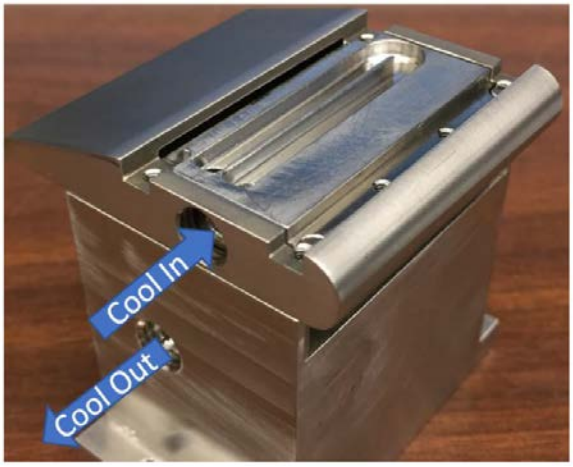

Figure 25. FCR coolant block and airfoil used in previous FCR research [5].

The coolant mass flow out of the film cooling holes was controlled by an additional mass flow controller located downstream of the FCR test section. This mass flow controller was set so that the difference in mass flows would result in the desired blowing ratio exiting the cooling holes. The first mass flow controller had a range of 50 SLPM and the second mass flow controller had a range of 30 SLPM. A Welch

WOB-L 2585 vacuum pump created a vacuum downstream of the second mass flow controller to draw the coolant out of the coolant block. The coolant flow rates used in this research are summarized in Section 3.4.

The coolant would heat up as it traveled through the coolant assembly and needed to be cooled down so that the second mass flow controller would not be damaged. A water-cooling system, shown in Figure 26 and described in detail in Lynch [5], sent the heated coolant through a copper line within a sealed water tank and circulated water through the tank. After traveling through the copper line, transferring heat

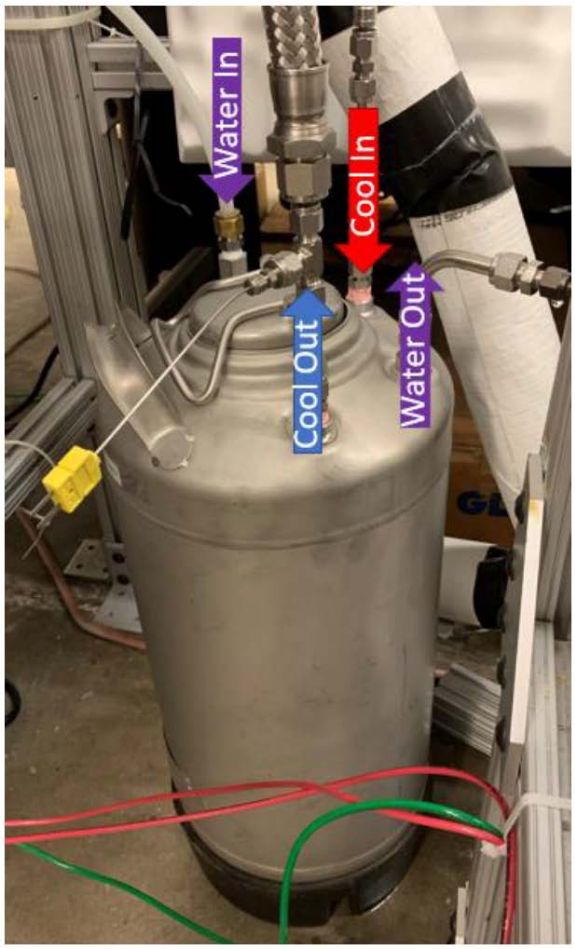

Figure 26. Water-cooling system used for coolant line [5].

to the circulating water, the coolant exited the tank. Thermocouples at the water outlet and coolant outlet were used to monitor the temperature of the coolant before

entering the second mass flow controller.

3.1.4 Previous FCR Test Section

The FCR, discussed in Lynch [5] and Tewaheftewa [31], was capable of operating at high temperatures and low temperatures and could use multiple gases for the freestream and coolant. The test section, shown in Figure 27, consisted of the main block, the coolant block assembly, and the viewport. The previous coolant block assembly is discussed in Section 3.1.5 and the coolant block assembly for this research is discussed in Section 3.2.4. The viewport, discussed in detail in Section 3.3.3, had a sapphire window that allowed optical access to the test airfoil for the IR camera.

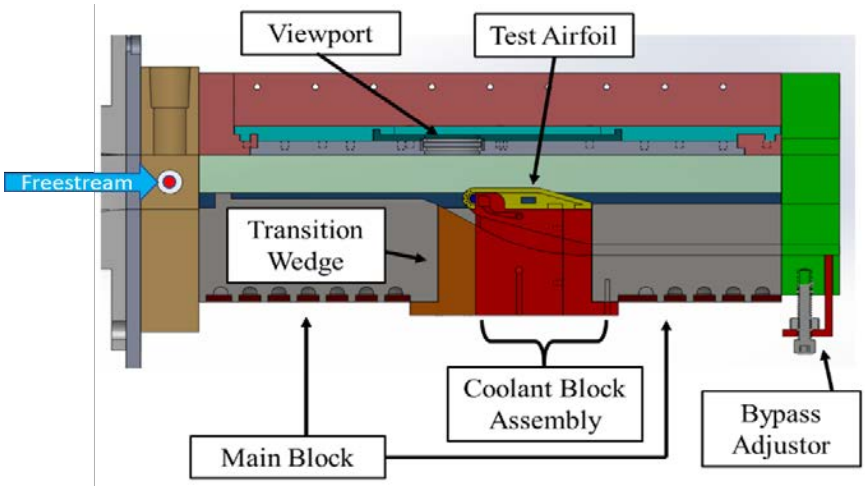

Figure 27. Previous version of FCR.

When the freestream air entered the test section, it flowed past the boundary layer trip and then traveled either over the airfoil or down the boundary layer bypass, shown in detail in Figure 28. In previous FCR research focused on the leading edge, the bypass channel was used to control the location of the stagnation point on the airfoil. The stagnation point could be shifted up or down by using the bypass adjustor shown in Figure 27 to adjust the amount of air that flowed through the bypass [5].

In previous work, the boundary layer trip, shown in Figure 29, allowed for a

consistent turbulent boundary layer that could be removed before the airfoil at the boundary layer bypass, creating a more uniform freestream flow [5]. A fully turbulent boundary layer also allowed previous students to use turbulent boundary layer correlations and freestream Reynolds number to predict boundary layer growth. It was discovered that the boundary layer trip was causing unexpected difficulties for the present research, discussed in detail in Section 3.2.2, and had to be altered. After passing over the airfoil or down the bypass, the flow exited the rig through either the main exit or the adjustable bypass exit.

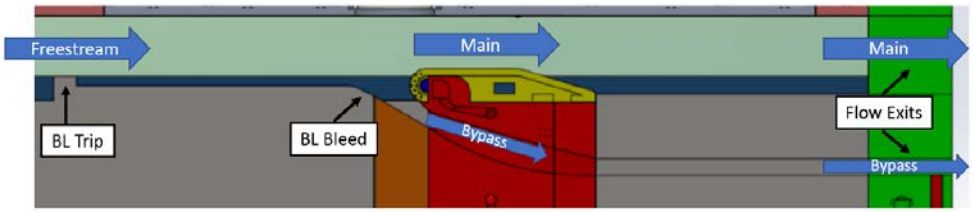

Figure 28. Previous FCR flow path [5].

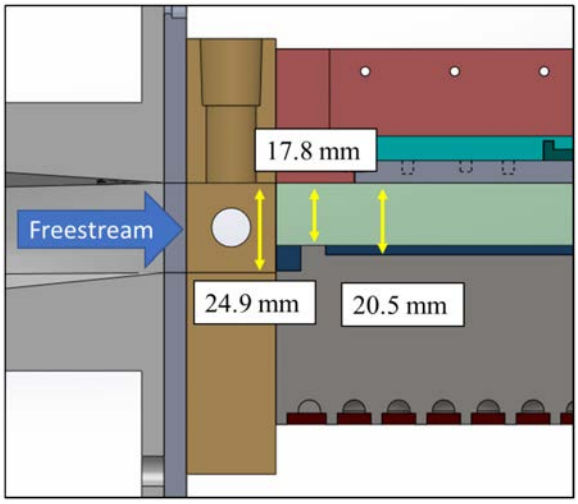

Figure 29. Freestream entry into previous version of FCR [31].

3.1.5 Previous Coolant Assembly

Turbine blades typically have internal passages, shown in Figure 30, that feed multiple rows of film cooling holes on the airfoil surface. This research builds off

of Lynch [5] and aims to replicate a typical turbine blade with an internal passage feeding the pressure side cooling holes. The u-bend of Passages 5 and 6 in Figure 30 were replicated to simulate the thermal environment around the row of pressure side holes.

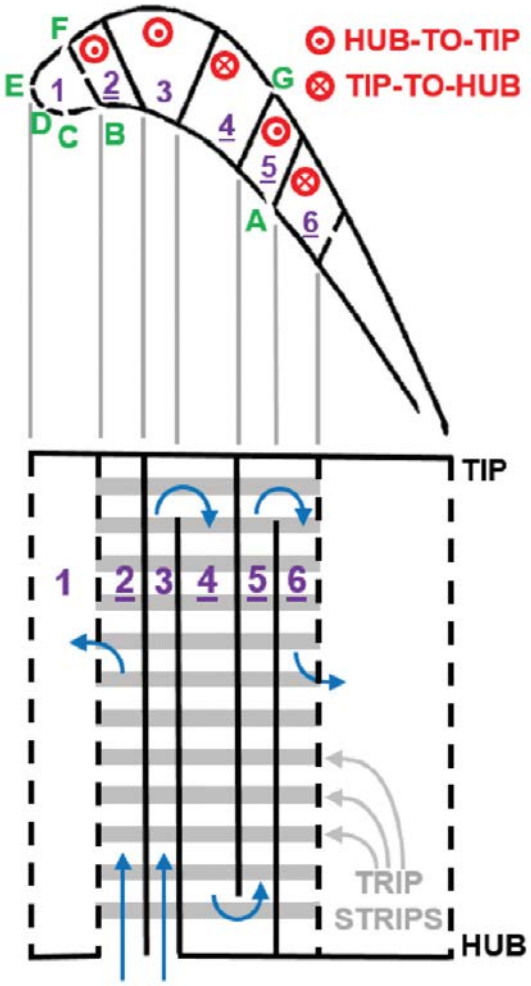

Figure 30. Schematic of internal passages in a typical airfoil [33].

As a result of this research being focused on pressure side holes located on the flat portion of the airfoil, Lynch [5] used flat interchangeable plates for the three hole shapes being studied. The coolant block and airfoil, shown in Figure 25, were 3-D printed in Inconel 718 and then machined to the final specifications.

The channel dimensions were specified by the sponsor of the research and are

shown in Figure 31. The channel's cross-sectional area was constant along the length of the channel to keep the flow consistent through all of the cooling holes. The channel extended past the row of holes on each side of the channel to allow for uniform flow across the hole inlets.

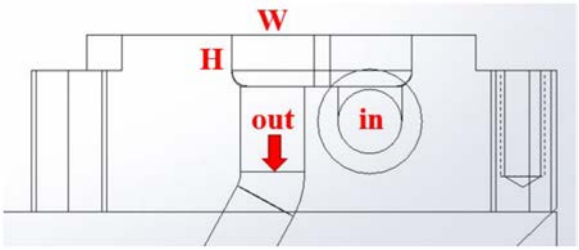

Figure 31. Coolant channel dimensions [5].

Several plates were manufactured for Lynch's investigation [5]: one blank plate with no film cooling holes, and one plate for each shaped hole. The two film cooling holes, discussed in detail in Section 3.3.1, are shown in Figure 32. The plates were secured with six screws: four corner screws secured to the airfoil and two center screws secured to the coolant block, shown in Figure 25.

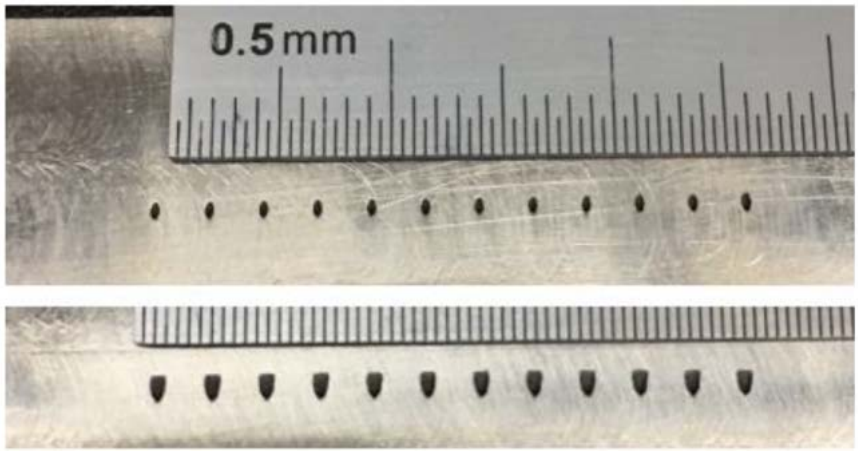

Figure 32. Cylindrical and laidback fan-shaped shaped holes (from top to bottom) [5].

Lynch [5] ran into issues when testing the seal between the airfoil and blank plate to the coolant block. The tightening of the airfoil to the coolant delivery block was expected to create a contact pressure seal, which would enable all inlet flow to travel

through the coolant channel without escaping. The airfoil was secured to the coolant block with two connection rods, shown in Figure 33, that went through and out the bottom of the coolant block and allowed the airfoil to sit flat on the coolant block. The ends of the connection rods were threaded so that a nut at the bottom end of the rods could secure the airfoil onto the coolant block. The two center screws of the plates also screws into the block to increase the sealing ability of the cooling assembly.

Testing revealed that the contact seal was not working and 10 SLPM was leaking from the assembly when coolant was flowing through the channel. A high-temperature Room-Temperature-Vulcanizing (RTV) silicone, shown in Figures 34 and 35 was used in an attempt to complete the seal, but the cooling assembly was still losing 3.7 SLPM. The RTV sealant was also creating an artificial conduction path that is not present in real airfoils. The sealing issues experienced by Lynch [5] led to a redesign of the cooling assembly, discussed in Section 3.2.4.

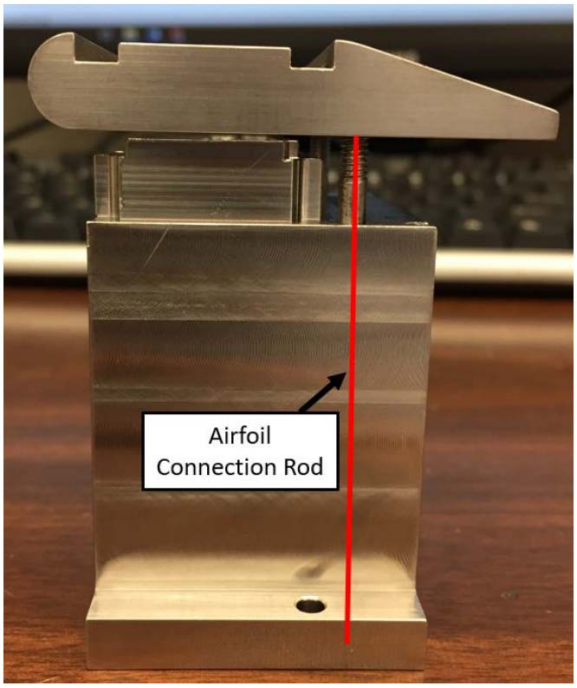

Figure 33. Airfoil connection rods [5].

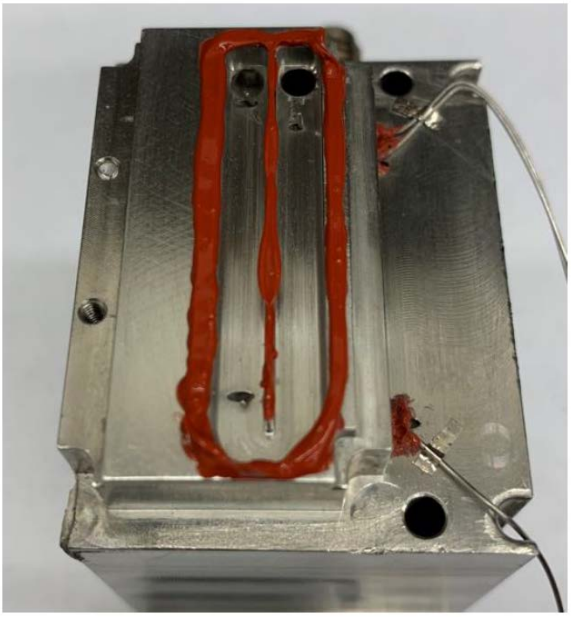

Figure 34. RTV seal for coolant block channel [5].

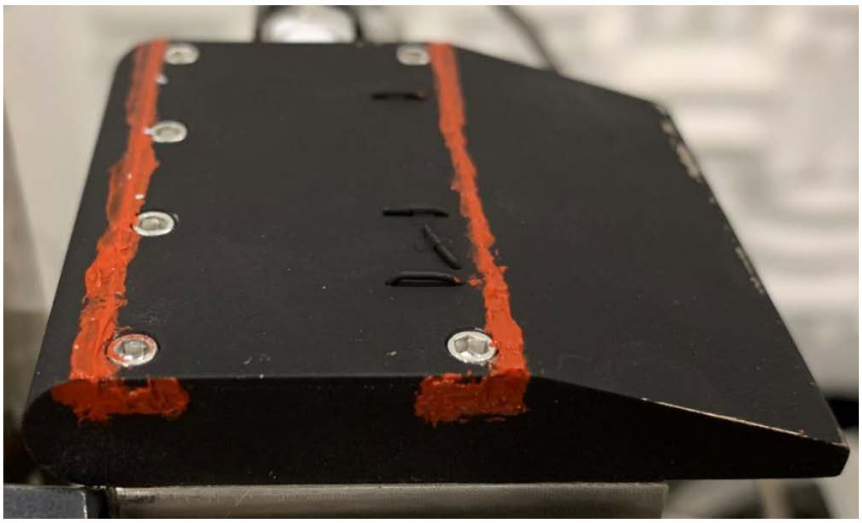

Figure 35. RTV border seal used in previous FCR research [5].

3.2 Film Cooling Rig Modifications

The FCR required several changes before the effects of high freestream turbulence could be investigated, including the design and installation of a flow straightener, discussed in Section 3.2.1, and a turbulence generator, discussed in Section 3.2.3. Section 3.2.2 discusses modifications made to the boundary layer trip that was introduced in

Section 3.1.4. Additionally, the sealing issues with the previous airfoil and coolant block design required a redesign of the cooling assembly, discussed in Section 3.2.4.

3.2.1 Flow Straightener

To study the effects of high freestream turbulence and turbulent length scale on the film cooling effectiveness of film cooling holes, it was important to be able to generate low levels of turbulence to serve as a baseline. A calibration jet was used to calibrate the hotwire before taking measurements in the rig. As described in Section 2.6.2, the calibration jet produced a range of jet velocites and the CTA system outputted the voltage, E. The calibration curve fit is shown in Figure 36. The hotwire uncertainty was calculated by taking the standard deviation of the differences between the fluid velocity and the fluid velocity calculated by the curve fit. The standard deviation was then multiplied by the inverse CDF of the Student's T distribution for a 95% confidence interval, resulting in an uncertainty of $0.18 m/s$. The hotwire was then used to measure the freestream turbulence intensity and integral length scale entering the test section. The location of the hotwire is represented by the red circle in Figure 27. Initial hotwire tests revealed that the flow entering the test section had a turbulence intensity around 6% and an integral length scale of 5 cm.

A flow straightener was designed to decrease the magnitude of the freestream turbulence intensity entering the test section. The flow straightener, shown in Figure 37, consisted of a 2.5:1 area expansion, an expanded sheet of aluminum honeycomb, a stainless steel wire mesh, and a 2.5:1 area contraction. The honeycomb was 1.27 cm thick and was made up of 0.635 cm cells, while the mesh consisted of holes that were 1 mm in diameter. The flow straightener was made of three separate pieces held together by two set-pins. A bottom view of the flow straightener is shown in Figure 38.

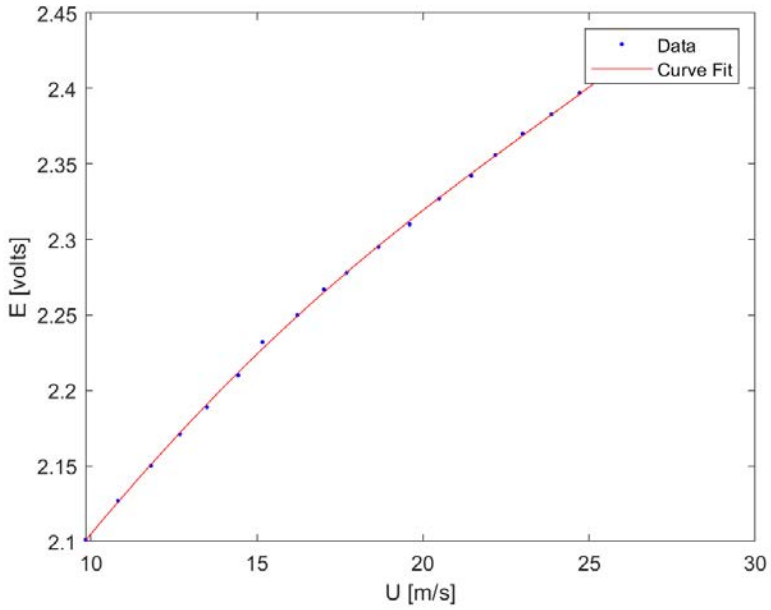

Figure 36. Hotwire calibration curve

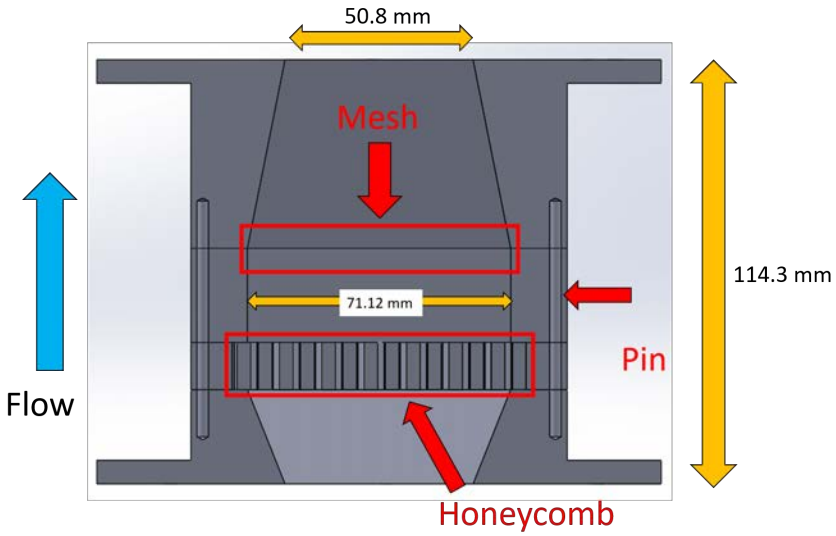

Figure 37. Cross section of flow straightener used in FCR.

Each component of the flow straightener was designed to aid in the production of low freestream turbulence intensities. The expansion decreased the velocity of the freestream so that the majority of the turbulent eddies were affected by the honeycomb. The honeycomb then "straightened" the flow by minimizing the lateral

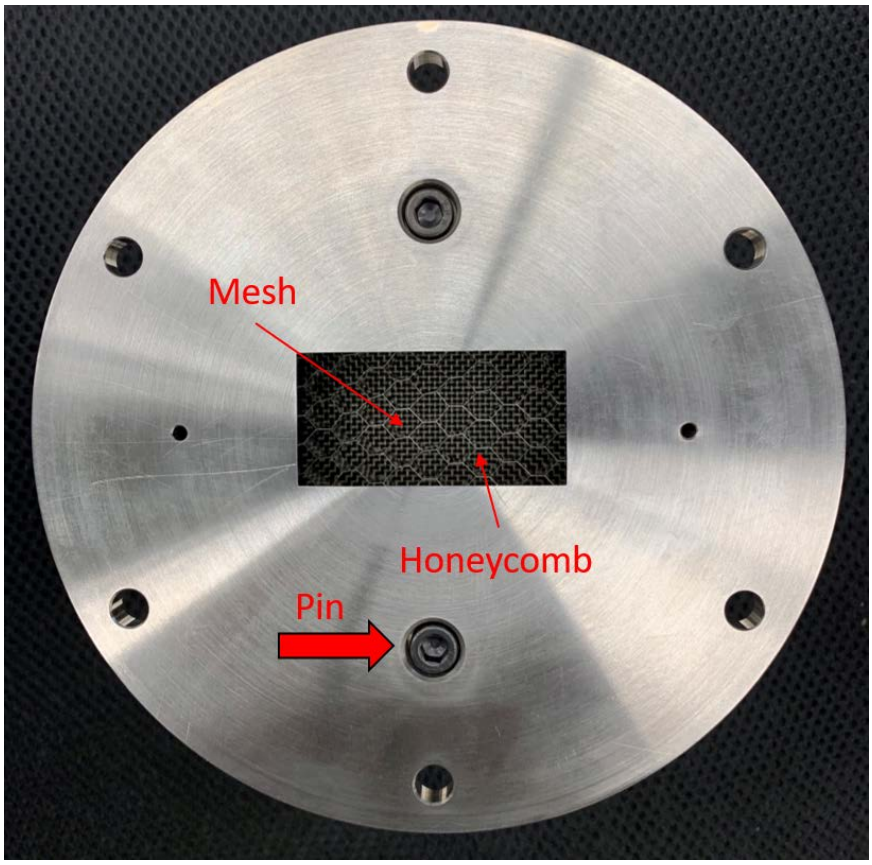

Figure 38. Bottom view of FCR flow straightener.

velocity components that were the result of the rotating motion of the air entering the FCR. The integral length scales of the flow exiting the honeycomb were on the order of the honeycomb cell size, and were small enough that they could be affected by the screen. The subsequent screen then generated turbulence at smaller length scales, as described by Baines and Peterson [25], that dissipated rapidly due to the small size of the mesh holes. The contraction then accelerated the flow to further decrease the magnitude of the freestream turbulence intensity. The definition of turbulence intensity, seen in Equation 12, dictates that the magnitude of the turbulence intensity must decrease if the velocity fluctuations stay the same and the mean flow velocity increases. After the flow straightener was installed, hotwire tests revealed that the freestream entering the FCR had a turbulence intensity of 2% and an integral length

scale of approximately 7.5 cm.

3.2.2 Boundary Layer Trip

The purpose of the flow straightener was to reduce the turbulence intensity of the freestream entering the test section. Initial tests with a hotwire located above the film cooling holes, represented by the red circle in Figure 39, revealed turbulence levels in excess of 20%. Since turbulence measurements directly after the flow straightener showed Tu levels around 2%, the turbulence was being generated by an aspect of the FCR. Examination of the rig revealed that the boundary layer trip introduced in Section 3.1.4 was located between the flow straightener and the location of the high freestream turbulence, making the boundary layer trip the possible culprit for the high freestream turbulence. The purpose of the boundary layer trip was to generate a turbulent boundary layer, but the turbulence intensity was not expected to be as high as it was away from the wall. This was the first time that turbulence measurements had been taken in the FCR because previous research with the FCR did not focus on freestream turbulence.

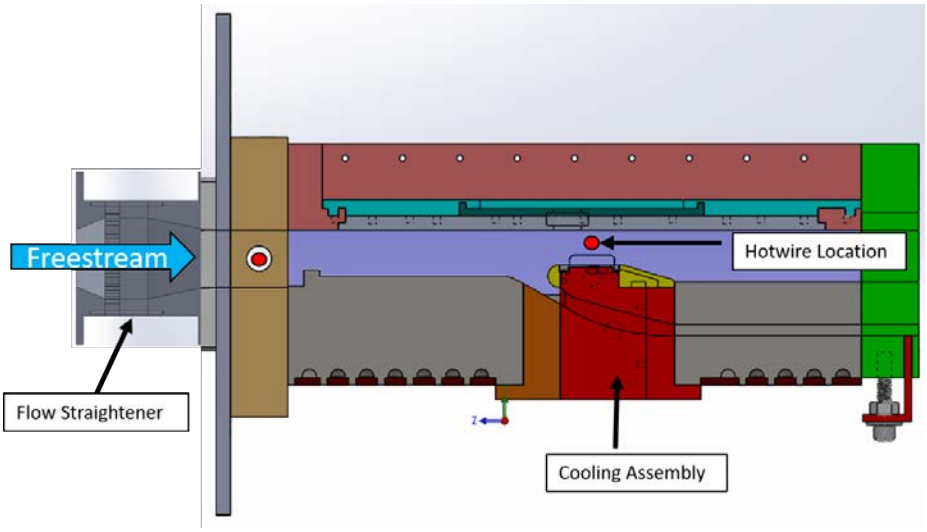

Figure 39. FCR test section with flow straightener installed.

AFIT technician Josh Dewitt shaved off the boundary layer trip from the main block using a grinding wheel in an attempt to reduce the generation of freestream turbulence after the flow straightener. Figure 40 shows the main block after the boundary layer trip was shaved off. Hotwire tests with the new version of the main block revealed freestream turbulence intensities around 2% at the location of the film cooling holes.

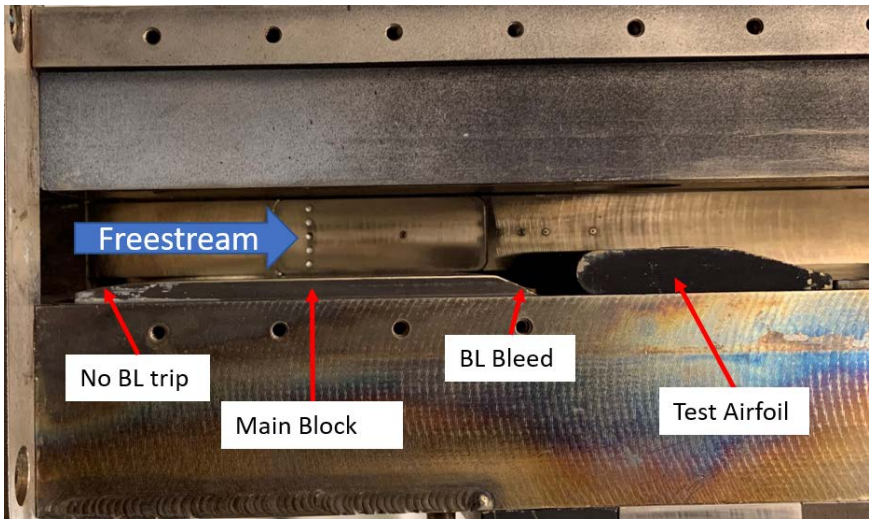

Figure 40. Main block after the boundary layer trip was shaved off.

3.2.3 Turbulence Generator

A turbulence generator was designed and installed in the FCR to allow the effects of high freestream turbulence on film cooling effectiveness to be studied. Four levels of freestream turbulence intensity were desired for this research: 5%, 10%, 15%, and 20% at different length scales. As discussed in Section 2.5, there are multiple ways to generate freestream turbulence. Cylindrical rods were chosen as the turbulence generation method for this research due to the relative ease of changing turbulence intensity and length scale. The SMR correlation from Roach [34] was used to calculate x/D, the required downstream distance, x, normalized by the rod diameter, D. Possible rod diameters were then chosen based on the available distance upstream

of the airfoil. Table 2 shows the rod diameters and downstream distances from the film cooling holes for different levels of freestream turbulence intensity, where M is the spacing between the rods. In Figure 41, x is represented by the horizontal yellow arrow, and M is represented by the vertical red arrow. To investigate the impact of length scale on overall effectiveness, multiple length scales for a constant turbulence intensity were desired. Since the length scales of rod-generated turbulence were expected to be on the order of the size of the rods, two configurations were chosen for 10% and 15%. Table 2 shows that the two configurations for 10% and 15% consisted of different rod diameters and downstream distances even though the desired $Tu\%$ was the same.

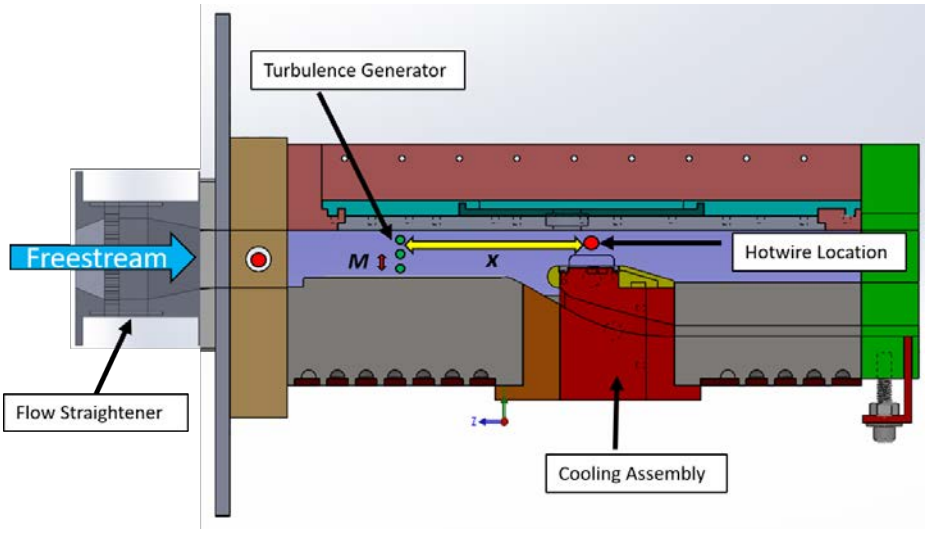

Figure 41. FCR test section showing the turbulence generator dimensions.

Table 2. Rod diameters and downstream distances for the desired turbulence intensity at the film cooling holes.

Desired $Tu\%$	x/D	D [mm]	x [mm]	M [mm]	Number of Rods
5	48.5	1.59	77.0	3.83	5
10	18.4	2.38	43.8	5.74	3
10	18.4	4	73.5	9.64	2
15	10.4	4	41.7	9.64	2
15	10.4	5	52.1	12.0	2
20	6.96	5	34.8	12.0	2

To implement the chosen method of turbulence generation in the FCR, the previous side plates, described in previous FCR work [5, 31], were redesigned to implement the generator rods. The design of the turbulence generator consisted of two main side plates bolted into the main block with #6-40 screws, shown in Figure 42, and various inserts. Each insert bolted into the side plates with four #6-32 screws and had holes for the various rod sizes, depending on the desired freestream turbulence intensity.

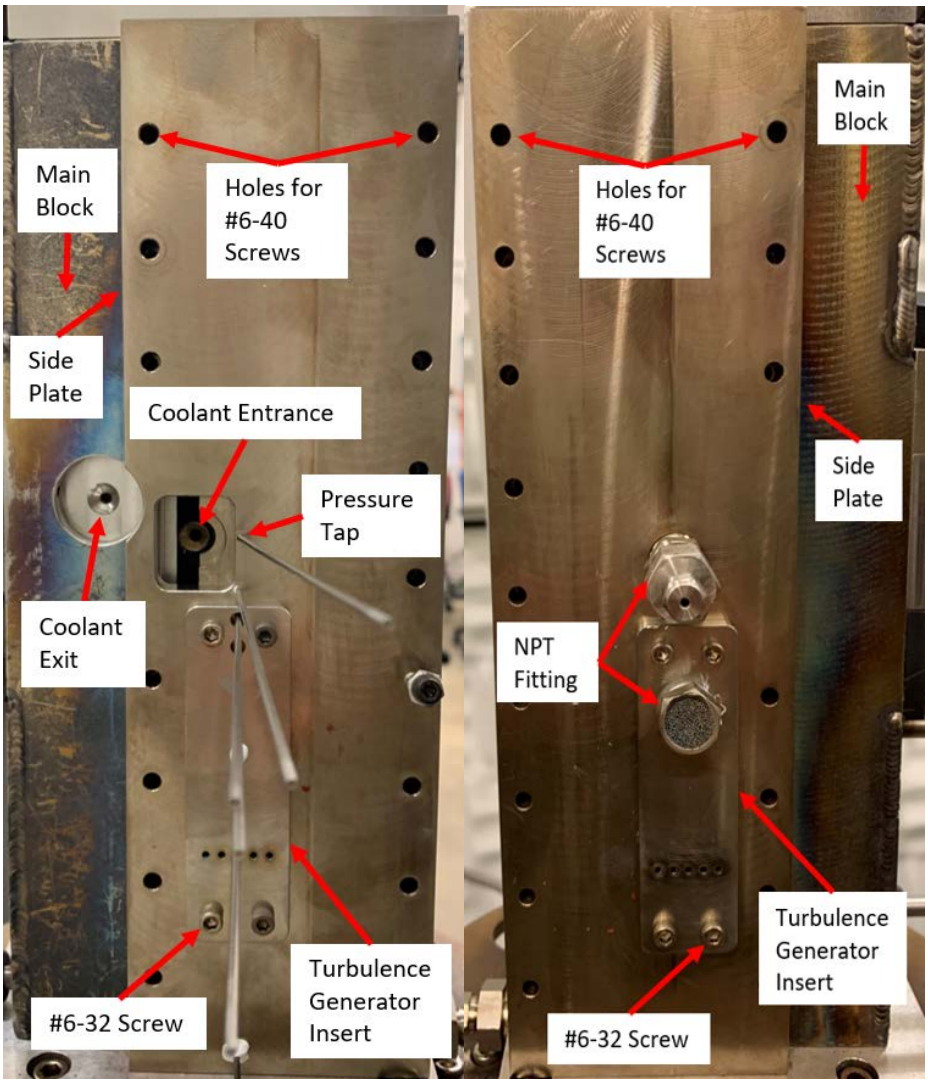

(a) Side Plate on Coolant Side (b) Side Plate on Hotwire Side

Figure 42. New FCR side plates showing the turbulence generator inserts and various features of the plates.

A side view of the FCR with the turbulence generator and flow straightener installed is shown in Figure 43. The side plates were 3/8" thick so that a 1/4" NPT fitting, used to hold the hotwire support rod, could screw directly in to the side of the front plate plate. The front side plate with the hotwire in place is also shown in Figure 43. The three hotwire locations for turbulence testing are labeled as 1, 2, and 3.

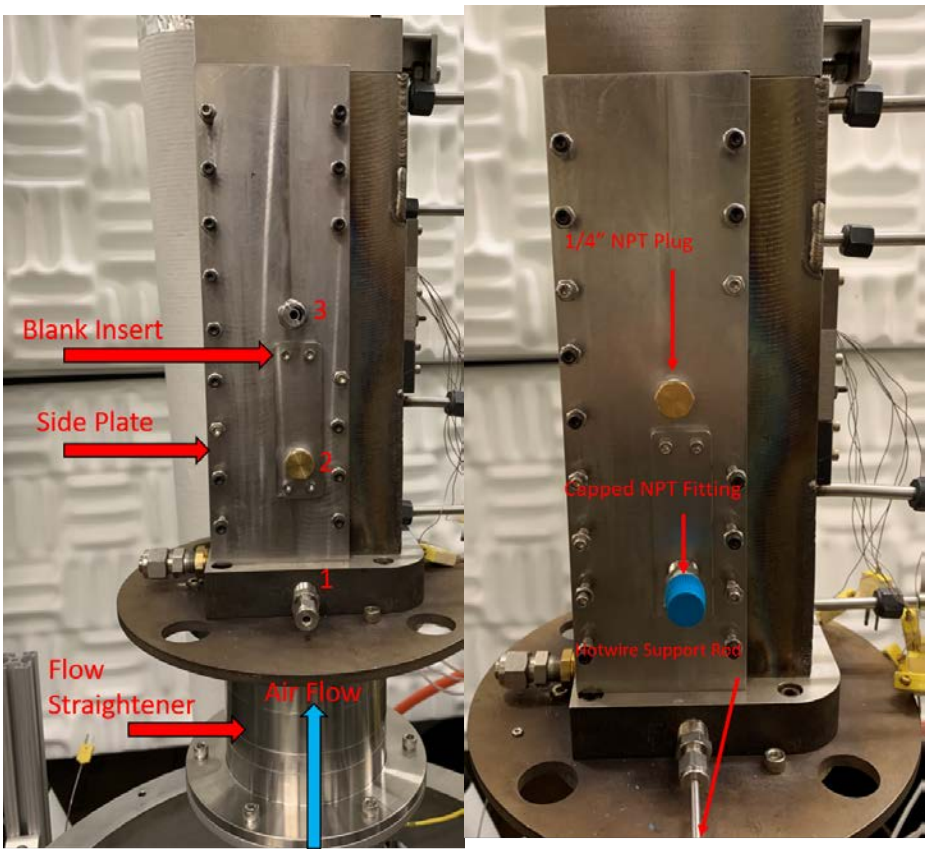

(a) Flow Straightener and New Side Plates

(b) Hotwire in Place for Testing

Figure 43. Side view of the FCR showing the flow straightener new side plates installed and the hotwire in place for testing.

The resulting turbulence at the location of the film cooling holes was characterized using hotwire anomometry for each turbulence insert and freestream Reynolds number, Re_D. The velocity scale and length scale for Re_D were the mean freestream

velocity above the airfoil and the airfoil's leading edge diameter, respectively. The CTA system obtained 2,048 velocity measurements at a rate of 5 kHz. Initial testing was conducted with insert "10 Big" to determine how many samples were needed. The turbulence intensity and integral length scale at the location of the film cooling holes were calculated for sample sizes of 2048, 4096, and 8192 at four different values of Re_D. The hotwire location is represented by the red circle above the airfoil in Figure 41. As discussed in Section 2.4, the turbulence intensity was calculated by dividing the root-mean-square velocity by the mean flow velocity and the length scale was calculated with an autocorrelation. Figures 44 and 45 show the turbulence intensity and length scale at hotwire position 3 versus sample size and show that 2,048 samples was enough. As the sample size increased, there was no noticeable trend in Tu or length scale. Surprisingly, Tu consistently decreased as sample size increased for $Re = 5k$. A possible reason for this is the inconsistent flow controller at the low flow rate that is required for $Re = 5k$. This research did not test at $Re = 5k$, so the inconsistent flow rate for that Reynolds number was not a concern.

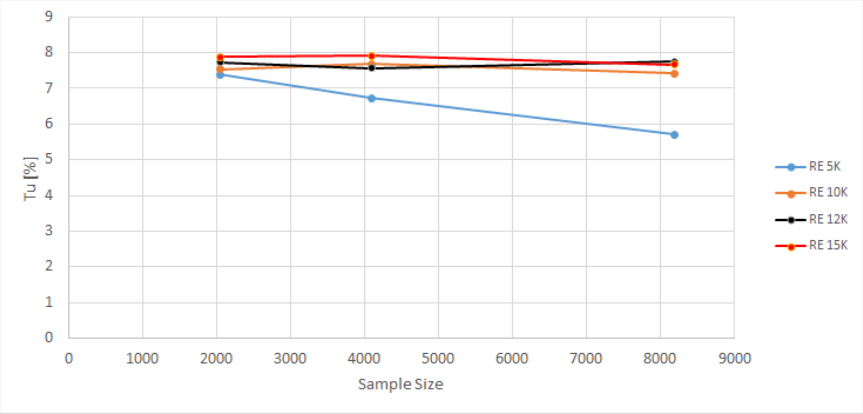

Figure 44. Turbulence intensity at hotwire Position 3 for insert "10 Big" versus sample size.

Table 3 summarizes the resulting turbulence intensity and integral length scale at the location of the film cooling holes for each turbulence generator insert. The turbulence intensity for the majority of the inserts was slightly lower than the desired

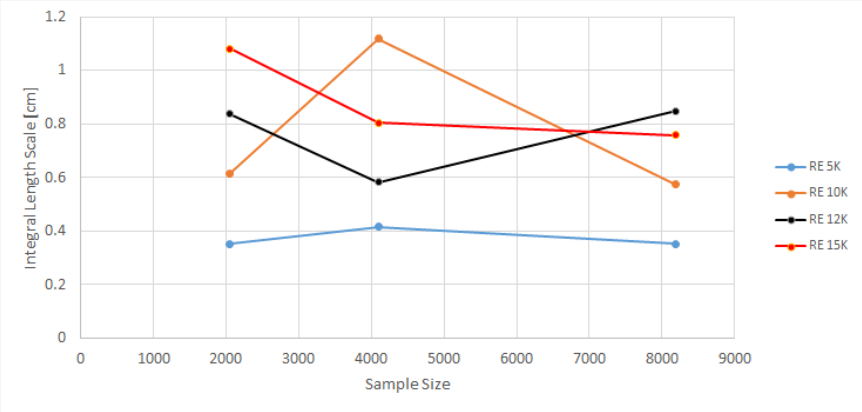

Figure 45. Integral length scale at hotwire Position 3 for insert "10 Big" versus sample size.

turbulence intensity, which could be the result of interactions with the top wall and the acceleration of the freestream as it goes over the top of the airfoil.

Table 3. Resulting Tu and integral length scales at the film cooling holes from the various turbulence generator configurations.

Insert	Re_D	Desired Tu%	Average Tu%	Integral Length Scale [cm]
5	10k	5	3.6	0.347
5	15k	5	3.5	0.498
10	10k	10	8.5	0.318
10	15k	10	8.8	0.405
10 Big	10k	10	7.6	0.444
10 Big	15k	10	7.8	0.626
15	10k	15	13	0.237
15	15k	15	14	0.439
15 Big	10k	15	12	0.601
15 Big	15k	15	11	0.745
20	10k	20	12	0.271
20	15k	20	11	0.311

Figures 46 and 47 show the turbulence decay downstream of the turbulence generator for $Re = 10k$ and $Re = 15k$. The linear decay of Tu downstream of the grid agrees with the SMR data found in Roach[34] for all but one case. The turbulence did not decay for the 5mm-diameter rods for $Re = 15k$. It is possible that the freestream turbulence for this case was not fully developed, as this was only at $x/D = 7$, and

did not yet start the process of isotropic decay.

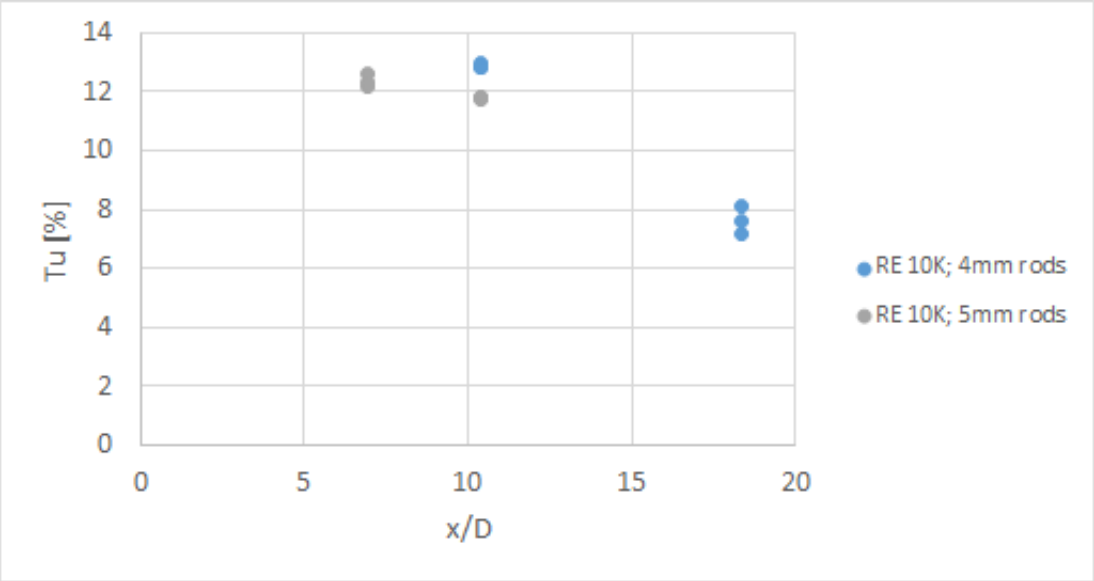

Figure 46. Turbulence decay downstream of the turbulence generator for $Re_D = 10k$.

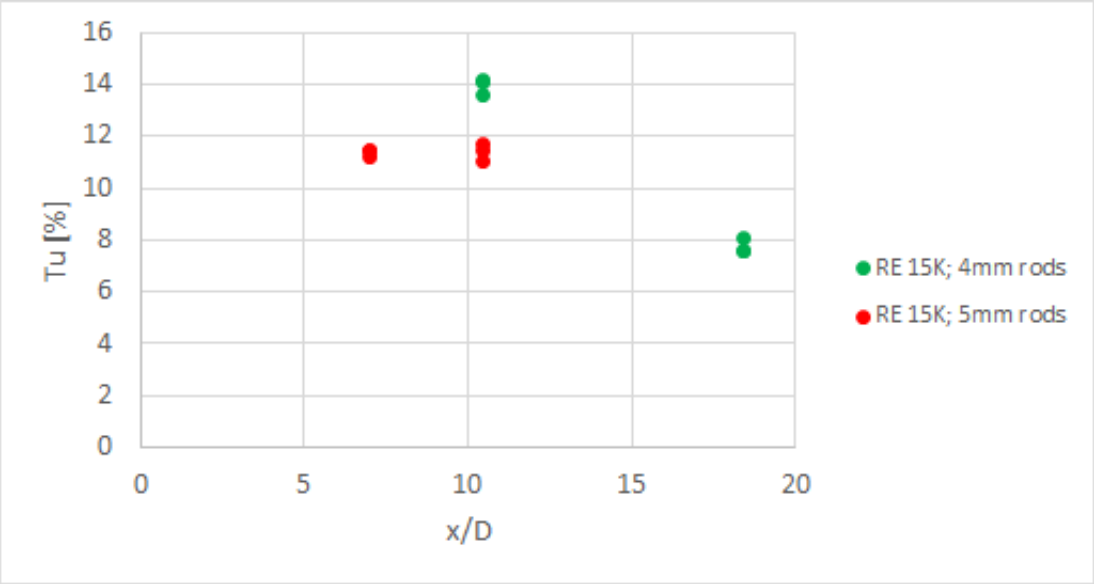

Figure 47. Turbulence decay downstream of the turbulence generator for $Re_D = 15k$.

3.2.4 Cooling Assembly

The cooling assembly was redesigned to combat the sealing issues discussed in Section 3.1.5. Instead of interchangeable plates with the various film cooling holes, it

was decided to manufacture separate airfoils for each hole design under investigation, which are discussed in Section 3.3.1. Changing the design from interchangeable plates to separate airfoils removed the potential leakage paths that were causing Lynch's[5] sealing issues. Additionally, an O-ring was placed between the airfoil and the coolant block, shown in Figure 48, to complete the seal between the airfoil and block.

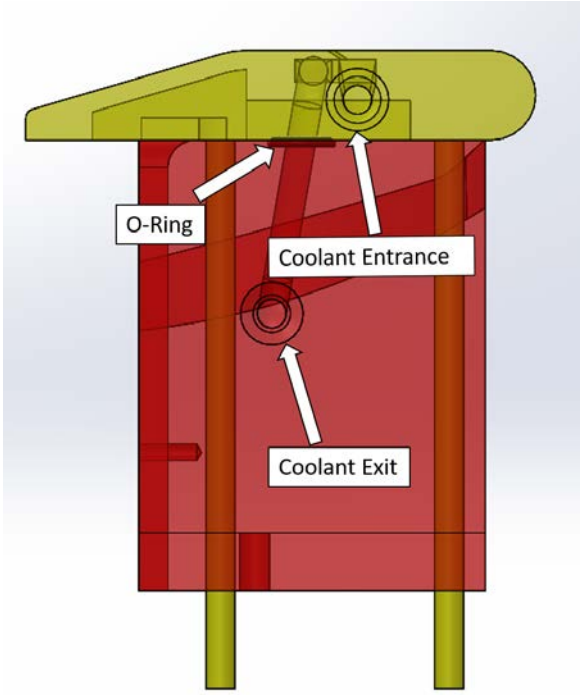

Figure 48. Side view of FCR cooling assembly.

A top view of the airfoil design is shown in Figure 49, where the top surface is transparent to reveal the internal coolant channel and the coolant path is labeled by the light blue arrows. The internal channel was designed to replicate a serpentine passage found in a typical turbine blade, with the dimensions of the channel shown in Figure 50. The channel was 2.54 mm high and 4.06 mm wide, with 1 mm between the top of the channel and the external surface of the airfoil. After the airfoils were 3D-printed, a hole was drilled into the top of the channel to measure the thickness of the external surface above the channel. Measurements of the four airfoils revealed that the thickness was consistent between the airfoils and the average thickness was

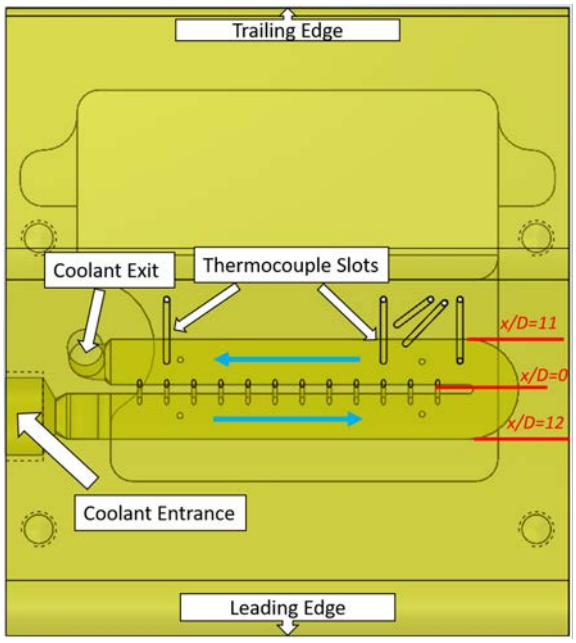

Figure 49. Top view of airfoil with cylindrical film cooling holes and slots for routing surface thermocouples.

1 ± 0.1mm. As discussed in Section 3.3.2, this hole was used for an internal surface thermocouple. The divider between the two loops of the channel was 0.84 mm thick.

The coolant entered the airfoil and fed the twelve cooling holes as it traveled along the channel. The entrance of the film cooling holes started at approximately $x/D \approx -4$. The film cooling holes exited above the downstream channel and on the other side of the channel divider. The geometry of the film cooling holes is discussed in Section 3.3.1. The coolant exited the film cooling holes above the center divider and flowed across the airfoil surface above the return loop of the coolant channel. There was 2.4 mm between each hole, giving a pitch spacing, P/D, of 6. The remaining coolant was turned at the end of the channel, and exited through the bottom of the airfoil. As seen in Figure 49, the coolant loop started at $x/D \approx -12$ and ended at $x/D \approx 11$. Instrumentation for the new setup is discussed in Section 3.3.2.

The airfoils and cooling insert were 3D-printed in Inconel 718, with a thermal conductivity of $11.2\frac{W}{m-K}$, and then machined by the AFIT machine shop to the final

dimensions. The final cooling assembly is shown in Figure 51. Initial testing with the cooling assembly revealed that the combination of the O-ring, the vacuum pump, and the cooling channel being integrated into the airfoil resulted in no coolant leaking from the new airfoil design. The mass flow controllers discussed in Section 3.1.3 were connected to the coolant block and the airfoil without film cooling holes to verify that the assembly was sealed. When a case was run with 10 SLPM entering the assembly, the mass flow controller downstream of the cooling assembly measured 10 SLPM, verifying that no coolant was leaking from the assembly.

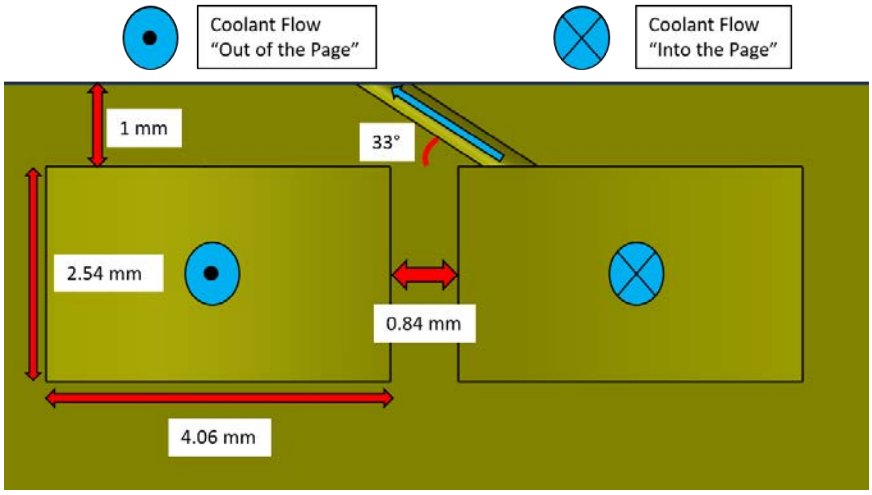

Figure 50. Section view of the internal coolant channel with the dimensions of the channel and coolant flow labeled.

3.3 Film Cooling Rig Test Section

After flowing through the heaters discussed in Section 3.1.2, the freestream air entered the rig, went through the flow straightener, and was directed to the test section, shown in Figure 52. The freestream traveled through the turbulence generator and then impacted the test airfoil. Section 3.3.1 discusses the hole geometries used in this investigation while Section 3.3.2 discusses the instrumentation. Lastly, Section 3.3.3 talks about the viewport that allowed optical access for the IR camera.

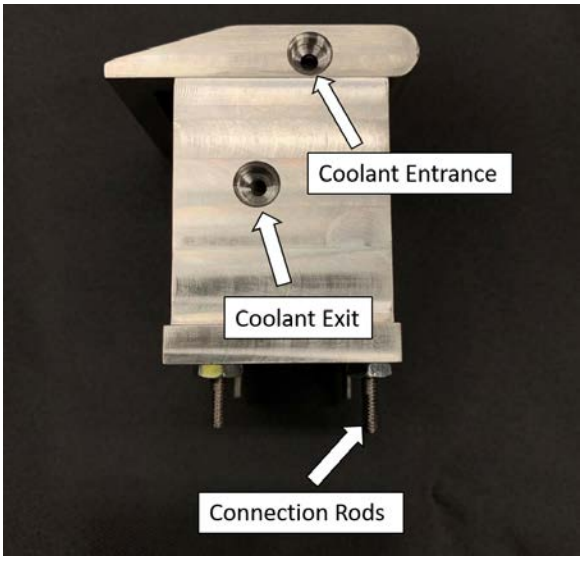

Figure 51. Side view of FCR cooling assembly.

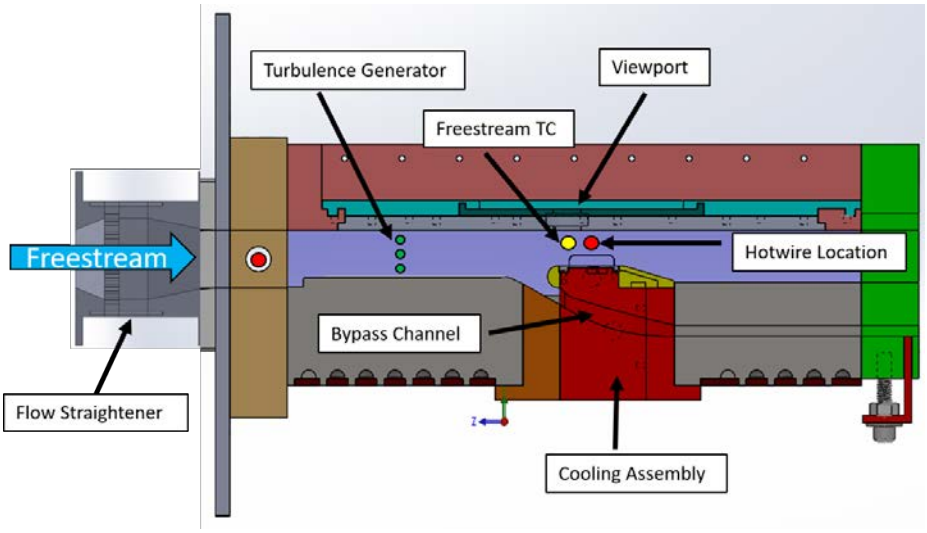

Figure 52. FCR Test Section.

3.3.1 Cooling Hole Geometry

The two cooling holes investigated, shown in Figure 53, were a cylindrical hole and a 10-10-10 laidback fan-shaped hole. The holes had the same inlet diameter of 0.381 mm and a pitch spacing of $6d$. The 10-10-10 hole was similar to the 7-7-7 hole that was discussed in Section 2.3, but the laidback angle was ten degrees. Both holes had the same initial injection angle of 33°.

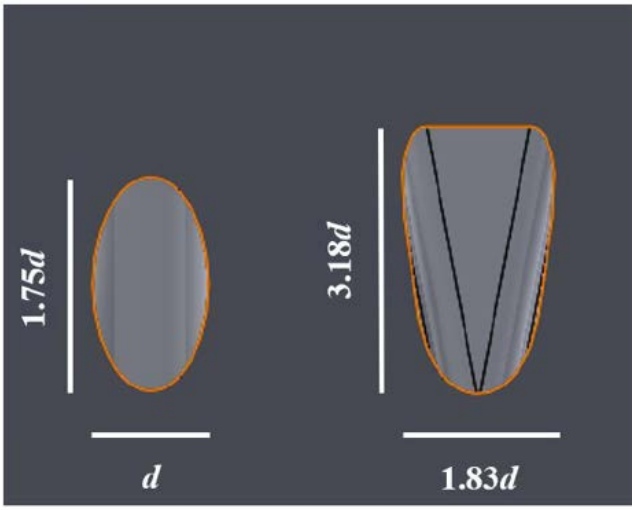

Figure 53. Dimensions of cylindrical and 10-10-10 film cooling holes (left to right) [5].

The film cooling holes were created using electrical discharge machining at Meyer Tool. Figure 54 shows the airfoil with cylindrical holes after all required machining was completed. Figure 54 also shows slots that were machined into the airfoil for thermocouples. The slots allowed the thermocouples to be flush with the surface so as to not disturb the boundary layer.

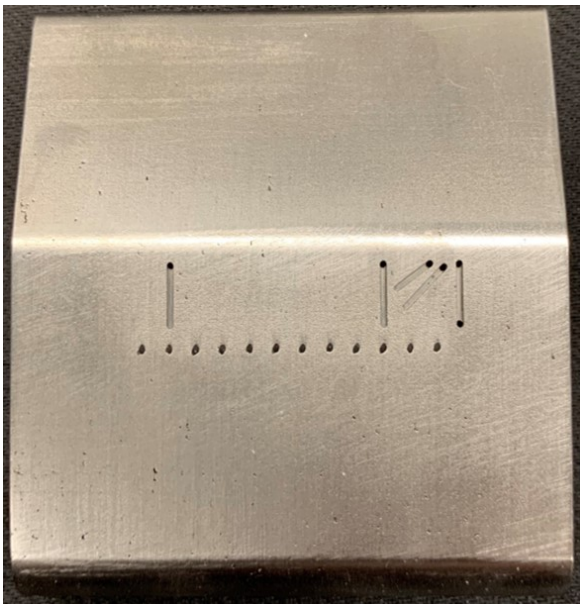

Figure 54. Top view of completed airfoil with cylindrical holes.

3.3.2 Instrumentation

Pressure taps and thermocouples were used to measure various pressures and temperatures in the FCR. To capture the freestream conditions, pressure taps and a thermocouple were installed on the side plate using Resbond 989 ceramic adhesive, shown in Figure 55. The pressure measurements were used to track the freestream velocity and the thermocouple was used to measure the temperature of the freestream entering the rig.

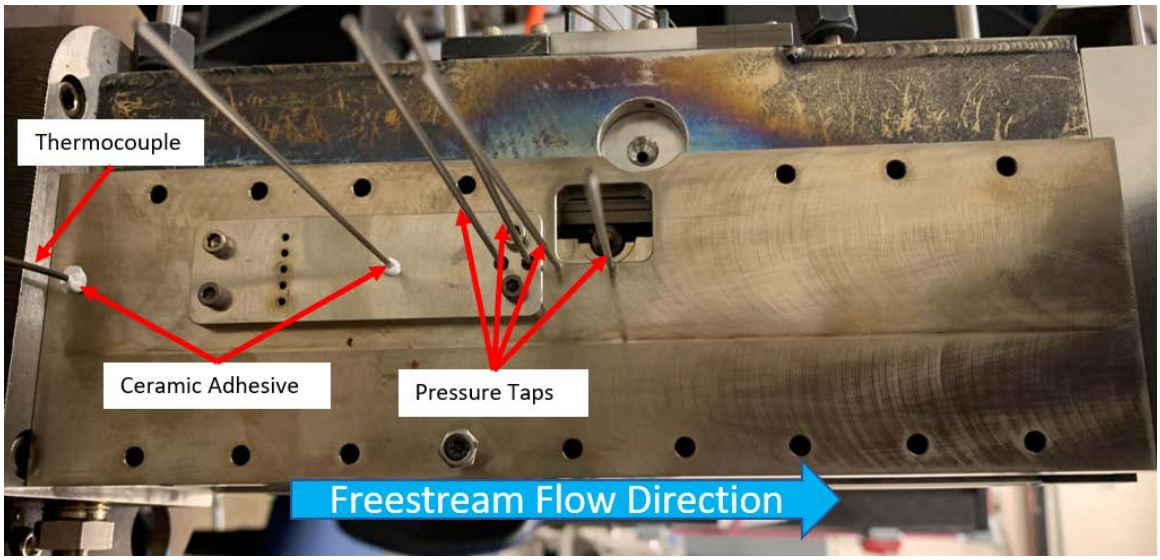

Figure 55. Side plate instrumentation used to measure the characteristics of the freestream air in the FCR.

Several more thermocouples were installed on the airfoil as shown in Figure 56. Thermocouples measuring the coolant temperature, labeled "IC" and seen by the dark blue circles in Figure 56, were placed along the coolant channel to determine the local coolant density ratio, DR. These temperatures were compared with the coolant inlet temperature to examine how much the coolant warmed up as it traveled through the coolant channel.

External surface thermocouples, labeled "S" and represented by the red circles in Figure 56, measured the external wall temperature and provided reference points for

the IR camera calibration, discussed in Section 3.4.2. An additional thermocouple, represented by the green circle in Figure 56, measured the internal wall temperature. A 3.18 mm K-type thermocouple, shown in Figure 57, measured the coolant temperature 70.3 mm before it entered the airfoil. During operation, a thermocouple was placed on the compression fitting that was connected to the airfoil to estimate the temperature rise of the coolant. During testing, the temperature of the fitting was approximately $100K$ and $200K$ higher than the upstream coolant temperature for freestream temperatures of $550K$ and $650K$, respectively.

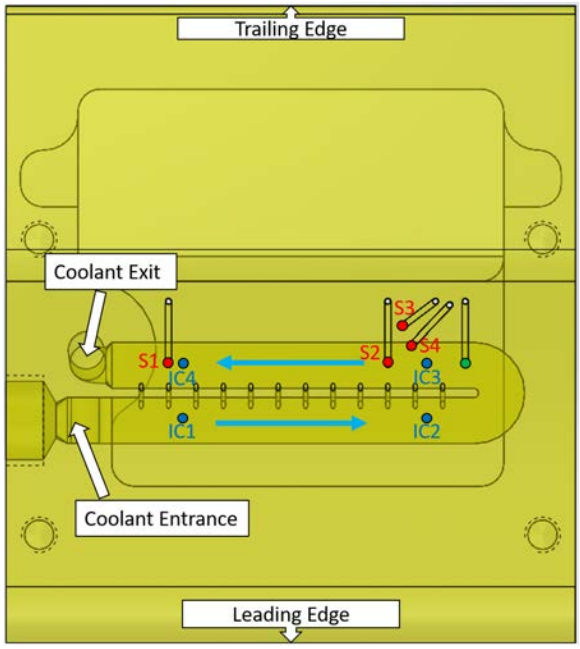

Figure 56. Thermocouple locations for the airfoil with cylindrical film cooling holes.

After the thermocouples were installed on the airfoils, the airfoil surface was painted black with *VHT Flameproof* for the IR thermography method described in Section 2.6.1. The painted airfoils were cured using the process described by Rathsack [35] and shown in Table 4 to prevent the paint from flaking off during high-temperature tests. The temperatures in Table 4 are in Fahrenheit because that was the operational units on the curing oven that was used. Figure 58 shows the test airfoil with cylindrical holes after being painted black and cured.

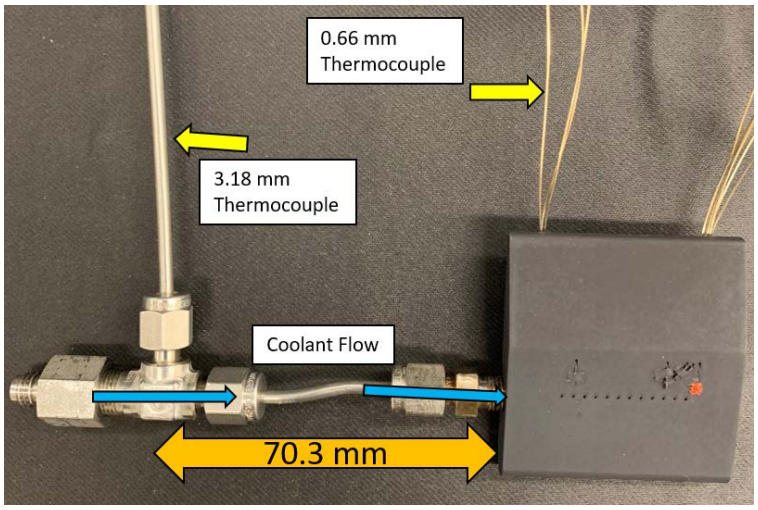

Figure 57. Thermocouple location for the coolant inlet temperature.

Table 4. Curing times and temperatures for applied paint.

Time [minutes]	Temperature [$^{\circ}F$]
15	250
30	600
60	800
30	1000

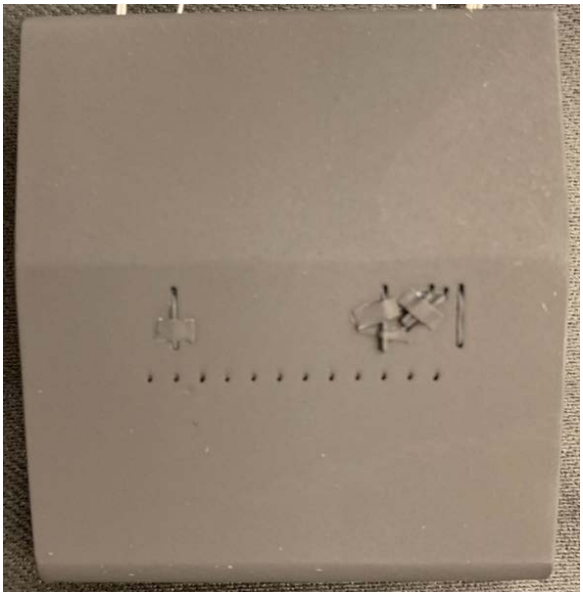

Figure 58. Airfoil with cylindrical holes after being painted and having the thermocouple installed.

3.3.3 Viewport

The viewport assembly, introduced in Section 3.1.4 and shown in Figure 59, allowed the IR camera to view the airfoil test surface through a 25 mm diameter sapphire window. The viewport assembly consisted of a bottom plate, a window plate, and a sealer plate, shown in Figure 60a. The bottom plate provided the hole for line-of-sight access to the test surface and the window plate sandwiched the sapphire window against the bottom plate. The sealer plate secured the bottom plate and window plate in place with screws and created an additional seal to minimize air leaking from the rig. The assembly was modular to allow the sapphire window to be in different locations.

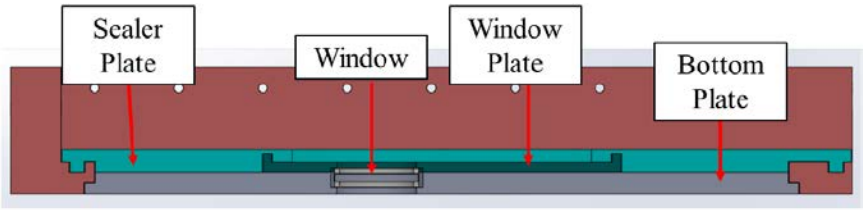

Figure 59. Viewport assembly [31].

Several sets of bottom plates and window plates, designed for Tewaheftawa [31] and shown in Figure 60b, were available to use depending on which part of the airfoil was being studied. The diameter of the sapphire window being 25 mm meant that only a small portion of the airfoil could be seen through the window. Previous research [5, 31] focused on the leading edge of the airfoil and used the 65-degree view bottom plate. This research focused on the downstream pressure surface of the airfoil and required the use of the 45-degree view bottom plate. Figure 61a shows the IR camera setup and the different camera angles used to study the various parts of the airfoil. Figure 61b shows the assembled viewport installed in the rig. During testing, the camera was raised and the camera angle was adjusted to view more surface upstream of the cooling holes. Raw IR images for the two views are shown in Figure 62.

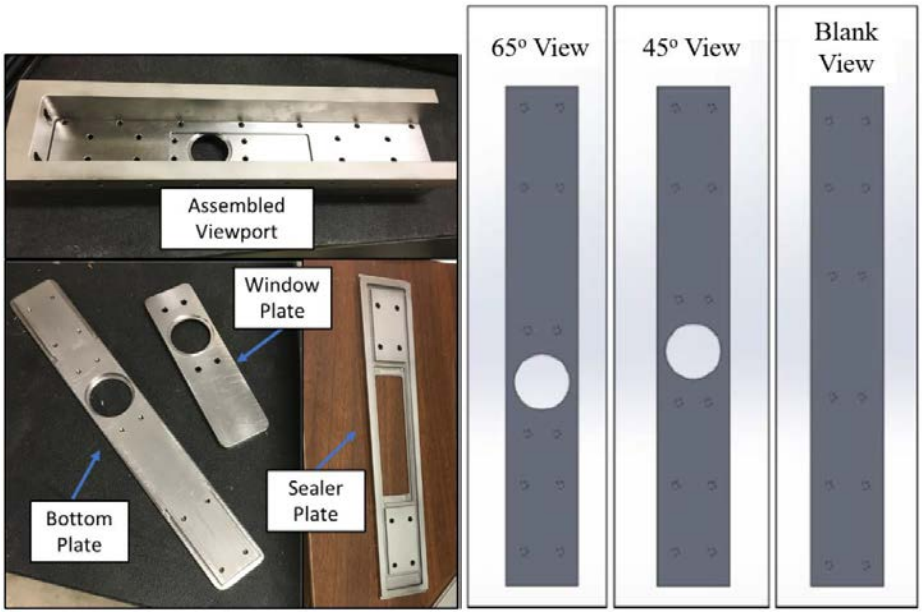

(a) Viewport Assembly Components (b) Viewport Bottom Plates

Figure 60. Viewport assembly components and various viewport bottom plates.[31].

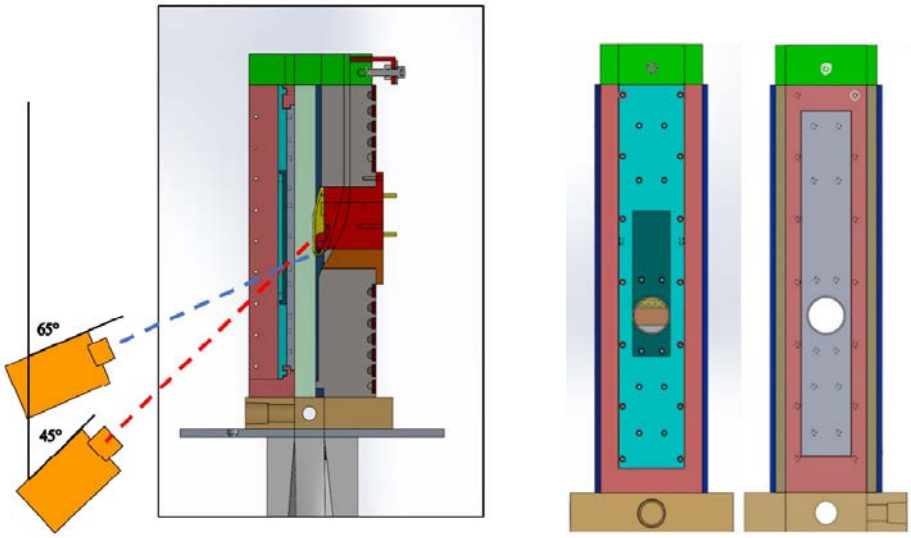

(a) IR Camera Angles (b) Assembled Viewport

Figure 61. FCR IR camera angles and assembled viewport installed in rig [31].

In previous research, the epoxy used to hold the window in place leaked into the image. To avoid the same issue in the current research, the sapphire window was removed and the old epoxy was carefully scraped off of the window. Lab Technician

Josh Dewitt polished the window and placed it back in the window plate before carefully applying fresh epoxy to hold the window in place. It was important to not use more epoxy than required so that there was not extra epoxy to leak into the viewing window. The epoxy was allowed to dry before installing the viewport assembly into the rig to ensure that liquid epoxy would not leak into the image.

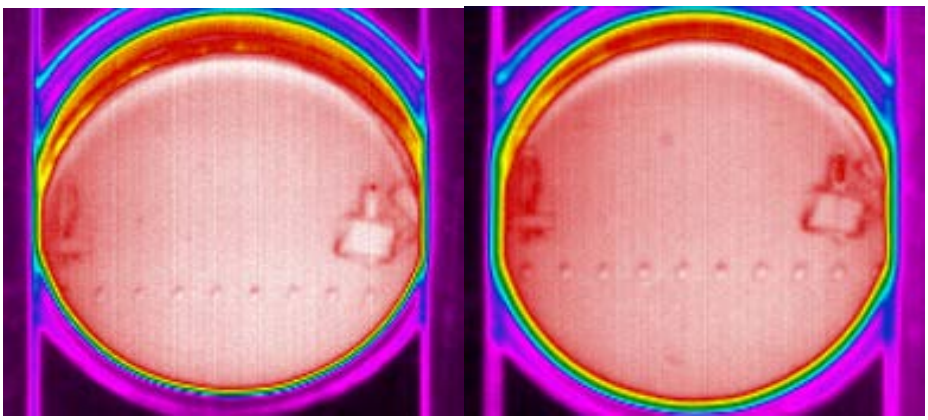

(a) View 1 (b) View 2

Figure 62. The two IR camera views used in this investigation.

3.4 Test Setup and Computational Analysis

This investigation required specific coolant flow rates to study the effects of high freestream turbulence on the overall film cooling effectiveness of shaped holes. Section 3.4.1 discusses how the required coolant flow rates were determined based on the desired Advective Capacity Ratio, ACR, and the desired freestream Reynolds Number based on leading edge diameter, Re_D. The Infrared thermography method, discussed in Section 3.4.2, was used to record the radiation counts coming off of the test surface and convert the counts to temperature measurements. The investigation also required a spatial calibration, discussed in Section 3.4.3, to convert the camera's image into a two-dimensional image. After the camera's image was calibrated to produce a two-dimensional image of the airfoil's surface temperature, a MATLAB code converted

the image into a contour plot of overall effectiveness. This process is discussed in Section 3.4.4.

3.4.1 Test Setup

Blowing ratio sweeps from $M = 0.25$ to $M = 2.0$ were conducted for each airfoil and freestream turbulence configuration for Reynolds numbers of $Re_D = 10,000$ and $Re_D = 15,000$. The length scale and velocity scale used to calculate the Reynolds numbers were the leading edge diameter and the freestream velocity at the location of the film cooling holes, respectively. The freestream massflow rate and cross-sectional area above the airfoil were used to determine the freestream velocity at the location of the film cooling holes. The Reynolds number was modified by setting the freestream massflow to the required value based on the density of the freestream, the desired freestream velocity, and the cross-sectional area of the test section. Equations 28 and 29 were used to determine the flow rates required out of the cooling holes to achieve the desired blowing ratios, where $\dot{m}_c$, is the coolant mass flow rate, $\dot{m}_\infty$ is the freestream mass flow rate, A_∞ is the cross-sectional area of the test section, and A_c is the total cross-sectional area of the film cooling holes. For this investigation, A_∞ was $1.04 * 10^{-3} m^2$ and A_c was $1.03 * 10^{-5} m^2$. Discharge coefficients of 0.75 for the cylindrical hole and 0.80 for the shaped hole [36] were then used to determine the actual flow rates required to achieve the desired blowing ratio, shown by Equation 30. The blowing ratios and corresponding flow rates for this research are shown in Table 5.

$$M = \frac{\rho_c U_c}{\rho_\infty U_\infty} = \frac{\dot{m}_c A_\infty}{A_c \dot{m}_\infty} \tag{28}$$

$$\dot{m}_c = M \frac{A_c \dot{m_\infty}}{A_\infty} \tag{29}$$

$$\dot{m}_{c,req} = \frac{\dot{m}_c}{C_d} \tag{30}$$

The blowing ratios were converted to ACR using Equation 31, where c_p is the specific heat at constant pressure. The specific heats were determined using the temperatures of the coolant in the internal channel and freestream. Known values of air's specific heat at different temperatures were used to create a curve-fit and the curve-fit was used to solve for the specific heat of the coolant and freestream.

$$ACR = \frac{c_{p_c}\rho_c U_c}{c_{p_\infty}\rho_\infty U_\infty} = \frac{c_{p_c}}{c_{p_\infty}} * \frac{\dot{m}_{c,req} A_\infty}{A_c \dot{m}_\infty} \tag{31}$$

The vacuum pump and mass flow controllers described in Section 3.1.2 set the flow rate out of the film cooling holes by limiting the coolant flow rate out of the cooling assembly. The equivalent flow of one extra row of holes and two extra rows of holes was added to the total coolant flow and drawn from the cooling assembly by the vacuum pump to simulate the coolant traveling to extra rows of holes. Table 5 shows the coolant flow rates for all cases. Simulating extra coolant rows resulted in larger coolant flow rates in the primary channel and coolant flow in the return section of the serpentine channel. For the cases with no extra rows, the second mass flow controller was set to 0.0 SLPM and all of the coolant was ejected through the film cooling holes. As a result of the mass flow controller setting the flow rate into the cooling assembly being limited to 50 SLPM and the mass flow controller setting the flow rate out of the assembly being limited to 30 SLPM, several of the cases listed in Table 5 were not possible.

3.4.2 IR Thermography Method

IR thermography, discussed in Section 2.6.1, was used to record the surface temperature of the airfoils. The temperature measurements were then used to calculate

overall effectiveness, discussed in Section 3.4.4. Figure 63 shows the area of the test surface that was visible by the IR camera, represented by the red circle, and shows a raw IR image, where the camera recorded radiation counts. In Figure 63, the surface thermocouples are highlighted by the yellow squares. To achieve this image, the camera was mounted approximately two feet from the FCR and tilted until the window was in view. The camera focus was then adjusted until the image was clear. The camera was focused during the spatial calibration to ensure that the calibration grid was visible and then the focus was not adjusted again.

Table 5. Coolant flow rates used to achieve desired blowing ratios for $Re = 10K$ and $Re = 15K$. Cases highlighted in red were not possible due to limitations of mass flow controllers.

Blowing Ratio	ACR	$\dot{m}_c$[SLPM] for $Re_D = 10k$		$\dot{m}_c$[SLPM] for $Re_D = 15k$		Simulated Extra Rows
		$\dot{m}_{c,in}$	$\dot{m}_{c,out}$	$\dot{m}_{c,in}$	$\dot{m}_{c,out}$	
0.25	0.25	3.65	0.0	5.47	0.0	0
0.25	0.25	7.30	3.65	10.9	5.47	1
0.25	0.25	11.0	7.30	16.4	10.9	2
0.50	0.49	7.30	0.0	10.9	0.0	0
0.50	0.49	14.6	7.30	21.8	10.9	1
0.50	0.49	21.9	14.6	32.7	21.8	2
0.75	0.73	10.9	0.0	16.4	0.0	0
0.75	0.73	21.8	10.9	32.8	16.4	1
0.75	0.73	32.7	21.8	49.2	32.8	2
1.0	0.97	14.6	0.0	21.9	0.0	0
1.0	0.97	29.2	14.6	43.8	21.9	1
1.0	0.97	43.8	29.2	65.7	43.8	2
1.5	1.45	21.9	0.0	32.8	0.0	0
1.5	1.45	43.8	21.9	65.6	32.8	1
1.5	1.45	65.7	43.8	98.4	65.6	2
2.0	1.93	29.2	0.0	43.8	0.0	0
2.0	1.93	58.4	29.2	87.6	43.8	1
2.0	1.93	87.6	54.4	131.4	87.6	2

The software for the IR camera had a built-in temperature conversion, but the

in-situ calibration technique introduced in Section 2.6.1 was used to convert the IR counts to temperatures. The IR calibration allowed for the emissivity of the test surface and transmissivity through the sapphire window to be accounted for. The calibration was conducted by increasing the freestream temperature in steps while approaching the desired freestream temperature and allowing the temperature to level off at each step. For example, if the desired freestream temperature for test data was 650 K, calibration points were taken in increments of 30 K starting at 500 K with the coolant flow off. At each calibration point, the freestream temperature was held constant for approximately thirty minutes to allow the facility to reach steady state. All of the hardware from the wall heaters to the test section were required to reach a steady temperature before the airfoil surface temperature could reach steady state.

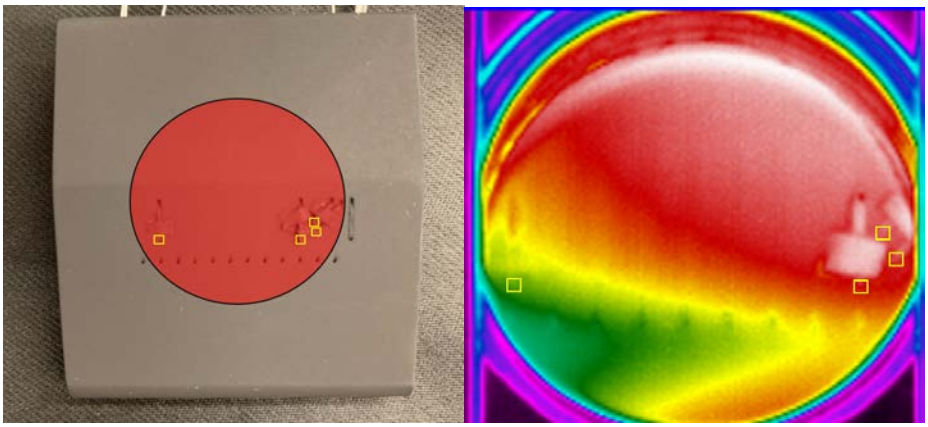

(a) Airfoil surface viewing Area (b) Raw IR Image

Figure 63. Airfoil surface viewing area and raw IR image for $Re = 10k, ACR = 0.49$ (no extra rows of holes).

At each calibration point, the IR camera recorded 120 frames over 2 seconds at 60 Hz and stored the count values by pixel as .csv files. The 120 frames were averaged into a single image to account for any minor vibrations of the image that could have been the result of unsteady flow through the rig. On average, the count value at each pixel would fluctuate between $+/-0.5\%$ of the average value. At the same time,

the temperature readings from the surface thermocouples were recorded at 20 Hz by the FCR LabVIEW program. During acquisition, the thermocuople readings would fluctuate between 0.1-0.5K.

A MATLAB code read in the temperature data from the four surface thermocouples and paired them to the intensity data from the IR image. The locations of the thermocouples were identified by hovering the cursor over the location of the thermocouple in the image and recording the pixel location. The MATLAB code then used intensity data from four pixels around the thermocouple tip, represented by the four corners of the yellow squares in Figure 63b, to avoid conduction/paint issues with the thermocouple. As noted by Lynch [5], identifying the thermocouple locations on the IR image and inputting them into the MATLAB code could be tricky. The (0,0) origin of the IR image was in the top left corner, while the (0,0) origin in the MATLAB code was in the bottom left corner. To obtain the correct y-coordinate to input into the code, the y-coordinate from the IR image had to be subtracted from the total number of pixels in the vertical direction.

After the thermocouple and IR count values were paired up, the code then plotted a calibration curve and calculated a curve fit. The curve fit was a biquadratic equation, also known as a quartic equation, with a constant. An example calibration curve for a freestream temperature of 650K is shown in Figure 64. IR calibrations were conducted on multiple days and the resulting curves were compared to determine if it was necessary to calibrate the IR camera on each day of testing. Figure 65 shows the IR calibration curves for three days of testing, including different hole shapes and freestream turbulence levels. The curves collapsed on each other, indicating that it was not necessary to conduct an IR calibration on each testing day.

It was important to keep the IR camera's integration time the same between the time of the IR calibration and each round of testing. The integration time, listed

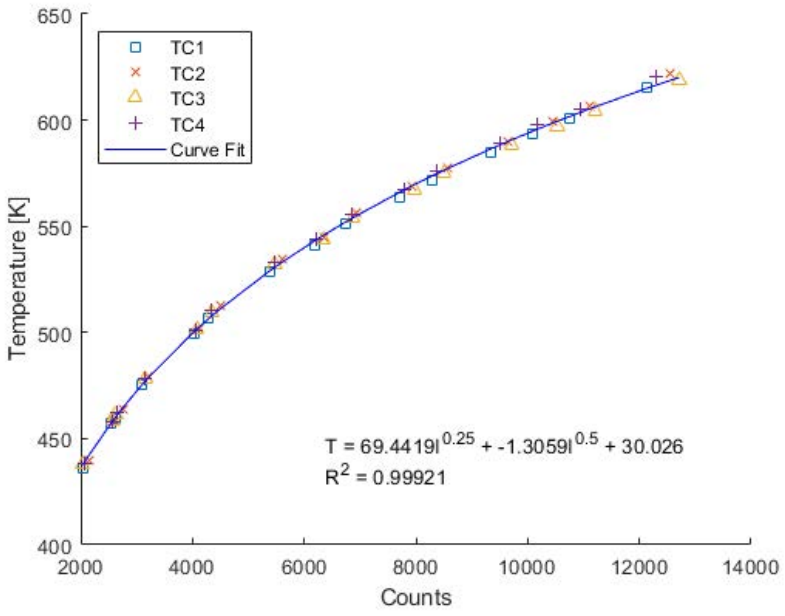

Figure 64. Sample IR calibration curve for $T_\infty = 650K$.

as "Cal/Int" in the camera software, was similar to the light sensitivity setting for a normal camera. Initial testing revealed that a Cal/Int setting of 0.02 was best suited for freestream temperatures of $550K$ and $650K$. Larger integration times resulted in the airfoil surface not being visible in the IR image once the surface heated up. Since the calibration curves collapsed on each other if the cal/int setting was kept the same, the calibration curve in Figure 64 was used for $T_\infty = 550K$ and $T_\infty = 650K$ test cases. The integration times and resulting uncertainties for the three freestream temperatures of interest are summarized in Table 6. The uncertainties were calculated by taking the standard deviation of the differences between the thermocouple temperature measurements and the temperatures determined by the curve fit. The standard deviation was then multiplied by the inverse CDF of the Student's T distribution for a 95% confidence interval, resulting in the uncertainty values seen in Table 6. The uncertainty values are for the calibration curve used to convert radiation counts to surface temperatures. For consistency, one curve was used for each

freestream temperature range since the curves collapsed on top of each other and a calibration for each testing day was not necessary. Figure 66 shows a contour plot of surface temperature for the cylindrical holes at $Re = 10k$ and $ACR = 0.49$.

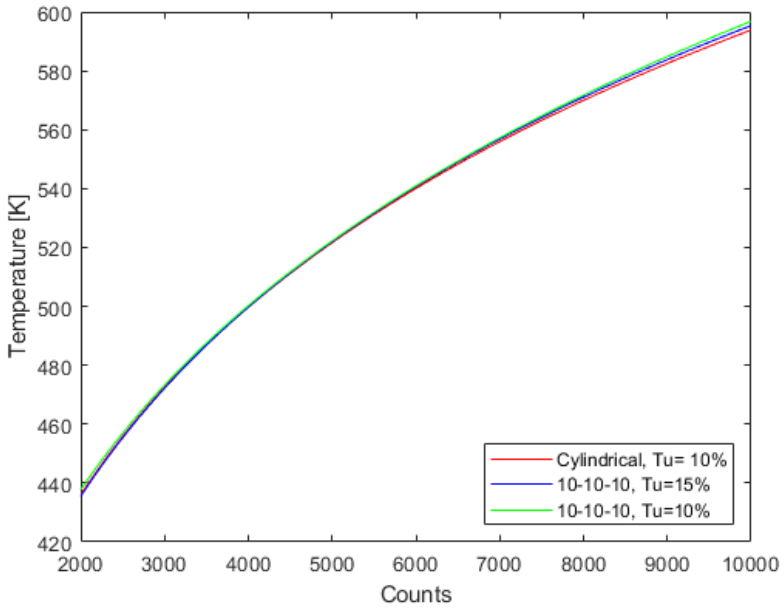

Figure 65. IR calibration curves for three different rig configurations.

Table 6. IR camera calibration settings and uncertainty for the three freestream temperatures of interest.

T_∞ [K]	Cal/Int	Uncertainty [K]
450	0.07	1.94
550,650	0.02	2.92

3.4.3 Spatial Calibration

The IR image had to be spatially calibrated to create a two-dimensional contour plot due to the viewing angle of the IR camera. The spatial calibration, similar to the process used by Lynch [5] and Tewaheftewa [31], involved tracing a printed 1/16" grid with a fine pen and attaching the grid to the airfoil surface, shown in Figure 67. The difference in material and color between the ink and the paper resulted in a

radiative difference that allowed the grid to be visible by the IR camera when heat was applied to the surface, also shown in Figure 67.

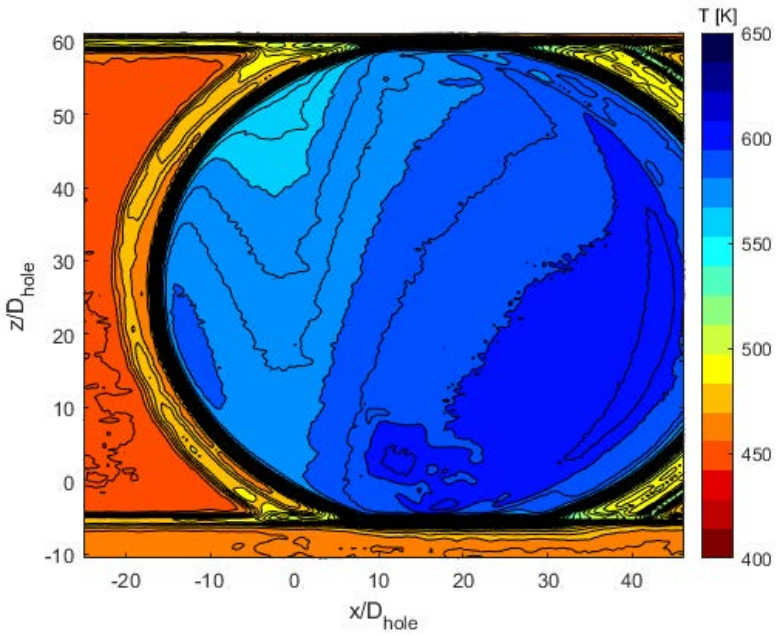

Figure 66. Temperature contour plot for $Re = 10k, ACR = 0.49$ (no extra rows of holes).

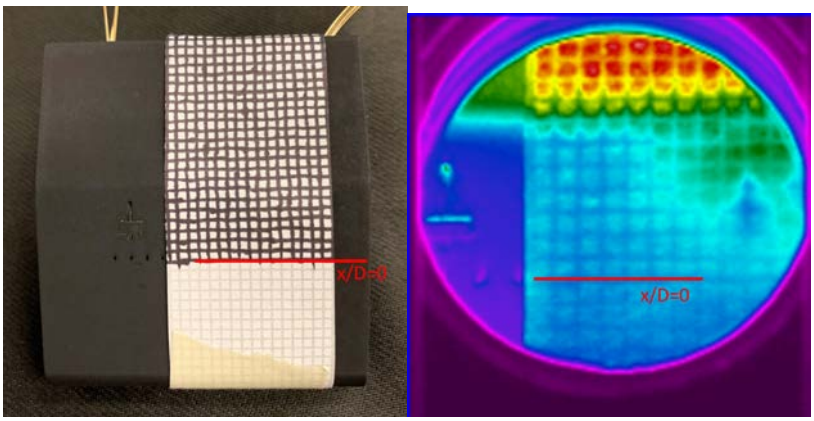

(a) Calibration Grid on Airfoil (b) Raw IR Image During Calibration

Figure 67. Spatial calibration grid attached to airfoil surface and raw IR image taken during spatial calibration.

The pixel locations of the grid lines were inputted into the calibration code and a linear equation was used to curve fit the spatial data in the x-direction and z-direction.

Figure 68 shows the curve fits used to convert pixels to x/D_{hole} and z/D_{hole}. An example image from testing that has been spatially calibrated is shown in Figure 69. During each round of testing, the pixel location of $x/D_{hole} = 0$ was recorded and then inputted into the spatial calibration code to adjust the spatial calibration. This allowed the spatial calibration to correctly calculate x/D_{hole} and z/D_{hole} for each image.

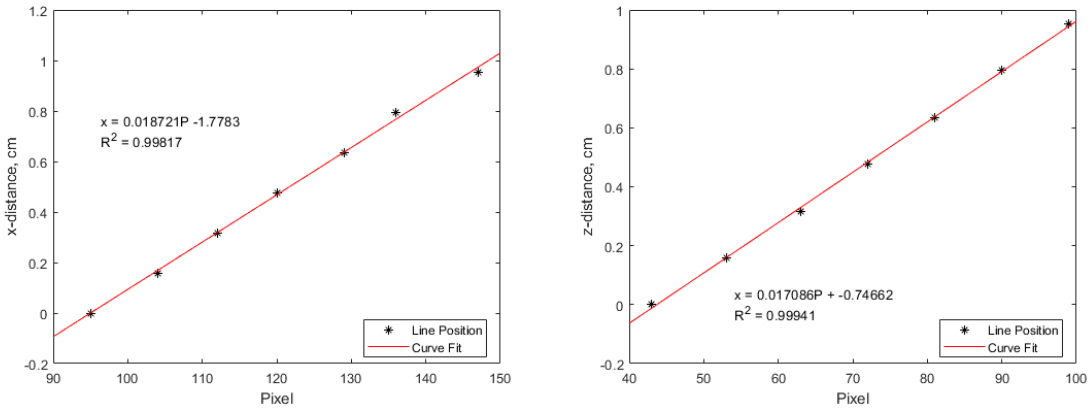

(a) x-direction (b) z-direction

Figure 68. Spatial calibration curves.

3.4.4 Overall Effectiveness

Once the raw IR data was both thermally calibrated and spatially calibrated, Equation 4 was used to solve for overall effectiveness, ϕ, at each pixel. In Equation 4, T_∞ was the freestream temperature measurement from the thermocouple in Figure 55, T_s was the surface temperatures from the IR calibration, and $T_{c,i}$ was the internal coolant temperature from the first internal thermocouple in Figure 56. A MATLAB code used the freestream temperature, the coolant temperature, and the surface temperatures to create contour plots of ϕ. Figure 70 shows an example ϕ contour plot with the internal channel and film cooling holes overlaid on top. Figure 71 shows the same contour plot zoomed into the area of interest for comparing data.

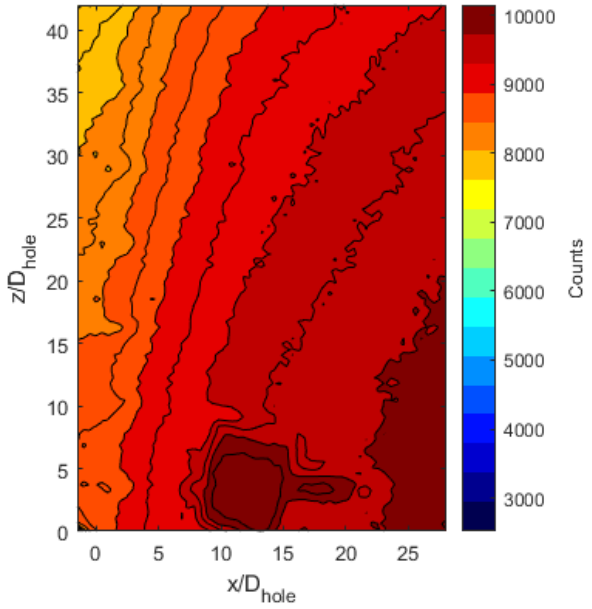

Figure 69. Sample spatially calibrated image for $Re = 10k, ACR = 0.49$ (no extra rows of holes).

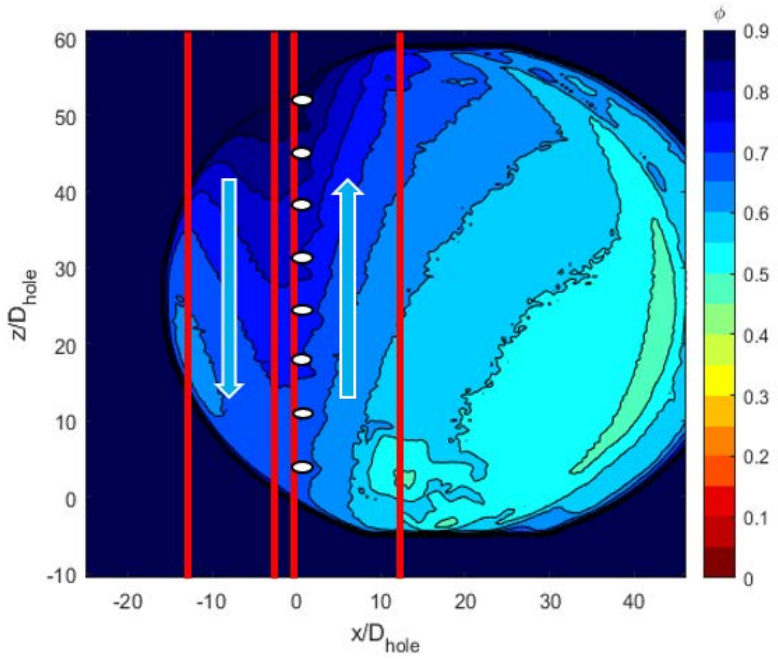

Figure 70. Sample contour plot of ϕ for $Re = 10k, ACR = 0.49$ (no extra rows of holes), $Tu \approx 2\%$.

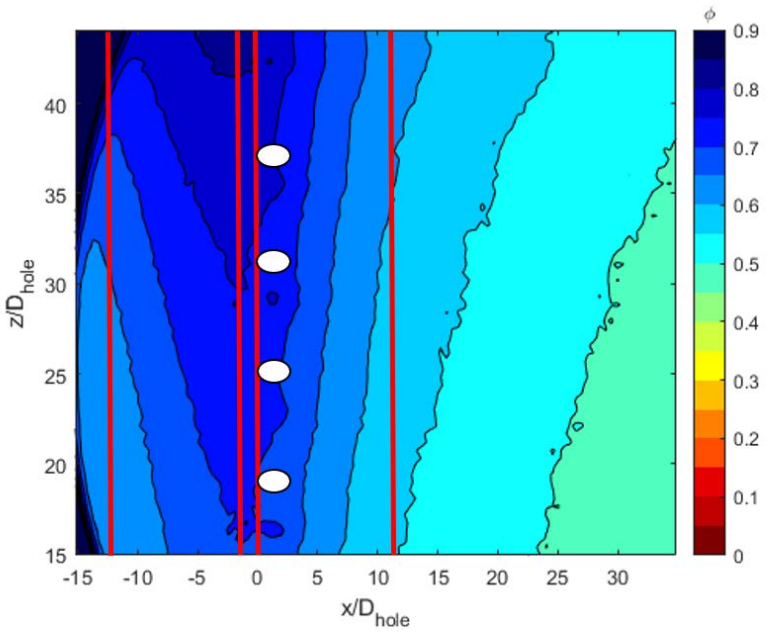

Figure 71. Zoomed contour plot of ϕ for $Re = 10k, ACR = 0.49$ (no extra rows of holes), $Tu \approx 2\%$.

3.5 Estimation of Heat Transfer Coefficients

There are many factors that can affect the overall film cooling effectiveness, including the heat transfer coefficients on the external surface of the airfoil and the heat transfer coefficients in the coolant channel. Any changes to the internal or external heat transfer coefficients can be used to predict a change in overall effectiveness. In the FCR, changes in Re_D and freestream turbulence were used to change the external heat transfer coefficient. The internal heat transfer coefficient was altered by simulating extra rows of coolant holes and changing the coolant flow rate through the channel. For this research, heat transfer coefficients were calculated for the external airfoil surface and internal coolant channel using correlations found in Kays et al [37]. The heat transfer coefficients were then plugged into a new equation, developed in Section 3.6, to estimate the expected change in overall effectiveness from increasing the external or internal heat transfer coefficients.

3.5.1 External Heat Transfer Coefficient

The correct correlation to use depended on whether the boundary layer on the surface of the airfoil was laminar or turbulent and was based on the freestream Reynolds number, shown in Equation 32

$$Re_x = \frac{u_\infty x}{\nu} \tag{32}$$

where u_∞ is the freestream velocity at the location of the film cooling holes, ν is the kinematic viscosity of the fluid, and x is the distance from the beginning of the flat plate portion of the airfoil to the location of interest. As mentioned in Section 3.4, the freestream massflow rate and cross-sectional area above the airfoil were used to determine the freestream velocity at the location of the film cooling holes. The Reynolds number was then set by setting the freestream massflow to the required value based on the density of the freestream, the desired freestream velocity, and the cross-sectional area above the airfoil. For this research, $x/D_{hole} = 0$ was located 1.8 cm from the beginning of the flat plate. The two freestream flowrates used in this research, for $Re_D = 10k$ and $Re_D = 15k$, resulted in freestream velocities of $61m/s$ and $91m/s$, respectively. These velocities resulted in flat plate Reynolds Numbers of $Re_x = 19,000$ and $Re_x = 28,000$ at the location of the film cooling holes. The length scale and velocity scale for Re_x were x and the freestream velocity above the plate, respectively. Both of these Reynolds Numbers were below the critical Reynolds number of $60,000$ for transition to turbulent flow [37]. Although this would mean laminar flow in a theoretical situation, it is likely that the boundary layer was tripped to turbulent as the flow traveled over the cylindrical leading edge of the airfoil. For this reason, calculations were done for laminar and turbulent boundary layers to compare to the data.

For cases without the turbulence generator installed, the heat transfer solution

for a laminar external boundary layer with constant freestream velocity flow along a constant-temperature semi-infinite plate, found in Kays et al. [37] and shown in Equation 33, was employed.

$$Nu_x = 0.332 Pr^{1/3} {Re_x}^{1/2} \tag{33}$$

The correlation uses the Prandtl Number, Pr, and the local Reynolds Number at the surface location of interest to estimate the local Nusselt Number, Nu_x, shown in Equation 34.

$$Nu_x = \frac{h_x x}{k_f} \tag{34}$$

where h_x is the local heat transfer coefficient, x is the characteristic length, and k_f is the thermal conductivity of the fluid above the surface. The freestream temperature measurement at the location of the film cooling holes was used to interpolate the thermal conductivity of the freestream air [6]. With the thermal conductivity of the fluid known, the heat transfer coefficient could be solved for at any location on the airfoil.

For cases with the turbulence generator installed, the turbulent external boundary correlation for constant freestream velocity and constant surface temperature, found in Kays et al. [37] and shown in Equation 35, was used to estimate the Stanton Number, St. As previously mentioned, this correlation was also used for cases without the turbulence generator installed in case the boundary layer was tripped to turbulent. Equation 36 [37] was then used to solve for the Nusselt Number and as before, the Nusselt Number was used to solve for the external heat transfer coefficient.

$$St = \frac{0.0287 Re_x^{-0.2}}{0.169 {Re_x}^{-0.1}(13.2Pr - 9.25) + 0.85} \tag{35}$$

$$St = \frac{Nu_x}{Re_x Pr} \tag{36}$$

3.5.2 Internal Heat Transfer Coefficient

As with the external heat transfer correlation, the correct correlation to use for the internal heat transfer coefficient depended on whether the flow inside the coolant channel was laminar or turbulent. The Reynolds number based on the hydraulic diameter, Re_{D_h} is shown in Equation 37.

$$Re_{D_h} = \frac{D_h G}{\mu} \tag{37}$$

where

$$G = \frac{\dot{m}_{c,req}}{A_c} \tag{38}$$

and

$$D_h = \frac{4A_c}{P} \tag{39}$$

In Equations 38 and 39, $\dot{m}$ is the massflow through the channel, A_c is the cross-sectional area of the channel, and P is the wetted perimeter of the channel. The channel dimensions shown in Figure 50 resulted in $A_c = 10.3mm^2$, $P = 13.2mm$, and $D_h = 3.12mm$. For this research, cases with Reynolds numbers less than 2,300 were considered to be laminar while cases with Reynolds numbers above 2,300 were considered to be turbulent.

The constant-temperature heat transfer solution for laminar internal flow found in Kays et al. [37] states that the Nusselt number is 3.66. Using the hydraulic diameter and the given Nusselt number, Equation 34 was used to solve for the heat transfer coefficient within the coolant channel.

For the turbulent cases, the heat transfer solution for fully-developed flow within

a circular tube at constant surface temperature [37], shown in Equation 40 was used to estimate the Nusselt number.

$$Nu = 0.021 Pr^{0.5} Re^{0.8} \tag{40}$$

3.6 New Overall Effectiveness Equation

Equation 5 has been used to predict changes in overall effectiveness due to variations in parameters such as Biot number, internal heat transfer coefficient, and external heat transfer coefficient. In the development of Equation 5, the convective heat flux at the surface was assumed to be equal to the conductive heat flux through the wall. As seen by Vorgert [4], there are additional conduction paths through the model that affect the overall effectiveness. For this investigation, a similar overall effectiveness equation was developed and includes a second conduction path to the side wall of the airfoil. The process of developing the new equation followed the process that is detailed in Rutledge et al. [8], but contained additional terms to account for an additional conduction path. Assuming that the convective heat flux at the surface equates to the conductive heat flux through the wall and the conductive heat flux to the temperature of the airfoil's side wall

$$h_f(T_{aw} - T_s) = \frac{k}{L_1}(T_s - T_i) + \frac{k}{L_2}(T_s - T_w) \tag{41}$$

Where T_{aw} is the adiabatic wall temperature, T_s is the surface temperature, k is the thermal conductivity, T_i is the airfoil's internal temperature, L_1 is the thickness of the airfoil above the coolant channel, T_w is the temperature of the airfoil's side wall, and L_2 is the distance to the side wall. Arranging to solve for the internal temperature

$$T_i = T_s - \frac{h_f L_1}{k}(T_{aw} - T_s) + \frac{L_1}{L_2}(T_s - T_w) \tag{42}$$

Substituting in the Biot number

$$T_i = T_s - Bi(T_{aw} - T_s) + \frac{L_1}{L_2}(T_s - T_w) \tag{43}$$

The airfoil is assumed to be at steady state, so the external convection must match the sum of the internal convection and the conduction to the side wall. Assuming that the heat flux through the wall is equal to the internal convection

$$h_f(T_{aw} - T_s) = h_i(T_i - T_c) + \frac{k}{L_2}(T_s - T_w) \tag{44}$$

The surface temperature of the airfoil can then be written

$$T_s = \frac{T_{aw}(h_f + h_i Bi) + T_w(h_i \frac{L_1}{L_2} + \frac{k}{L_2}) + h_i T_c}{h_i(1 + Bi + \frac{L_1}{L_2}) + h_f + \frac{k}{L_2}} \tag{45}$$

The surface temperature can then be nondimensionalized according to Equation 4 to yield

$$\phi = \frac{(T_\infty - T_{aw})(\frac{h_f}{h_i} + Bi) + (T_\infty - T_w)(\frac{L_1}{L_2} + \frac{k}{h_i L_2}) + (T_\infty - T_c)}{(T_\infty - T_c)(1 + Bi + \frac{L_1}{L_2} + \frac{h_f}{h_i} + \frac{k}{h_i L_2})} \tag{46}$$

As in Rutledge et al.[8], we can write

$$\frac{T_\infty - T_{aw}}{T_\infty - T_c} = \chi\eta \tag{47}$$

where χ is the coolant warming factor and η is the adiabatic effectiveness. This development introduces a new nondimensional parameter represented by ψ.

$$\psi = \frac{T_\infty - T_w}{T_\infty - T_c} \tag{48}$$

Equation 46 then becomes

$$\phi = \frac{\chi\eta(\frac{h_f}{h_i} + Bi) + \psi(\frac{L_1}{L_2} + \frac{k}{h_i L_2}) + 1}{1 + Bi + \frac{L_1}{L_2} + \frac{h_f}{h_i} + \frac{k}{h_i L_2}} \tag{49}$$

Algebraic manipulation of Equation 49 results in

$$\phi = \frac{\chi\eta(\frac{h_f}{h_i} + Bi) + \psi\frac{L_1}{L_2}(1 + \frac{1}{Bi}\frac{h_f}{h_i}) + 1}{1 + Bi + \frac{h_f}{h_i} + \frac{L_1}{L_2}(1 + \frac{1}{Bi}\frac{h_f}{h_i})} \tag{50}$$

Equation 50 is similar in form to Equation 5, but now has ψ and $\frac{L_1}{L_2}$.

This investigation sought to examine the effects of Reynolds number, freestream turbulence intensity, and internal heat transfer coefficient on overall effectiveness. Equation 49 was used to estimate how much the overall effectiveness should change when varying different parameters. Changing Reynolds number and turbulence intensity was simulated in Equation 49 by varying the external heat transfer coefficient. Changing the internal heat transfer coefficient by simulating extra rows of cooling holes was simulated by varying the internal heat transfer coefficients. Changing the coolant temperature was simulated by altering the new term, ψ. When varying any of these parameters, the resulting change in overall effectiveness from Equation 49 was compared to the experimental results.

3.7 Repeatability

To determine the repeatability of the experimental results, the same test case was run at the beginning and end of a test day. The same test point could not be run every day due to the constant variation in turbulence intensity, length scale, and hole shape from day to day. For this investigation, the repeatability test point at the beginning and end of each test day was and $ACR = 0.49$ with no simulated extra rows of cooling holes. Laterally-averaged overall effectiveness was plotted for the

repeatability points to compare the $\Delta\bar{\phi}$ between the two test points, where $\Delta\bar{\phi}$ is the difference in laterally-averaged overall effectiveness between two points

$$\Delta\bar{\phi} = \bar{\phi}_2 - \bar{\phi}_1 \tag{51}$$

Figure 72 shows the laterally-averaged overall effectiveness for the repeatability test points on three different testing days. The two curves fell on top of each other on each testing day, indicating that the results were repeatable. Over an hour would pass between the first and second repeatability point and the rest of the test cases for the day were run during that time.

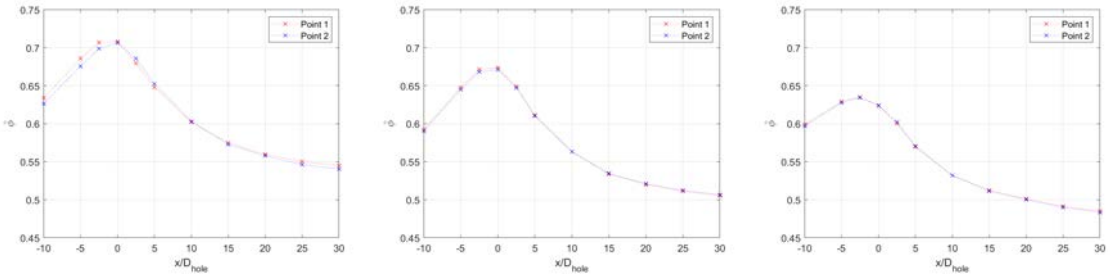

(a) 10-10-10 Hole; $Tu \approx 5\%$ (b) 10-10-10 Hole; $Tu \approx 10\%$ (c) Cylindrical Hole; $Tu \approx 15\%$

Figure 72. Laterally-averaged overall effectiveness versus downstream distance for the two repeatability test points on different testing days.

Figure 73 shows the $\Delta\bar{\phi}$ between the two repeatability test points for the different testing days. The $\Delta\bar{\phi}$ between the two points for $Tu \approx 10$ and $Tu \approx 15$ was never greater than 0.003, showing that the two data sets are nearly identical. The $\Delta\bar{\phi}$ between the two repeatability points at $Tu \approx 5$ was slightly larger upstream of the cooling hole, but was never greater than 0.01. For $x/D_{hole} > 2.5$, the $\Delta\bar{\phi}$ between the two repeatability points for $Tu \approx 5\%$ was never larger than 0.006.

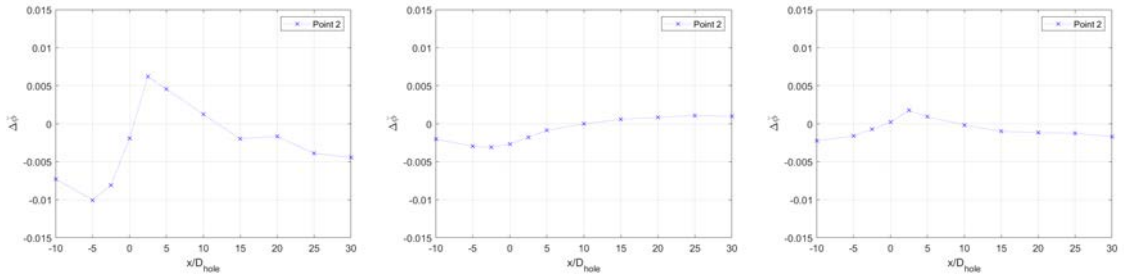

(a) 10-10-10 Hole; $Tu \approx 5\%$ (b) 10-10-10 Hole; $Tu \approx 10\%$ (c) Cylindrical Hole; $Tu \approx 15\%$

Figure 73. $\Delta\bar{\phi}$ between the two repeatability test points on different testing days.

3.8 Uncertainty Analysis

This uncertainty analysis looks at the uncertainty in overall effectiveness for three test cases at different ends of the test matrix. Case 1 consisted of $T_\infty = 450K$, $ACR = 0.49$ (no simulated extra rows), and $Tu \approx 2\%$ for the cylindrical hole. Case 2 consisted of $T_\infty = 550K$, $ACR = 0.97$ (0 simulated extra rows), and $Tu \approx 10\%$ for the 10-10-10 hole. Case 3 consisted of $T_\infty = 650K$, $ACR = 1.45$ (1 simulated extra row), and $Tu \approx 10\%$ for the 10-10-10 hole. Table 7 summarizes the measurements and fluctuations used in the uncertainty analysis.

Table 7. Measurement fluctuations used to calculate overall uncertainty.

Measurement	Case 1	Case 2	Case 3
$\dot{m}_\infty$ [kg/min]	1.20 ± 0.03	1.20 ± 0.03	1.20 ± 0.03
$\dot{m}_c$ [kg/min]	$.0097 \pm 1 * 10^{-5}$	$.019 \pm 1.9 * 10^{-4}$	$.058 \pm 5.8 * 10^{-4}$
T_∞ [K]	450 ± 1	548 ± 1	650 ± 1
T_c [K]	408 ± 0.5	467 ± 0.5	448 ± 0.5
Surface Radiation Counts	4124 ± 21	4463 ± 17	6409 ± 32
T_s [K]	426.2 ± 0.3	511.5 ± 0.4	546.8 ± 0.5

The uncertainty values for the thermocouple measurements were calculated by using the root-sum-square method detailed by Moffat [38] to combine the measurement fluctuations with the thermocouple uncertainty. The uncertainty in T_s was determined by combining the fluctuations in Table 7 with the IR calibration uncertainty

values given in Table 6. Table 8 shows the results of the uncertainty analysis for various parameters including ACR and ϕ. The uncertainty in overall effectiveness was much greater for Case 1 than Cases 2 and 3. Examination of the uncertainty and sensitivity values revealed that the sensitivity values used in the root-sum-square method were large for Case 1 compared to Cases 2 and 3. This was due to the temperatures of the freestream, surface, and coolant being much closer together at the lower temperature regime. The coolant temperature was the driving factor in the uncertainty calculation and would require more accurate measurements or lower coolant temperatures to bring the uncertainty down. As the temperature differences between the freestream, coolant, and surface increased, the uncertainty in overall effectiveness decreased. As a result, the $T_\infty \approx 650K$ cases had the lowest uncertainty in overall effectiveness.

Table 8. Uncertainty analysis results for two different test cases.

	Case 1		Case 2		Case 3	
Parameter	Value	Uncertainty	Value	Uncertainty	Value	Uncertainty
$\dot{m}_\infty$ [kg/min]	1.2	0.032	1.2	0.032	1.2	0.032
$\dot{m}_c$ [kg/min]	0.0097	9.75E-5	0.019	8.2E-4	0.058	8.2E-4
T_∞ [K]	450	1.12	548	1.12	650	1.12
T_c [K]	408	0.707	467	0.707	448	0.707
T_s [K]	426	2.03	512	3.00	547	3.00
ACR	0.49	0.039	0.97	0.037	1.45	0.034
ϕ	0.57	0.187	0.44	0.07	0.51	0.019

IV. Results and Discussion

The first objective of this investigation was to study the effects of freestream turbulence, Tu, on the overall effectiveness of film cooling holes. A cylindrical hole and a laidback fan-shaped hole, referred to as the 10-10-10 hole, were tested at freestream turbulence intensities of $Tu \approx 2\%$, $Tu \approx 5\%$, $Tu \approx 10\%$, and $Tu \approx 15\%$. A sub-objective of this was to study the impact of turbulent length scale on overall effectiveness. The holes were tested at $Tu = 10\%$ and $Tu = 15\%$ with different length scales to investigate the effect that length scale has on overall effectiveness. The second objective of this investigation was to study the effects of Reynolds number and freestream temperature on overall effectiveness. At each freestream turbulence intensity, the holes were tested at freestream Reynolds numbers of $Re_D = 10,000$ and $Re_D = 15,000$, and freestream temperatures of $450K$, $550K$, and $650K$ to study how Reynolds number and freestream temperature affect overall effectiveness. Testing at different freestream temperatures while holding every other parameter constant allowed the impact of the air's thermal properties on film cooling effectiveness to be studied. Keeping the coolant temperature constant and changing the freestream temperature allowed different density ratios and Advective Capacity Ratios to be studied without using different gases. The third objective of this investigation was to investigate the effects of internal convection within the coolant channel and how conduction through the model affects the overall effectiveness. This investigation used an airfoil with an internal coolant channel that was representative of a serpentine channel found in a typical turbine blade. The internal heat transfer coefficient was varied by simulating extra rows of film cooling holes. This allowed the coolant flow within the passage to be varied while maintaining a constant Advective Capacity Ratio out the holes.

Section 4.1 discusses the effect of Advective Capacity Ratio, ACR, on overall ef-

fectiveness. The effect of freestream turbulence on overall effectiveness is discussed in Section 4.2. Section 4.3 details the effect of Reynolds number on overall effectiveness while Section 4.4 talks about the effect of freestream temperature on overall effectiveness. Finally, Section 4.5 reviews how varying the internal heat transfer coefficient by simulating extra rows of cooling holes impacts overall effectiveness for a given ACR.

Table 9 outlines the test cases used to accomplish the objectives of this investigation and includes the freestream temperature, Re_D, and $Tu\%$ used during testing. For the test cases listed, freestream temperature was varied between $450K - 550K$, ACR was varied from $0 - 2.0$, and the number of simulated extra rows of cooling holes varied from $0 - 2$.

4.1 ACR Effects on Overall Effectiveness

The cylindrical hole and 10-10-10 hole were tested without the turbulence generator to serve as baselines for the rest of the test cases. The ACR values listed in this section are for a single row of cooling holes and do not include simulated extra rows of holes. The effects of flowing excess coolant to simulating extra rows of holes with excess coolant are discussed in Section 4.5. As mentioned in Section 3.4.4, $T_{c,i}$ was the internal coolant temperature from the first internal thermocouple in Figure 56 on page 64. The coolant temperature entering the airfoil was initially used for $T_{c,i}$, but doing so resulted in low overall effectiveness values, shown in Figure 74a. In Figure 74a, the internal channel is outlined in red and the film cooling holes are overlaid on top.

Comparing the thermocouple at the coolant entrance to the thermocouple in the internal channel revealed that the coolant temperature was increasing by over $200K$. Table 10 shows the different overall effectiveness values for the same surface temperature that resulted from different coolant temperatures. The two coolant temperatures

Table 9. Test cases for the cylindrical hole and 10-10-10 hole.

Case	Hole Shape	Re_D	$Tu\%$	Length Scale [mm]
Case 1	Cylindrical	$10k$	2	75
Case 2	Cylindrical	$15k$	2	147
Case 3	Cylindrical	$10k$	5	3.47
Case 4	Cylindrical	$15k$	5	4.98
Case 5	Cylindrical	$10k$	10	3.18
Case 6	Cylindrical	$15k$	10	4.05
Case 7	Cylindrical	$10k$	10	4.44
Case 8	Cylindrical	$10k$	10	6.26
Case 9	Cylindrical	$10k$	15	2.37
Case 10	Cylindrical	$10k$	15	4.39
Case 11	Cylindrical	$10k$	15	6.01
Case 12	Cylindrical	$10k$	15	7.45
Case 13	10-10-10	$10k$	2	75
Case 14	10-10-10	$15k$	2	147
Case 15	10-10-10	$10k$	5	3.47
Case 16	10-10-10	$15k$	5	4.98
Case 17	10-10-10	$10k$	10	3.18
Case 18	10-10-10	$15k$	10	4.05
Case 19	10-10-10	$10k$	10	4.44
Case 20	10-10-10	$10k$	10	6.26
Case 21	10-10-10	$10k$	15	2.37
Case 22	10-10-10	$10k$	15	4.39
Case 23	10-10-10	$10k$	15	6.01
Case 24	10-10-10	$10k$	15	7.45

come from the inlet thermocouple shown in Figure 57 and the first internal thermocouple in Figure 56 on page 64. In the 70.3 mm between the inlet thermocouple and the airfoil, the coolant heated up over 200 degrees K. Table 10 shows that this drastic change in coolant temperature resulted in ϕ being over 0.5 higher for the same surface temperature. Due to the definition of $T_{c,i}$ being the temperature of the coolant before entering the film cooling hole, it was more accurate to use the temperature inside the coolant channel as $T_{c,i}$. The drastic heating of the coolant resulted in the density ratio to change from $DR \approx 2$ to $DR \approx 1.2$ in the short distance between the two measurement locations. This significant increase in DR implies that in real turbine

engines, the density ratio of the coolant entering the holes is likely significantly higher than the density ratio at the beginning of the coolant line. Figure 74b shows the ϕ contour plot for the cylindrical hole at $ACR = 0.49$ and $Tu \approx 2\%$ when $T_{c,i}$ was the internal coolant temperature from the first internal thermocouple in Figure 56. The ϕ values are noticeably higher in Figure 74b than in Figure 74a even though they both utilize the same IR image.

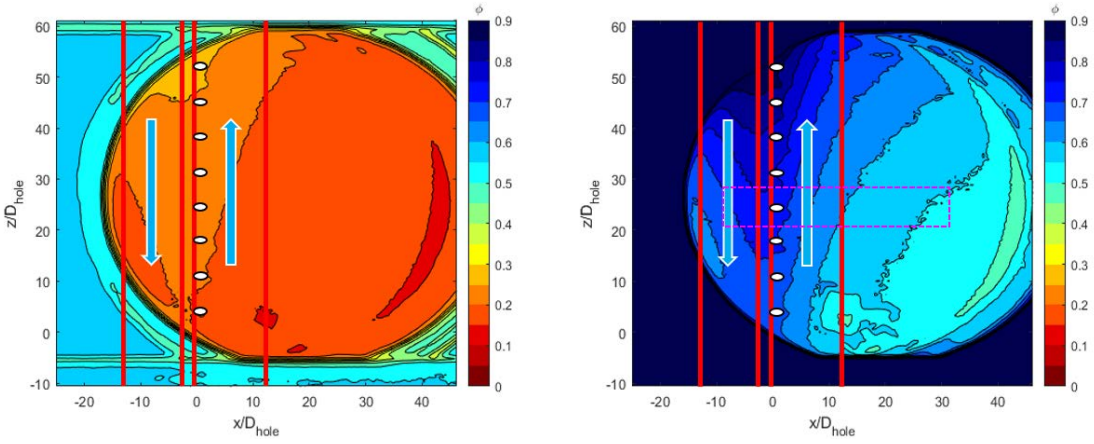

(a) Coolant inlet temp as $T_{c,i}$ (b) Internal channel temp as $T_{c,i}$

Figure 74. Contour plots of ϕ for the cylindrical holes at $ACR = 0.49$ (no simulated extra rows of holes), $Tu \approx 2\%$.

Table 10. Effects of coolant temperature on overall effectiveness.

$T_{c,i}$ $[K]$	T_s $[K]$	ϕ
313	572	0.23
550	572	0.78

In Figure 74b, the flow of coolant through the internal channel is labeled with the blue arrows and is evident by the wedge-shaped contours of elevated overall effectiveness. The coolant immediately began to cool the surface of the airfoil when it entered due to internal convection within the channel and conduction within the model. Interestingly, the coolant jets are not evident in the contour plots as they are in typical contour plots of adiabatic effectiveness. As discussed in Section 2.1, the inclusion

of conduction is what differentiates overall effectiveness from adiabatic effectiveness. The flow of coolant being evident in the contour plots of ϕ while the film cooling jets are not apparent indicates that the internal cooling dominated the external cooling. The impact of the internal cooling and subsequent conduction throughout the airfoil is shown by the overall effectiveness gradually decreasing as x/D_{hole} increases.

The overall effectiveness peaked at a value of $\phi \approx 0.9$ near the coolant entrance and decreased down the length of the channel due to the coolant warming up as it traveled through the airfoil. The thermocouple reading from the second, third, and fourth internal thermocouple in Figure 56 were $585K$, $582K$, and $565K$, respectively. As seen in Figure 56 on Page 64, the fourth thermocouple was directly in line with the first thermocouple. This shows that the temperature in the channel increased down the length of the channel and then decreased along the back channel, presumably due to conduction through the channel divider impacting the back channel where there was no coolant.

The overall effectiveness was laterally averaged for one pitch from $z/D \approx 22$ to $z/D \approx 28$ from $x/D = -10$ to $x/D = 30$ for each test case. Although the start of the upstream channel started at approximately $x/D = -12$, data from locations further upstream could not be laterally-averaged due to limitations with the camera view. The camera view was later adjusted to capture data further upstream, discussed in Section 4.6. The data were only laterally averaged to $x/D = 30$ because the flat plate portion of the airfoil ended at $x/D \approx 32$. The area used for the laterally-averaged results is highlighted in pink in Figure 74b. Figures 75a and 75b show that $\bar{\phi}$ decreased as ACR was increased. This was the combination of a number of factors. As ACR increased, the coolant mass flow increased and resulted in larger internal heat transfer coefficients and lower coolant temperatures. The lower coolant temperature reduced the internal airfoil temperature and thus the external surface temperature.

Table 11 includes internal heat transfer coefficients, freestream temperatures, coolant temperatures from the first internal thermocouple in Figure 56, surface temperatures from a surface thermocouple, and overall effectiveness values for different values of ACR. Table 11 shows that increasing ACR increased the internal heat transfer coefficient and decreased $T_{c,i}$, leading to reduced ϕ values even though the end result was the desired lower surface temperatures. Interestingly, the heat transfer coefficient slightly decreased when ACR was increased from 0.25 to 0.49. According to the heat transfer analysis discussed in Section 3.5.2, both of these flow rates resulted in laminar flow inside the coolant channel and had the same Nusselt number of 3.66. The thermal conductivity of the coolant decreased as the temperature of the coolant decreased, resulting in a slightly smaller heat transfer coefficient for a constant Nusselt number.

According to Equation 5, increasing ACR from 0.25 to 0.49 should have resulted in ϕ to increase by approximately 0.05. Equation 50 however, predicted a decrease of 0.06 in overall effectiveness when increasing ACR from 0.25 to 0.49 due to the additional conduction path that Equation 49 accounted for. This shows that the numerous conduction paths in the airfoil offset other factors that should have resulted in ϕ to increase and resulted in *phi* to decrease.

Figures 75a and 75b show that $\bar{\phi}$ peaked between $x/D = -2.5$ and $x/D = 0$, where there is no external coolant, and decreased in both directions away from the hole. The entrance of the film cooling holes starts at approximately $x/D \approx -4$, so the surface from $x/D \approx -4$ to $x/D = 0$ was most effected by conduction through the cooling holes. For the cylindrical hole and $ACR = 0.49$, $\bar{\phi}$ started at 0.67 at $x/D = -10$ and gradually increased to 0.73 at $x/D = -2.5$. For the same conditions, $\bar{\phi}$ for the 10-10-10 hole started at 0.70 at $x/D = -10$ and gradually increased to 0.77 at $x/D = -2.5$. The overall effectiveness peaking before the film cooling hole exit was an indication that the internal convection within the channel had a bigger impact

on the surface temperature than the external film cooling jet.

Table 11. Sample internal heat transfer coefficients, coolant temperatures, surface temperatures, and resulting overall effectiveness values for various Advective Capacity Ratios; $Tu \approx 2\%$.

Hole Shape	ACR	$h_i[\frac{W}{m^2K}]$	T_∞	$T_{c,i}[K]$	$T_s[K]$	ϕ
Cylindrical	0	0	650	605	606	0.98
Cylindrical	0.25	52.3	650	571	585	0.82
Cylindrical	0.49	50.8	651	550	572	0.78
Cylindrical	0.73	128	650	533	561	0.76
Cylindrical	0.97	161	650	518	552	0.74
Cylindrical	1.45	220	651	493	539	0.71
Cylindrical	1.92	273	650	472	528	0.69
10-10-10	0	0	651	601	603	0.96
10-10-10	0.25	52.6	650	576	588	0.84
10-10-10	0.49	51.3	649	557	577	0.78
10-10-10	0.73	131	651	543	570	0.75
10-10-10	0.97	164	651	528	562	0.72
10-10-10	1.45	226	650	506	553	0.67
10-10-10	1.92	284	650	488	544	0.65

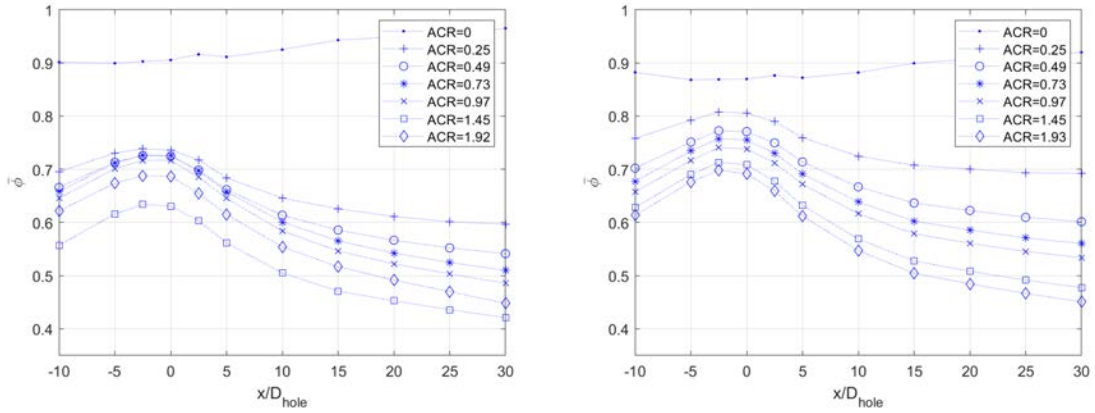

(a) Cylindrical (b) 10-10-10

Figure 75. ACR effects on overall effectiveness for the cylindrical hole and 10-10-10 hole at $Tu \approx 2\%$.

Comparing Figure 75a and Figure 75b showed that the 10-10-10 hole produced higher overall effectiveness values than the cylindrical hole at any given ACR. This was expected, as the 10-10-10 hole allowed the coolant jet to smoothly transition to the

airfoil surface and stay attached longer. Figure 76a is a plot of $\Delta\bar{\phi}$ versus downstream distance between different ACR values for the two holes. For each hole, $ACR = 0.49$ served as a baseline for the $\Delta\bar{\phi}$ comparisons. For both hole shapes, increasing ACR resulted in lower $\bar{\phi}$ values at each downstream distance. Figure 76b shows the $\Delta\bar{\phi}$ between the 10-10-10 hole and cylindrical hole at three ACR values. The $\bar{\phi}$ values for the 10-10-10 hole were approximately 0.05 higher than for the cylindrical hole at an ACR of 0.49, corresponding to a momentum flux ratio of $I \approx 0.20$. For $ACR = 0.97$ ($I \approx 0.73$), the $\bar{\phi}$ values for the 10-10-10 hole were approximately 0.02 - 0.03 higher than for the cylindrical hole in the near-hole region. The $\Delta\bar{\phi}$ between the 10-10-10 hole and cylindrical hole increased as downstream distance increased, presumably due to the 10-10-10 hole keeping the coolant jet attached longer than the cylindrical hole. As ACR was increased to 1.45 ($I \approx 1.5$), the $\Delta\bar{\phi}$ experienced between the 10-10-10 hole and cylindrical hole was almost nonexistent for $x/D < 15$ due to the coolant jets for both holes being separated.

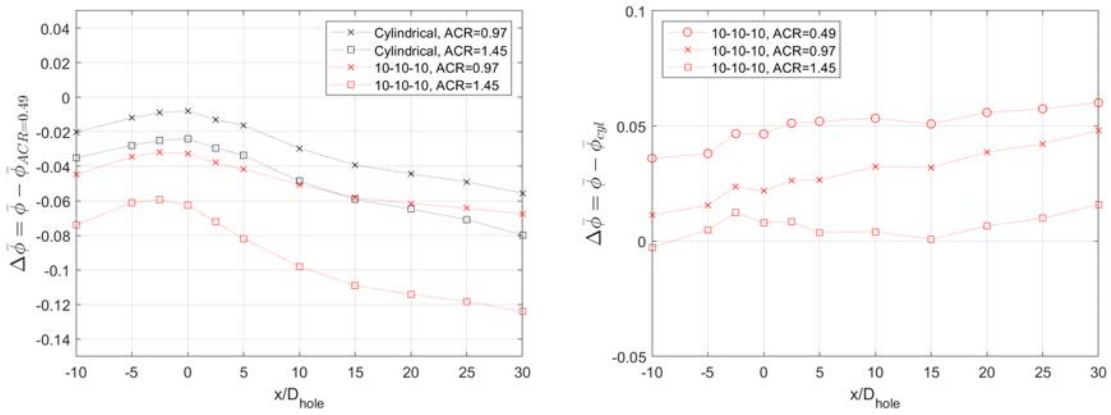

(a) $ACR = 0.49$ as baseline for both holes (b) Cylindrical data as baseline for each ACR

Figure 76. $\Delta\bar{\phi}$ versus downstream distance for the cylindrical hole and 10-10-10 hole at $Tu \approx 2\%$.

4.2 Freestream Turbulence Effects on Overall Effectiveness

The impacts of high freestream turbulence were investigated next. Figure 77 shows the cylindrical hole's ϕ contour plots at $Tu \approx 2\%$ and $Tu \approx 10\%$ for an ACR of 0.97. Again, the ACR values listed in this section are for a single row of cooling holes. While the ϕ contours in Figure 77 have similar shapes, the effectiveness values are visibly lower for the The decrease in overall effectiveness was likely due to the increased external heat transfer coefficient that is associated with high freestream turbulence. According to Equation 49, an increase in h_f would result in a decreased ϕ for a constant η. This is evident by the lower $\bar{\phi}$ values upstream of the film cooling holes, where there is no external cooling and the adiabatic effectiveness would be zero for both cases. $Tu \approx 10\%$ case.

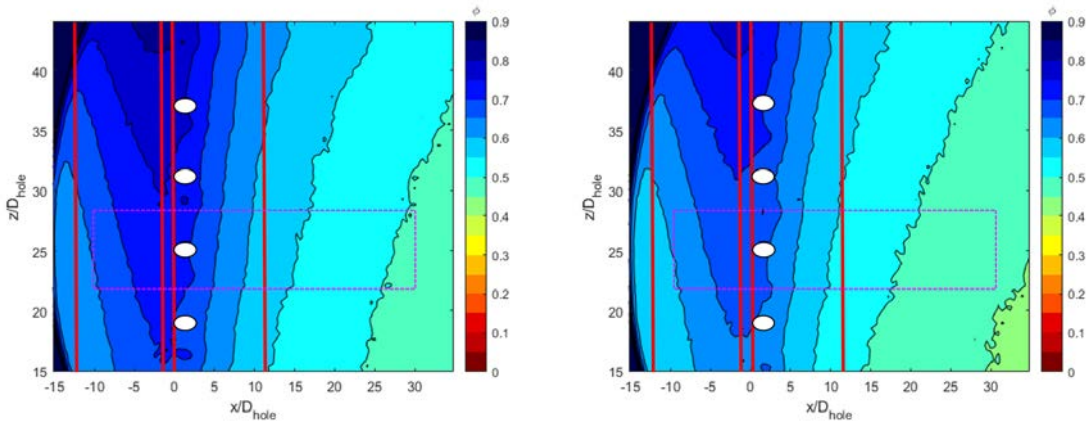

(a) Tu≈ 2% (b) Tu≈ 10%

Figure 77. Contour plots of ϕ for the cylindrical holes at $ACR = 0.97$.

Figure 78 shows laterally-averaged overall effectiveness versus downstream distance for the cylindrical hole at two ACR values and several levels of freestream turbulence intensity. At $ACR = 0.49$, increasing the freestream turbulence intensity to $Tu \approx 5\%$ caused a slight decrease in overall effectiveness upstream of the hole and in the near-hole region. The decrease in overall effectiveness was no more than 0.02,

the experimental uncertainty for $T_\infty = 650K$. Increasing the freestream turbulence intensity to $Tu \approx 10\%$ caused $\bar{\phi}$ to decrease by approximately 0.05 both upstream and downstream of the cooling hole. For an adiabatic effectiveness of zero, Equation 49 predicted a 0.07 decrease in overall effectiveness when increasing the external heat transfer coefficient from $110\frac{W}{m^2K}$ for $Tu \approx 2\%$ to $200\frac{W}{m^2K}$ for $Tu \approx 10\%$. Assuming an adiabatic effectiveness of 0.45 downstream of the cooling hole for a blowing ratio of 0.5 [3], Equation 49 predicted a 0.04 decrease in overall effectiveness when increasing the external heat transfer coefficient from $110\frac{W}{m^2K}$ for $Tu \approx 2\%$ to $200\frac{W}{m^2K}$ for $Tu \approx 10\%$.

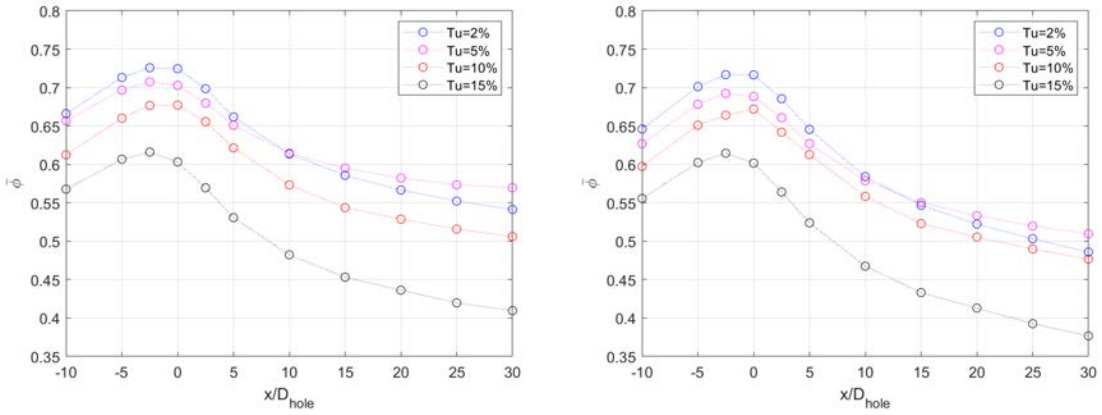

(a) $ACR = 0.49$ (b) $ACR = 0.97$

Figure 78. $\bar{\phi}$ versus downstream distance for the cylindrical hole at various levels of freestream turbulence intensity with original $Tu \approx 15\%$ data.

For $ACR = 0.49$, $\bar{\phi}$ decreased by an additional 0.07 when Tu was increased from 10% to 15%. Figure 78b shows that the decrease in $\bar{\phi}$ near the hole with increasing Tu was similar for $ACR = 0.97$, with $\Delta\bar{\phi} = -0.04$ when increasing Tu to 10% and an additional $\Delta\bar{\phi} = -0.07$ when increasing Tu to 15%. The further decrease in overall effectiveness when increasing the freestream turbulence intensity from $Tu \approx 10\%$ to $Tu \approx 15\%$ was not expected to be as large as it was. The $Tu \approx 15\%$ data was re-run several times to compare the results. The multiple sets of repeat data were compared

to each other and each data set was virtually identical. This led to the conclusion that the original $Tu \approx 15\%$ data was not accurate. Figure 79 shows the same cases as Figure 78, but with the new $Tu \approx 15\%$ data. The new data showed that for $ACR = 0.49$, $\bar{\phi}$ decreased by approximately 0.01 in the near-hole region when the freestream turbulence intensity was increased from $Tu \approx 10\%$ to $Tu \approx 15\%$, which was within the experimental uncertainty. Figure 80 shows the $\Delta\bar{\phi}$ experienced by the cylindrical for $ACR = 0.49$ and $ACR = 0.97$ when increasing the freestream turbulence intensity. Downstream of the hole, there was virtually no difference in overall effectiveness when further increasing the freestream turbulence intensity from $Tu \approx 10\%$ to $Tu \approx 15\%$. For $ACR = 0.97$, the $\Delta\bar{\phi}$ between $Tu \approx 10\%$ and $Tu \approx 15\%$ was approximately 0.02 in the near-hole region and downstream of the cooling hole, again within the experimental uncertainty. Overall, the further increase in freestream turbulence intensity from $Tu \approx 10\%$ to $Tu \approx 15\%$ did not appear to cause a further decrease in overall effectiveness.

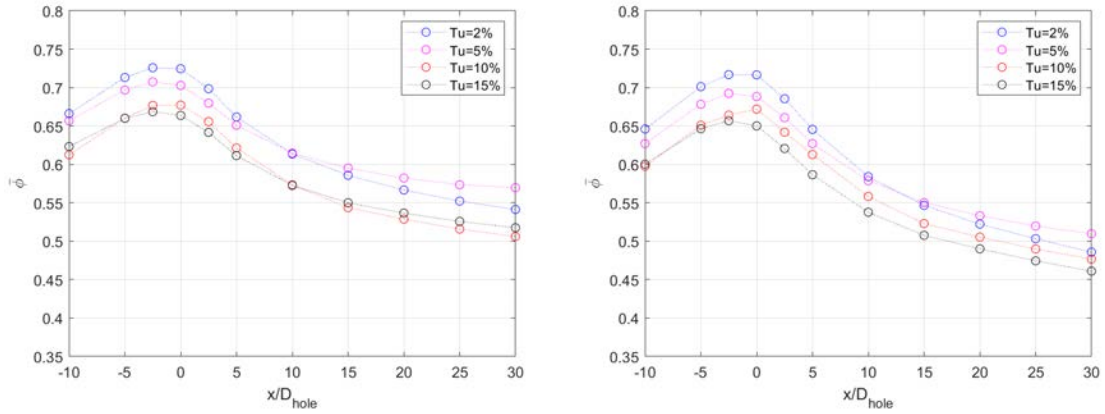

(a) $ACR = 0.49$ (b) $ACR = 0.97$

Figure 79. $\bar{\phi}$ versus downstream distance for the cylindrical hole at various levels of freestream turbulence intensity with repeated $Tu \approx 15\%$ data.

Figure 81 shows the $\Delta\bar{\phi}$ experienced by the 10-10-10 hole for $ACR = 0.49$ and $ACR = 0.97$ when increasing the freestream turbulence intensity. For an ACR of 0.97

and $Tu \approx 2\%$, the overall effectiveness peaked at a value of 0.74 near the hole and dropped to 0.66 when Tu was increased to 10%. Increasing Tu to 15% did not cause a further decrease in $\bar{\phi}$ at the film cooling hole, but decreased ϕ by approximately 0.02 for $x/D > 5$. As with the cylindrical hole the $\Delta\bar{\phi}$ caused by the further increase in freestream turbulence intensity was within the experimental uncertainty.

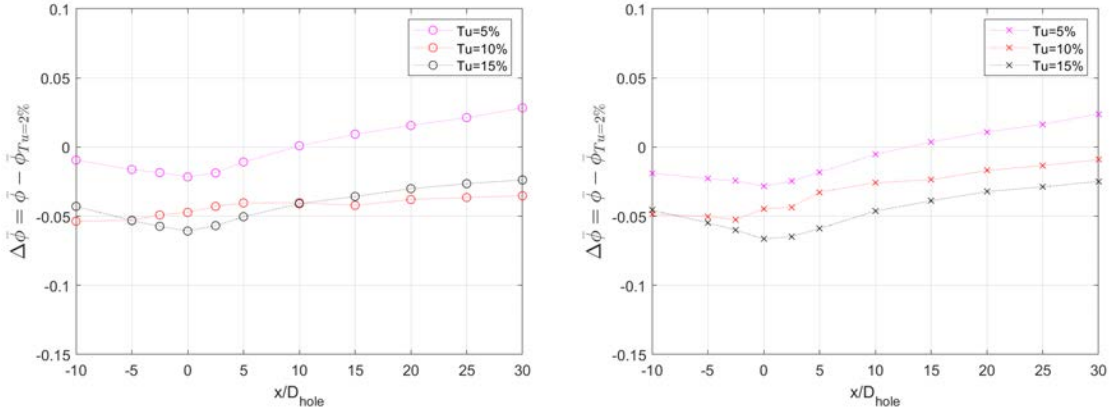

(a) $ACR = 0.49$ (b) $ACR = 0.97$

Figure 80. $\Delta\bar{\phi}$ versus downstream distance for the Cylindrical hole at various levels of freestream turbulence intensity. Baseline: Cylindrical, $Tu \approx 2\%$

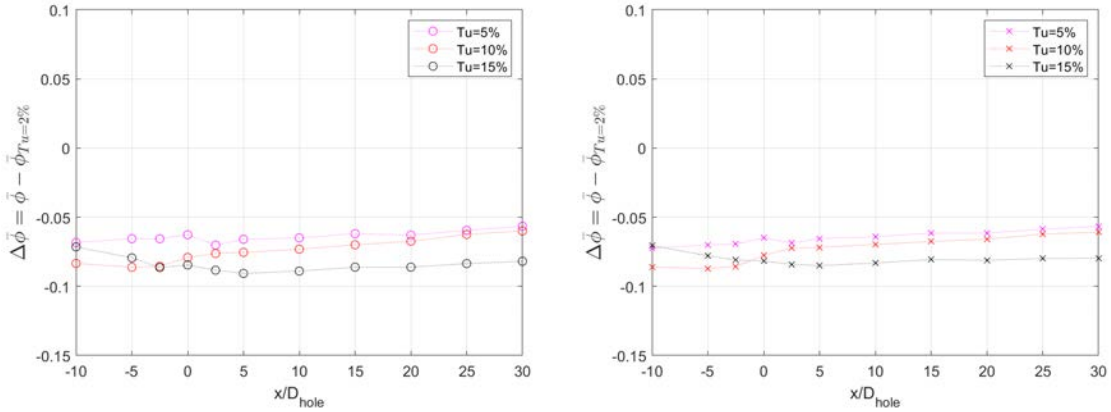

(a) $ACR = 0.49$ (b) $ACR = 0.97$

Figure 81. $\Delta\bar{\phi}$ versus downstream distance for the 10-10-10 hole at various levels of freestream turbulence intensity. Baseline: 10-10-10, $Tu \approx 2\%$

Figure 82 shows $\bar{\phi}$ versus freestream turbulence intensity at several downstream

distances for the 10-10-10 hole at $ACR = 0.49$. The highest $\bar{\phi}$ values occurred at $x/D = 0$ and the next highest $\bar{\phi}$ values occurred upstream of the film cooling holes. The high $\bar{\phi}$ values upstream of the cooling holes were due to the coolant channel beneath the surface. The internal convection within the channel caused the overall effectiveness upstream of the hole to be higher than locations further downstream. Reinforcing the importance of internal convection within the coolant channel is the fact that $\bar{\phi}$ was higher at $x/D = -10$, where there was no external coolant than at $x/D = 10$, where there was external coolant.

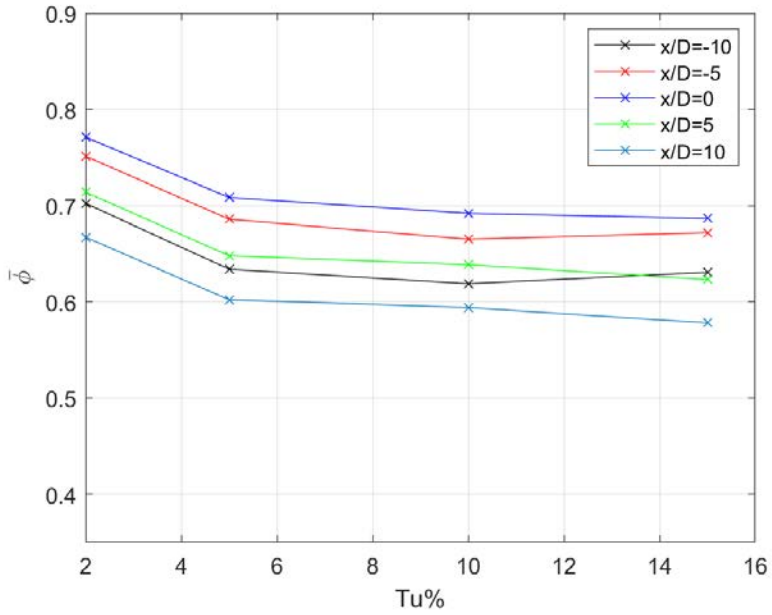

Figure 82. Laterally-averaged overall effectiveness at several downstream distances versus freestream turbulence intensity for the 10-10-10 hole at $ACR = 0.49$.

Figure 83 shows laterally-averaged overall effectiveness at $x/D = 5$ versus freestream turbulence intensity for the 10-10-10 hole at two values of ACR. At both ACR values, the laterally-averaged overall effectiveness decreased by approximately 0.07 when the freestream turbulence intensity was increased from 2% to 5%. The decrease in laterally-averaged overall effectiveness with increasing Tu was minimal after that. At an ACR of 0.49, increasing Tu to 10% and 15% each caused an additional $\Delta\bar{\phi}$ of

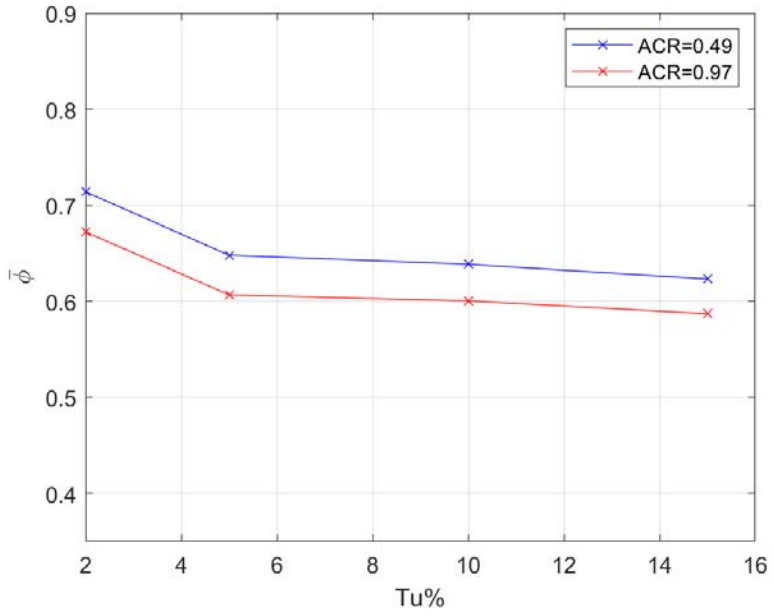

Figure 83. Laterally-averaged overall effectiveness at $x/D = 5$ vs freestream turbulence intensity for the 10-10-10 hole at two ACR values.

approximately -0.01.

Figure 84 shows that at $Tu \approx 2\%$, the $\Delta\bar{\phi}$ provided by the 10-10-10 hole was approximately 0.05 along the length of the airfoil for $ACR = 0.49$. For $ACR = 0.97$ and $ACR = 1.45$, the $\Delta\bar{\phi}$ provided by the 10-10-10 hole increased after $x/D = 10$, possibly due to the 10-10-10 hole's ability to keep the coolant jet closer to the surface longer. The $\Delta\bar{\phi}$ between the 10-10-10 hole and the cylindrical hole was minimal at $Tu \approx 15\%$ for $ACR = 0.49$ and $ACR = 0.97$. For $ACR = 0.49$, the $\Delta\bar{\phi}$ peaked in the near hole region, possibly due to less penetration of the 10-10-10 hole's coolant jet into the freestream, and then decayed to zero. For $ACR = 0.97$, there was virtually no $\Delta\bar{\phi}$ between the cylindrical hole and the 10-10-10 hole. For $ACR = 1.45$, the $\Delta\bar{\phi}$ downstream of the cooling hole was around 0.05 for the length of the airfoil.

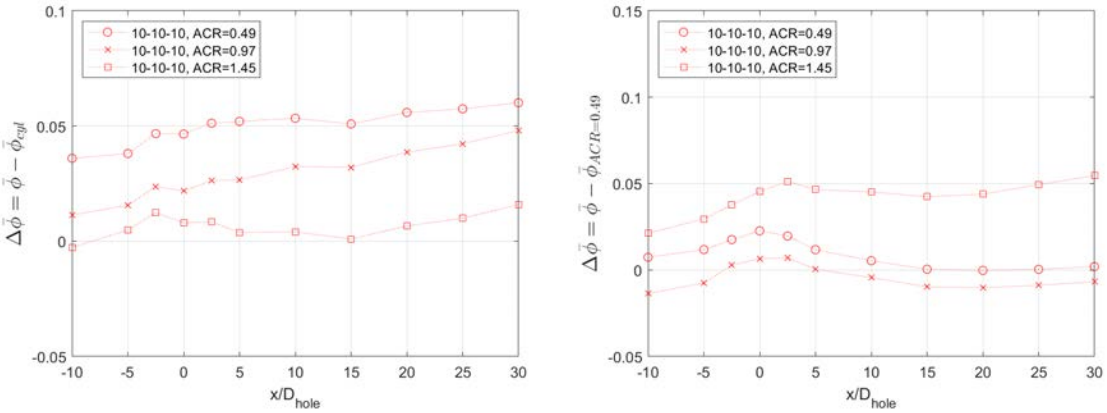

(a) $Tu \approx 2\%$ (b) $Tu \approx 15\%$

Figure 84. $\Delta\bar{\phi}$ versus downstream distance with the cylindrical data as the baseline for each ACR.

4.2.1 Length Scale Effects on Overall Effectiveness

After studying the effects of freestream turbulence on overall effectiveness, the effects of length scale were investigated. As mentioned in Section 3.2.3, the turbulence generator was capable of generating $Tu \approx 10\%$ and $Tu \approx 15\%$ with multiple length scales. Inserts "10", "10 Big", "15", and "15 Big" from Table 3 on Page 56 were used. For $Re_D = 10k$, insert "10" had an integral length scale of $0.32cm$, insert "10 BIG" had an integral length scale of $0.44cm$, insert "15" had an integral length scale of $0.24cm$, and insert "15 BIG" had an integral length scale of $0.60cm$. Figure 85 shows $\bar{\phi}$ versus downstream distance for the cylindrical hole and 10-10-10 hole at $ACR = 0.49$ for both freestream turbulence intensities. Figure 85 shows that for a given freestream turbulence intensity, $\bar{\phi}$ for both holes was reduced when the length scale was increased.

Figure 86 shows the same trend at $ACR = 0.97$. Increasing the length scale for a given freestream turbulence intensity resulted in lower values of overall effectiveness. This is possibly due to the larger length scales enhancing the external heat transfer coefficient. Larger external heat transfer coefficients would increase the amount of

heat that is transferred from the freestream to the airfoil.

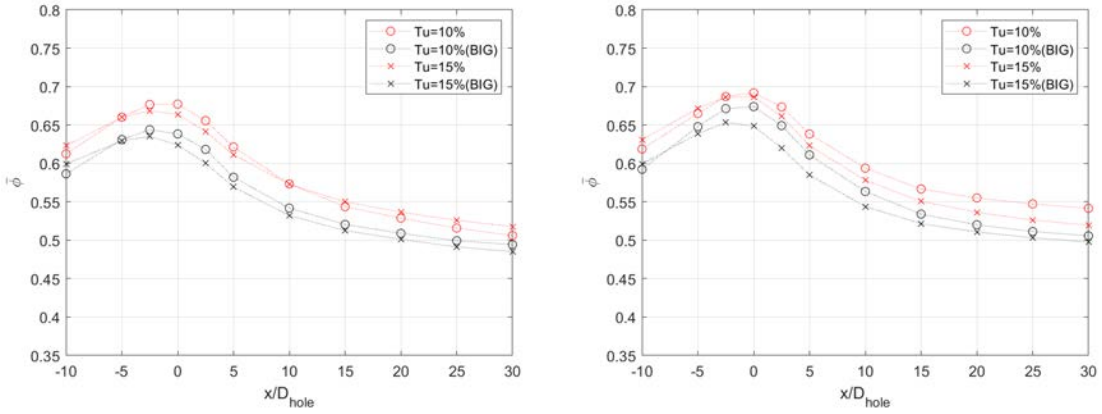

(a) Cylindrical (b) 10-10-10

Figure 85. Effects of length scale on laterally-averaged overall effectiveness versus downstream distance for the cylindrical hole and 10-10-10 hole for $ACR = 0.49$.

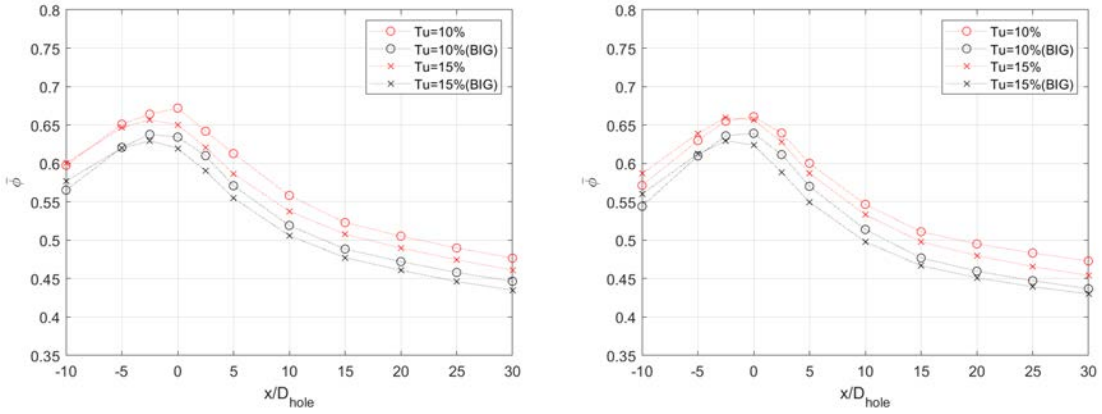

(a) Cylindrical (b) 10-10-10

Figure 86. Effects of length scale on laterally-averaged overall effectiveness versus downstream distance for the cylindrical hole and 10-10-10 hole for $ACR = 0.97$.

4.3 Reynolds Number Effects on Overall Effectiveness

To investigate the effects of Reynolds number on overall effectiveness, the cylindrical hole and 10-10-10 hole were tested at freestream Reynolds numbers of $Re_D = 10 * 10^3$ and $Re_D = 15 * 10^3$. The length scale and velocity scale for Re_D were the

leading edge diameter and the freestream velocity above the film cooling holes. Figure 87 shows $\bar{\phi}$ versus downstream distance for the cylindrical hole at two ACR values and two freestream Reynolds numbers for $Tu \approx 2\%$ and $Tu \approx 10\%$. For both ACR values and turbulence intensities, increasing the freestream Reynolds number resulted in a decrease in overall effectiveness by approximately 0.1 upstream of and near the cooling hole. The decrease in overall effectiveness was likely due to the increased external heat transfer coefficient that resulted from the increased freestream velocity.

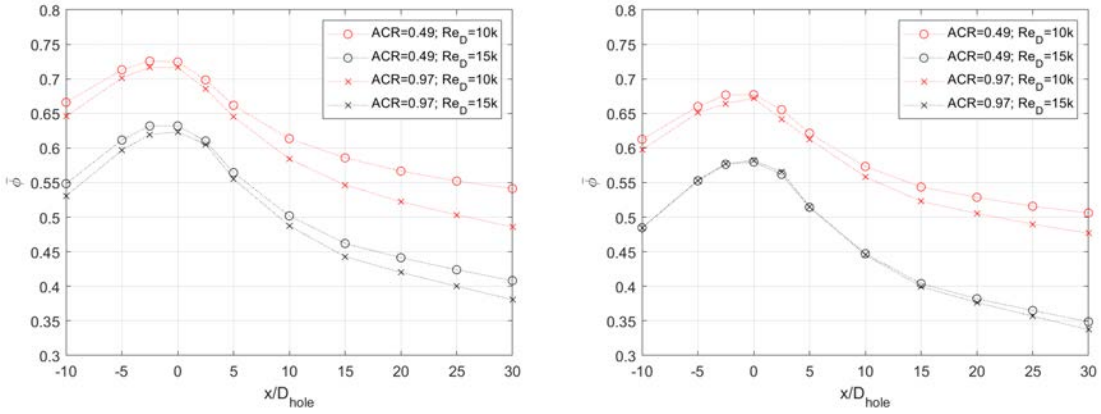

(a) $Tu \approx 2\%$ (b) $Tu \approx 10\%$

Figure 87. Effects of Reynolds number on laterally-averaged overall effectiveness versus downstream distance for the cylindrical hole at $Tu \approx 2\%$ and $Tu \approx 10\%$.

Table 12 lists the external heat transfer coefficients associated with each Reynolds number for laminar and turbulent boundary layers. Increasing the Reynolds number to $Re_d = 15k$ caused the external heat transfer coefficient to increase by approximately $20\frac{W}{m^2K}$ for the laminar case and approximately $60\frac{W}{m^2K}$ for the turbulent case. According to Equation 49, increasing the external heat transfer coefficient from $110\frac{W}{m^2K}$ to $134\frac{W}{m^2K}$ for a constant adiabatic effectiveness resulted in a 0.02 decrease in overall effectiveness. Assuming that the boundary layer is turbulent at $Re_D = 10k$ and $Re_D = 15k$, increasing the external heat transfer coefficient from $166\frac{W}{m^2K}$ to

$229\frac{W}{m^2K}$ for a constant adiabatic effectiveness resulted in a 0.04 decrease in overall effectiveness. Assuming that the boundary layer is laminar at $Re_D = 10k$ and turbulent at $Re_D = 15k$, increasing the external heat transfer coefficient from $110\frac{W}{m^2K}$ to $229\frac{W}{m^2K}$ for a constant adiabatic effectiveness resulted in a 0.08 decrease in overall effectiveness. This value is closer to the 0.1 decrease in overall effectiveness experienced by the cylindrical hole, indicating that the boundary layer may be laminar at $Re_D = 10k$ and turbulent at $Re_D = 15k$. While these estimates for external heat transfer coefficient do not account for enhancement due to the presence of film cooling jets, the general trends agree with the experimental results.

Table 12. Freestream Reynolds numbers and corresponding external heat transfer coefficients for laminar and turbulent cases.

Re_D	laminar $h_e[\frac{W}{m^2K}]$	turbulent $h_e[\frac{W}{m^2K}]$
$10k$	110	166
$15k$	134	229

Figure 88 shows the $\Delta\bar{\phi}$ provided by the 10-10-10 hole over the cylindrical hole for two ACR values and two Reynolds numbers. For each case, the baseline was the cylindrical hole at the same ACR. At $ACR = 0.49$, the 10-10-10 hole consistently provided an approximate 0.04 increase in overall effectiveness at $Re_D = 10k$. At $Re_D = 15k$, the $\Delta\bar{\phi}$ for $ACR = 0.49$ peaked at approximately 0.02 at $x/D = 0$ and then decayed to nearly zero by $x/D = 15$. At $ACR = 0.97$ and $Re_D = 10k$, the $\Delta\bar{\phi}$ provided by the 10-10-10 hole was approximately zero until $x/D = 15$ and then increased due to the hole's ability to keep the coolant jet closer to the surface. At $Re_D = 15k$, the $\Delta\bar{\phi}$ for $ACR = 0.97$ was approximately zero until $x/D = 5$ and then decayed to approximately -0.02. The benefits of the 10-10-10 hole seemed to be minimized or nonexistent at $Re_D = 15k$.

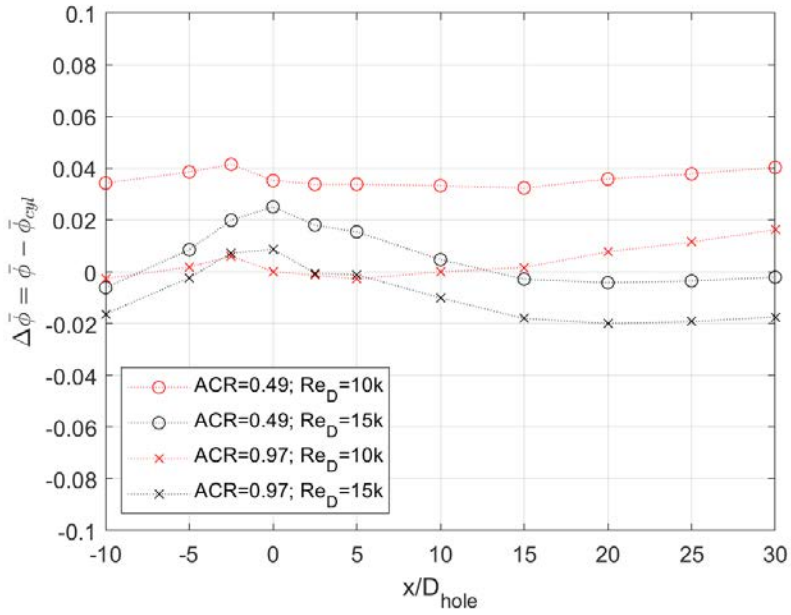

Figure 88. Effects of Reynolds Number on $\Delta\bar{\phi}$ between the 10-10-10 Hole and Cylindrical Hole

4.4 Freestream Temperature Effects on Overall Effectiveness

Film cooling tests were conducted at freestream temperatures of $T_\infty = 450K$, $T_\infty = 550K$, and $T_\infty = 650K$ to study scalability of overall effectiveness measurements between temperature regimes. As freestream temperature changed, ACR and Re_D were kept constant, so the overall effectiveness values were expected to collapse to the same values. Each temperature regime had a different density ratio but ACR was matched because the flow controllers for the freestream and coolant controlled mass flow. As discussed in Section 3.4.1, ACR was determined by setting a blowing ratio and then multiplying the blowing ratio by the specific heat ratio. The specific heat ratio did not change much between temperature regimes, resulting in matched ACR values at the three temperature regimes. Figure 89 shows laterally-averaged overall effectiveness versus downstream distance at different freestream temperatures for the cylindrical hole and freestream turbulence intensities of $Tu \approx 2\%$ and $Tu \approx 10\%$. At

$Tu \approx 2\%$ and $ACR = 0.49$, the overall effectiveness values were very close between the three temperature regimes. For $x/D > 15$, the overall effectiveness values for the three temperture regimes were within 0.01 of each other. The overall effectiveness values were slightly more spread out at $ACR = 0.97$, but stayed within 0.04 of each other. At $Tu \approx 10\%$, the overall effectiveness did not scale as well between the three temperature regimes.

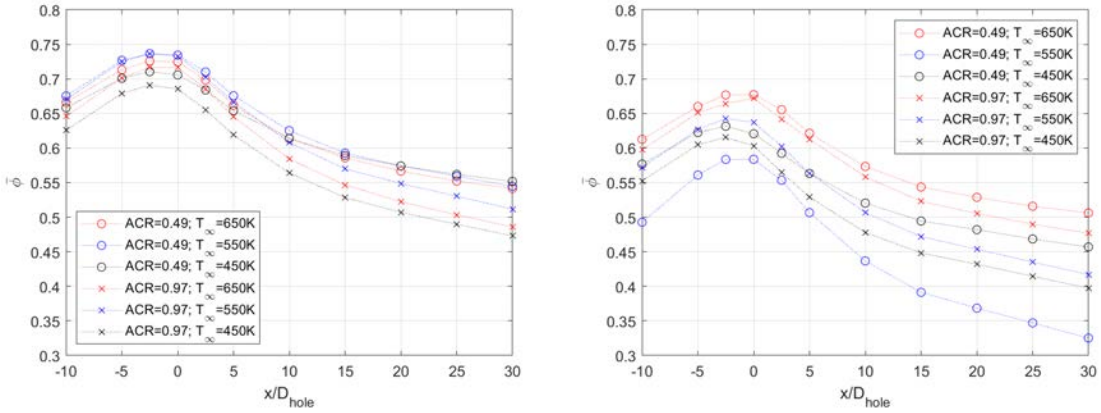

(a) $Tu \approx 2\%$ (b) $Tu \approx 10\%$

Figure 89. Laterally-averaged overall effectiveness versus downstream distance for the cylindrical hole at three freestream temperatures.

Figure 90 shows laterally-averaged overall effectiveness versus downstream distance at different freestream temperatures for the 10-10-10 hole at freestream turbulence intensities of $Tu \approx 2\%$ and $Tu \approx 10\%$. As with the cylindrical hole, the laterally-averaged overall effectiveness was closely matched between freestream temperatures of $550K$ and $650K$ for $Tu \approx 2\%$. For $ACR = 0.49$, the $\Delta\bar{\phi}$ between $650K$ and $550K$ was approximately 0.02 and for $ACR = 0.97$, the $\Delta\bar{\phi}$ between $650K$ and $550K$ was approximately 0.04. The $\Delta\bar{\phi}$ between $650K$ and $450K$ was nearly 0.1 for both ACR values. As discussed in Section 3.8, the uncertainty in overall effectiveness for $T_\infty = 450K$ was about 0.19. Due to the very large uncertainty at $T_\infty = 450K$, a conclusion cannot be reached about the $450K$ data. For both hole shapes, the

$\Delta\phi$ between the $650K$ and $550K$ cases were within the experimental uncertainty for $550K$, so it can be said that the overall effectiveness values for the two cases collapsed to the same values as expected.

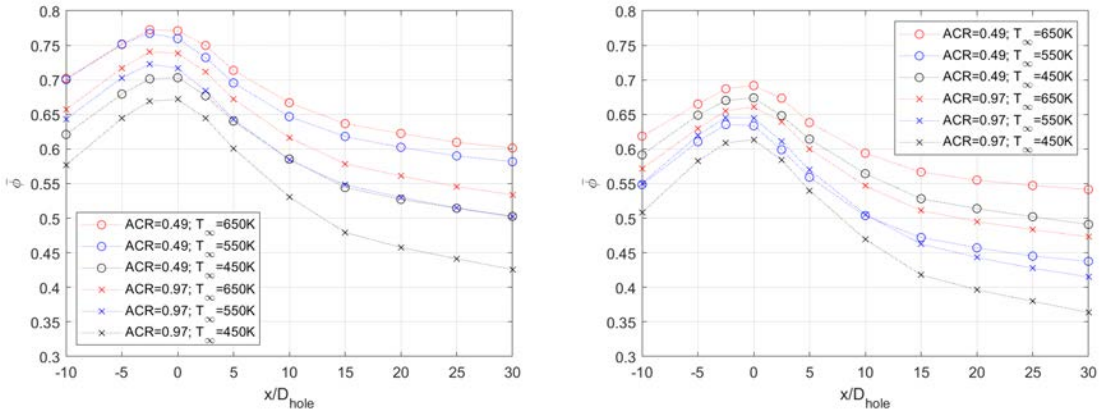

(a) $Tu \approx 2\%$ (b) $Tu \approx 10\%$

Figure 90. Effects of freestream temperature on laterally-averaged overall effectiveness versus downstream distance for the 10-10-10 hole at $Tu \approx 2\%$ and $Tu \approx 10\%$.

4.5 Internal Heat Transfer Coefficient Effects on Overall Effectiveness

This investigation simulated extra rows of film cooling holes to change the internal heat transfer coefficient within the coolant channel while holding ACR constant. The extra rows of cooling holes were simulated by increasing the coolant flow rate into the airfoil while keeping the amount of coolant flow out of the film cooling holes constant. This was done by regulating the mass flow out of the airfoil as discussed in Section 3.1. This allowed the effects of the internal heat transfer coefficient and resulting conduction within the model on overall effectiveness to be examined. Table 13 shows the resulting internal heat transfer coefficients for zero, one, and two simulated extra rows of film cooling holes. As the coolant flow rate increased due to the simulation of extra rows of holes, the temperature of the coolant inside the channel decreased due to the increased mass flow through the channel. The increased coolant flow rates

resulted in less time for heat to be transferred to the coolant and resulted in lower coolant temperatures.

Table 13. Internal heat transfer coefficients, coolant temperatures, overall effectiveness values, and resulting surface temperatures at $x/D_{hole} = 10$ for test cases with simulated extra rows of film cooling holes. Cylindrical hole, $Tu \approx 2\%$.

ACR	Simulated Extra Rows	$h_i[\frac{W}{m^2K}]$	T_∞	$T_{c,i}$ $[K]$	ϕ	$T_s[K]$
0.49	0	50.8	651	550	0.61	589
0.49	1	162	650	509	0.65	558
0.49	2	220	651	482	0.64	543
0.97	0	161	650	518	0.58	573
0.97	1	272	651	460	0.62	533
0.97	2	370	649	428	0.60	516

Figure 91 shows laterally-averaged overall effectiveness versus downstream distance for the cylindrical hole at three ACR values and $Tu \approx 2\%$ for a freestream temperature of $650K$. For $ACR = 0.49$ and $ACR = 0.97$, Figure 91 shows the resulting overall effectiveness for zero, one, and two simulated extra rows of film cooling holes. For $ACR = 1.45$, only one extra coolant row was simulated due to the limitations of the mass flow controllers. For $ACR = 0.49$, the laterally-averaged overall effectiveness for the three cases were within 0.02 of each other in the near hole region. As the downstream distance from the hole increased, the simulated extra rows caused the overall effectiveness to increase. For $ACR = 0.49$, the extra coolant flowing through the back channel caused the temperature in the back channel to decrease by about 30 degrees with each extra row. The temperatures in the back channel were $565K$, $530K$, and $506K$ for zero, one, and two extra rows of holes, respectively. The decreased temperatures and internal convection in the back channel lowered the external surface temperatures above the channel.

The increase in overall effectiveness, even with a decrease in coolant temperature, can also be attributed to the increased internal heat transfer coefficients in the front channel. Table 13 shows that increasing the internal heat transfer coefficient from

$43\frac{W}{m^2K}$ to $162\frac{W}{m^2K}$ caused ϕ to increase by approximately 0.04. Assuming an adiabatic effectiveness of 0.45 at $x/D = 5$ for a blowing ratio of 0.5 [3], Equation 49 predicted a 0.05 increase in overall effectiveness when increasing the internal heat transfer coefficient from $50.8\frac{W}{m^2K}$ for no extra rows to $162\frac{W}{m^2K}$ for one extra row. Assuming an adiabatic effectiveness of 0.55 at $x/D = 5$ for a blowing ratio of 1.0 [3], Equation 49 predicted a 0.04 increase in overall effectiveness when increasing the internal heat transfer coefficient from $161\frac{W}{m^2K}$ for no extra rows to $272\frac{W}{m^2K}$ for one extra row. Assuming an adiabatic effectiveness of 0.40 at $x/D = 5$ for a blowing ratio of 1.5 [3], Equation 49 predicted a 0.04 increase in overall effectiveness when increasing the internal heat transfer coefficient from $220\frac{W}{m^2K}$ for no extra rows to $370\frac{W}{m^2K}$ for one extra row.

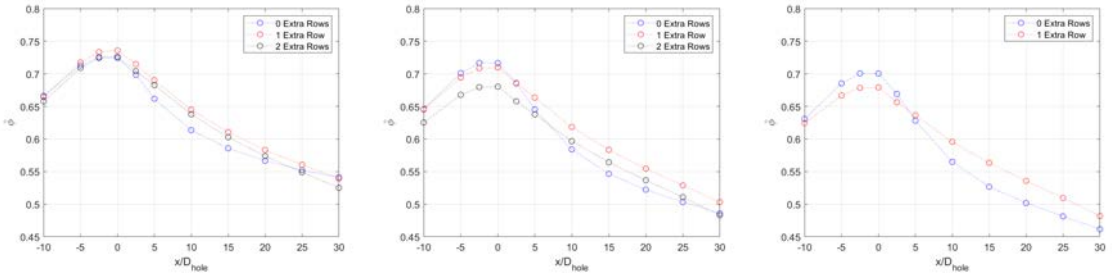

(a) $ACR = 0.49$ (b) $ACR = 0.97$ (c) $ACR = 1.45$

Figure 91. Effects of simulated extra rows of cooling holes on laterally-averaged overall effectiveness; Cylindrical Hole, $T_\infty = 650K$, $Tu \approx 2\%$.

Compared to the cases with no extra rows of cooling holes, the decay of ϕ appears almost linear after $x/D = 10$ for the cases with simulated extra rows. The back coolant channel ended at approximately $x/D = 11$, so the extra coolant in the back channel contributed to the lowered surface temperatures. The linear decay of ϕ, consistent with the linear nature of Fourier's law, is an indicator that conduction within the model was dominating the overall heat transfer. The internal convection lowered the surface temperature of the airfoil, and then the surface temperature gradually increased in a linear fashion as x/D increased. For the cylindrical hole at

$ACR = 0.49$ and $ACR = 0.97$, the laterally-averaged overall effectiveness decreased at a rate of approximately $\frac{d\phi}{dx} = -0.005$ for $x/D > 10$ for the cases with simulated extra rows of holes.

4.6 Conduction Effects Upstream of Cooling Hole

To study the effects of conduction on overall effectiveness, View 2, discussed in Section 3.3.3, was used to look at the airfoil surface upstream of the cooling holes. In a hypothetical scenario where the area upstream of the coolant channel is not affected by conduction due to the cooling channel, the surface temperatures upstream of the cooling channel would be independent of ACR. Changing the coolant flow rate would not affect the upstream surface temperatures, no matter the coolant temperature inside the channel. Labeling the upstream temperature as $T_{s,nc}$, where the subscript is defined as the surface temperature with no cooling, an alternate overall effectiveness can be defined

$$\hat{\phi} = \frac{T_\infty - T_{s,nc}}{T_\infty - T_{c,i}} \tag{52}$$

where $\hat{\phi}$ represents the overall effectiveness at the upstream location without conduction. For this investigation, $T_{s,nc}$ was assumed to be the temperature upstream of the cooling channel for $ACR = 0$ and was found to be approximately $603K$ for the 10-10-10 hole $T_\infty = 650K$ and $Tu \approx 2\%$.

For each ACR, $\hat{\phi}$ was calculated at $x/D = -16$. Due to the limitations of the new view, data from further upstream locations were not available. Table 14 lists $T_{c,i}$, and resulting $\hat{\phi}$ values for two values of ACR. As explained in Section 4.1, increasing the coolant flow rate through the channel resulted in lower coolant temperatures. As expected, decreasing the internal coolant temperature resulted in lower $\hat{\phi}$ values for a constant surface temperature.

Table 14 also compares $\hat{\phi}$ to the measured value of ϕ at $x/D = -16$. As previously

mentioned, the coolant channel started at approximately $x/D = -12$. In general, ϕ was higher than $\hat{\phi}$ for each case due to axial conduction being present in the model. As the coolant flow rate through the channel increased and the temperature in the channel decreased, the $\Delta\phi$ between ϕ and $\hat{\phi}$ increased. The decreased temperatures in the coolant channel increased the conductive heat flux from the rest of the airfoil. The increase in conductive heat flux caused the external surface temperature at $x/D = -16$ to decrease as the coolant flow rate increased even though there was no external coolant at this location and this location was not above the coolant channel.

Table 14. Coolant Temperatures, $\hat{\phi}$, and ϕ at $x/D_{hole} = -16$ for Various ACR values and $T_{s,nc} = 603K$. 10-10-10 hole, $Re_D = 10k$, $T_\infty = 650K$, $Tu \approx 2\%$

ACR	Extra Rows	$T_{c,i}$	$\hat{\phi}$	ϕ	$\Delta\phi$	T_s
0.49	0	554	0.49	0.66	0.17	587
0.49	1	521	0.37	0.63	0.26	569
0.49	2	497	0.31	0.61	0.30	557
0.97	0	531	0.39	0.60	0.21	578
0.97	1	484	0.28	0.59	0.31	552
0.97	2	451	0.24	0.57	0.33	537

4.7 Conduction Effects Downstream of Cooling Hole

The effects of conduction within the model on overall effectiveness downstream of the cooling holes were investigated by simulating extra rows of film cooling holes. Varying the mass flow through the coolant channel while keeping the mass flow out the holes constant allowed the effects of lower coolant channels on overall effectiveness to be studied for a constant ACR. Keeping ACR constant effectively kept the adiabatic effectiveness constant and allowed the effects of conduction within the model to be studied. The overall effectiveness at $x/D = 25$ for no extra rows of cooling holes was used to calculate the surface temperature at that point for each ACR. With this surface temperature labeled as $T_{s,0}$, for the surface temperature with no extra rows

of cooling holes, another alternate overall effectiveness can be defined

$$\phi' = \frac{T_\infty - T_{s,0}}{T_\infty - T_{c,i}} \tag{53}$$

where ϕ' represents the hypothetical overall effectiveness using $T_{s,0}$ and the internal coolant temperature. For cases with no simulated extra rows, $\phi' = \phi$. For a constant $T_{s,0}$, lowering the coolant temperature should result in a decreased overall effectiveness. For the 10-10-10 hole at $T_{\infty=650K}$ and $Tu \approx 2\%$, $T_{s,0}$ was approximately $591K$ and $585K$ for $ACR = 0.49$ and $ACR = 0.97$, respectively.

Table 15 shows coolant temperatures and resulting ϕ' for various ACR values. As expected, ϕ' decreased as coolant temperature decreased for a constant $T_{s,0}$. Simulating extra rows of cooling holes increased the internal heat transfer coefficient and lowered the temperatures in the channel. As described in Section 4.6, lowering the temperature in the channel increased the conductive heat flux through the airfoil. As the temperatures in the channel decreased due to increased coolant flow, the surface temperatures of the airfoil decreased due to the increased heat flux to the channel. Table 15 shows that at $ACR = 0.49$, increasing the number of simulated rows resulted in the $\Delta\phi$ between ϕ and ϕ' to increase. As previously mentioned, the coolant flow rate out the holes was kept constant, so the adiabatic effective should not change when adding extra rows of holes. As a result, any change in overall effectiveness at $x/D = 25$ would be due to conduction within the model since the coolant channel ended at $x/D \approx 11$. At $ACR = 0.97$, simulating one extra cooling row resulted in a $\Delta\phi$ between ϕ and ϕ' of approximately 0.18. Adding another extra row did not cause a further $\Delta\phi$, but the surface temperature still decreased due to the decreased temperature in the coolant channel resulting in more conductive heat flux.

Table 15. Coolant Temperatures and ϕ' at $x/D_{hole} = 25$ for Various ACR values. 10-10-10 hole, $Re_D = 10k$, $T_\infty = 650K$, $Tu \approx 2\%$

ACR	Extra Rows	$T_{c,i}$	ϕ'	ϕ	$\Delta\phi$	T_s
0.49	1	521	0.46	0.62	0.16	570
0.49	2	497	0.39	0.61	0.22	557
0.97	1	480	0.39	0.57	0.18	555
0.97	2	451	0.33	0.60	0.17	551

V. Conclusion

As technology continues to advance and turbine inlet temperatures continue to rise, cooling methods will need to constantly improve so that the turbine blades can operate in these extreme temperatures. The flow entering the high-pressure turbine is turbulent due to the upstream combustor with the turbulence intensity and length scale depending on the combustor operating condition. Overall effectiveness is commonly used to quantify the performance of a film cooling scheme. Overall effectiveness takes into account conduction within the model and evaluates the combined effectiveness of internal and external cooling methods. Understanding the effects of high freestream turbulence on overall effectiveness allows new cooling schemes to be developed that allow turbine blades to operate in increasingly extreme environments. Overall effectiveness is impacted by conduction within the model and evaluates the combined effects of internal and external cooling. Internal cooling reduces the internal temperatures of the airfoil, causing the external surface temperatures to drop due to conduction. Conduction enhances the effect of film cooling by lowering temperatures of the surface where there is no external coolant. A goal of this investigation was to understand the effects of conduction on the temperatures both within the airfoil and on the airfoil surface. The high temperatures experienced at engine conditions make evaluating cooling schemes difficult, so utilizing a true-scale turbine vane with a matched Biot number allows results to be taken at lower temperatures and then scaled up to engine conditions with the use of non-dimensional parameters. This was the process used to predict the effects of internal convection, external convection, and conduction within the model on overall effectiveness.

This investigation utilized the Film Cooling Rig (FCR) at the Air Force Institute of Technology (AFIT) to study the effects of high freestream turbulence intensity on the film cooling effectiveness of cylindrical and shaped holes. A true-scale model

with an internal serpentine channel simulated a typical turbine blade. The model was made of Inconel 718 due to the material's Biot number scaling properties. The airfoil had thermocouples on the external surface in the internal channel to track temperatures. The external surface thermocouple measurements were utilized to calibrate the radiation counts from an IR camera to obtain a map of surface temperatures. The thermocouples in the internal channel tracked the temperature of the coolant as it traveled through the channel so that the Density Ratio (DR) through the channel could be tracked. From knowledge of the freestream temperature, coolant temperature, and surface temperatures, contour plots of overall effectiveness were created over a range of operating conditions.

5.1 Objectives

This investigation focused on three objectives. The first objective was to examine the effects of high freestream turbulence intensity and turbulent length scale on the overall effectiveness of film cooling holes. The flow through turbine engines is highly turbulent so understanding the effects of turbulence intensity and length scale on cooling effectiveness is vital. The second objective was to investigate the effects of Reynolds number and freestream temperature on overall effectiveness to examine the impact that scaling has on overall effectiveness over a range of relevant Reynolds numbers and temperatures. The third objective was to examine the effects of internal convection within the coolant channel and how conduction through the model affects overall effectiveness. Understanding the effects of conduction within the model on overall effectiveness is an important step in predicting the overall effectiveness of cooling techniques in a real turbine engine.

5.2 Results and Conclusions

To fully understand the impacts of freestream turbulence intensity on overall effectiveness, it was necessary to be able to generate low levels of freestream turbulence intensity to serve as a baseline. The turbulence intensity in the FCR was measured for the first time to obtain baseline conditions in the rig. Hotwire anemometry revealed that the freestream flow entering the rig had a freestream turbulence intensity of approximately 6%. A flow straightener was designed to reduce the turbulence intensity of the freestream entering the rig. The flow straightener consisted of a honeycomb, which minimized the lateral velocity components of the flow, and a mesh that generated turbulence at small length scales. The small length scales dissipated rapidly and resulted in a turbulence intensity of $Tu \approx 2\%$ at the location of the film cooling holes. A turbulence generator consisting of a linear array of rods was chosen as the method of turbulence generation. By changing the diameter of the rods and the location of the rods relative to the airfoil, the turbulence intensity and length scale were controlled. Turbulence intensities of 5%, 10%, and 15% were achieved with various length scales. Integral length scales ranging from 6-20x the cooling hole diameter were achieved for the various turbulence intensities.

Lynch [5] sought out to investigate different hole shapes but leakage issues prevented the experiment from happening. To complete the objectives of this investigation, the airfoil cooling assembly was redesigned to solve the leakage issues experienced by Lynch [5]. The new cooling assembly consisted of an airfoil with an integrated serpentine channel, a coolant block, and an O-ring sealing the interface between the two. The flow of coolant was controlled by two mass flow controllers and a vacuum pump. The first mass flow controller was located upstream of the model and set the flow rate of coolant into the channel. The second mass flow controller was located downstream of the model and controlled the coolant flow out of the airfoil. ACR was

controlled by setting the difference in the two mass flow controllers to the required flow rate out of the holes. A vacuum pump downstream of the second mass flow controller ensured that all of the coolant did not exit the film cooling holes when flowing through the airfoil.

In this investigation, cylindrical and laidback fan-shaped holes were tested at freestream turbulence intensities of 2%, 10%, and 15% over a variety of length scales for ACR values ranging from 0 - 2. For $ACR = 0.49$, increasing the freestream turbulence intensity from $Tu \approx 2\%$ to $Tu \approx 10\%$ caused the laterally-averaged overall effectiveness, $\bar{\phi}$, of the cylindrical hole to decrease by approximately 0.05. Further increasing the turbulence intensity to $Tu \approx 15\%$ did not cause a significant decrease in $\bar{\phi}$. For $ACR = 0.49$, the 10-10-10 hole experienced a $\Delta\bar{\phi}$ of approximately -0.07 when the turbulence intensity was increased from $Tu \approx 2\%$ to $Tu \approx 10\%$ but only experienced an additional 0.02 decrease when the turbulence intensity was increased from $Tu \approx 10\%$ to $Tu \approx 15\%$. In general, increasing the freestream turbulence intensity decreased the overall effectiveness due to an increase in the external heat transfer coefficient. The 10-10-10 hole was designed to keep the coolant jet closer to the surface and resulted in higher overall effectiveness values than the cylindrical hole.

A new equation for overall effectiveness, Equation 49, was developed and includes a lateral conduction path for heat transfer. This equation was used to predict the change in overall effectiveness due to changing parameters such as the external heat transfer coefficient and internal heat transfer coefficient. Upstream of the holes, where the adiabatic effectiveness was zero, Equation 49 predicted a 0.07 decrease in overall effectiveness when increasing the external heat transfer coefficient from $110\frac{W}{m^2K}$ for $Tu \approx 2\%$ to $200\frac{W}{m^2K}$ for $Tu \approx 10\%$. Assuming an adiabatic effectiveness of 0.45 downstream of the cooling hole for a blowing ratio of 0.5 [3], Equation 49 predicted

a 0.04 decrease in overall effectiveness when increasing the external heat transfer coefficient from $110\frac{W}{m^2K}$ for $Tu \approx 2\%$ to $200\frac{W}{m^2K}$ for $Tu \approx 10\%$. The predicted changes in overall effectiveness were consistent with the experimental results.

The cylindrical hole and 10-10-10 hole were tested at freestream Reynolds numbers of $Re_D = 10k$ and $Re_D = 15k$ for freestream temperatures of $450K$, $550K$, and $650K$ to investigate the scaling of overall effectiveness between Reynolds numbers and temperature regimes. For $ACR = 0.49$ and $ACR = 0.97$ and $Tu \approx 2\%$, increasing the Reynolds number from $Re_D = 10k$ to $Re_D = 15k$ decreased the overall effectiveness by approximately 0.1 for the cylindrical hole. As with increasing turbulence intensity, increasing the Reynolds number increased the external heat transfer coefficient due to the increased freestream velocity. Equation 49 predicted a 0.06 decrease in overall effectiveness when increasing the external heat transfer coefficient from $110\frac{W}{m^2K}$ for $Re_D = 10k$ to $229\frac{W}{m^2K}$ for $Re_D = 15k$. As seen with turbulence results, increasing the external heat transfer coefficient was detrimental to overall effectiveness. For $Re_D = 10k$ and $ACR = 0.49$, the 10-10-10 hole consistently provided a 0.04 increase in overall effectiveness over the cylindrical hole. For $Re_D = 15k$ and $ACR = 0.49$, the 10-10-10 hole provided a 0.02 improvement in overall effectiveness near the cooling hole but the improvement was negligible after $x/D = 15$. The benefits of the 10-10-10 hole were minimized at $Re_D = 15k$.

At low freestream turbulence, overall effectiveness was closely matched between temperature regimes for the cylindrical and 10-10-10 hole. For the cylindrical hole at $Tu \approx 2\%$, the laterally-averaged overall effectiveness values for $ACR = 0.49$ were within 0.01 of each other for the three temperature regimes. Similarly, the laterally-averaged overall effectiveness values for $ACR = 0.49$ were within 0.02 of each other for the 10-10-10 hole at $T_\infty = 650K$ and $T_\infty = 550K$. At $ACR = 0.97$, the $\Delta\bar{\phi}$ between the $650K$ and $550K$ cases were approximately 0.02 for the cylindrical hole

and 0.04 for the 10-10-10 hole. The uncertainty in overall effectiveness was nearly 0.2 for the $450K$ cases, so the results at $T_\infty = 450K$ were inconclusive. When the freestream turbulence was increased, the overall effectiveness results did not scale well between the three temperature regimes.

To study the effects of internal convection and conduction on overall effectiveness, extra rows of film cooling holes were simulated by varying the coolant flow into the airfoil and keeping the coolant flow out of the cooling holes constant. Varying the number of simulated extra rows had the effect of varying the internal heat transfer coefficient while holding ACR constant. Lynch [5] attempted to investigate the effect of internal heat transfer coefficient on overall effectiveness but the leakage issues mentioned earlier prevented the investigation from being conducted. This investigation consisted of film cooling experiments with zero, one, and two simulated extra rows of film cooling holes. As with previous FCR experiments [4, 5, 31], this investigation saw an elevated overall effectiveness when there was no coolant flowing through the airfoil due to conduction paths through the model. For $ACR = 0$, the overall effectiveness along the surface of the airfoil was approximately 0.9 for both hole shapes due to conduction bringing the temperature of the internal channel to approximately the same temperature of the external surface. This condition had been previously dubbed the 'resting' temperature [4]. While these high ϕ values appeared to be a good quality, the actual surface temperatures were quite high and would likely melt the metal if at operating temperatures. Increasing the coolant flow rate through the channel caused the temperature inside the channel to decrease and resulted in lower coolant temperatures. The net effect was that the overall effectiveness decreased. However, these lower ϕ values produced the desired outcome of lower surface temperatures.

As the number of simulated extra rows increased for a given ACR, the mass flow rate of the coolant within the channel increased. The increased coolant flow rates

resulted in less time for heat to be transferred from the airfoil to the coolant and ultimately resulted in lower coolant temperatures. While the overall effectiveness values were close in value in the near-hole region for all three cases, the cases with extra rows produced higher overall effectiveness values as the downstream distance from the hole increased. For $ACR = 0.49$, adding one extra row of holes increased the heat transfer in the front channel from $43\frac{W}{m^2K}$ to $162\frac{W}{m^2K}$ and resulted in a 0.04 increase in ϕ at $x/D = 5$. Equation 49 predicted a 0.03 increase in overall effectiveness when increasing the internal heat transfer coefficient from $40\frac{W}{m^2K}$ to $162\frac{W}{m^2K}$, assuming an adiabatic effectiveness of 0.45 for a blowing ratio of 0.5 [3].

Unlike the cases with no extra rows of holes, the cases with extra rows had coolant flow in the back channel. The flow of coolant through the back channel resulted in more heat being transferred from the channel walls to the coolant, resulting in lower channel temperatures. For the cylindrical hole at $ACR = 0.49$, the extra coolant flowing through the back channel caused the temperature in the back channel to decrease from $565K$ to $530K$ to $506K$ for zero, one, and two extra rows of holes, respectively. The decreased temperatures in the back channel resulted in more heat being conducted from the airfoil's external surface to the channel and lowered the external surface temperatures above the channel from $573K$ to 543 to $524K$.

Comparing plots of laterally-averaged overall effectiveness versus downstream distances for the three cases revealed that the $\bar{\phi}$ decay for $x/D_{hole} > 10$ appeared linear for the cases with simulated extra rows of holes. For the cylindrical hole at $ACR = 0.49$ and $ACR = 0.97$, the laterally-averaged overall effectiveness decreased at a rate of approximately $\frac{d\phi}{dx} = -0.005$ for $x/D > 10$. The linear decay was an indication that conduction through the model was the dominating mode of heat transfer. The increased mass flow through the channel caused the temperature of the channel to decrease and created a large temperature gradient through the model.

Conduction within the FCR had a negative impact on the temperature of the coolant and as a result, had a negative impact on the density of the coolant. Although the density of the coolant was around twice the density of the freestream just 70.3 mm away from the coolant inlet, the coolant heated up rapidly once it entered the airfoil. For cases with $T_\infty = 650K$, the coolant heated up from $314K$ just outside the airfoil to $550K$ in the internal channel. This resulted in the density of the coolant to dramatically decrease in the short distance between the two measurement locations. In real turbine engines, the density of the coolant entering the holes is likely significantly lower than the density at the beginning of the coolant line.

5.3 Future Work

The scope of this investigation was limited by the temperature capability of the facility. Future work should perform similar experiments at temperatures closer to that of a typical turbine engine to examine how the results of this investigation scale up to near-engine conditions. The heating capabilities of the FCR may not allow near engine conditions to be reached, so the next step may be transitioning to a high-temperature facility. Higher freestream temperatures would also lower the uncertainty in overall effectiveness by increasing the difference between the temperatures of the coolant and freestream. Performing experiments at near-engine conditions would reduce the importance of chilling the coolant and insulating the coolant line to achieve typical density ratios found in a turbine engine.

The flow straightener successfully reduced the freestream turbulence intensity in the FCR, but the turbulence intensity was still around 2%. When conducting the literature review, it was common to see turbulence intensities equal to or less than $Tu \approx 1\%$ for the low freestream turbulence cases. A new flow straightener that allows the number of honeycombs and mesh grids to be varied could allow the baseline level

of freestream turbulence intensity to be lowered.

The new equation for overall effectiveness which includes lateral conduction allowed an additional conduction path within the model to be accounted for. While this allowed changes in overall effectiveness to be predicted, there are several more conduction paths that affect overall effectiveness. A computational study may be required to fully understand the effects of conduction within the model on overall effectiveness. A computational analysis of a true-scale conductive model could examine the resting overall effectiveness at different freestream temperatures when there is no coolant flow within the airfoil. The study could also investigate the effects of increasing ACR on overall effectiveness for comparison with the results of this investigation.

While the new equation for overall effectiveness demonstrated the impact of additional conduction paths on overall effectiveness, additional experimental testing is needed to fully understand why ϕ decreased with ACR. Due to its non-dimensional nature, overall effectiveness should not be a function of coolant temperature. Future experiments should experimentally determine values of $\frac{L_1}{L_2}$ at various ACR to obtain $\phi = \psi$. Doing so could remove the effect of additional conduction paths and correct ϕ in such a way that it is no longer a function of coolant temperature.

Bibliography

1. Meher-Homji, C. B., "The Development of the Junkers JUMO 004B: The World's First Production Turbojet," V002T02A012, Birmingham, UK, 1996.

2. Eberly, M. K. and Thole, K. A., "Time-Resolved Film-Cooling Flows at High and Low Density Ratios," *Journal of Turbomachinery*, Vol. 136, No. 6, 2014, pp. 061003.

3. Bogard, D. G. and Thole, K. A., "Gas Turbine Film Cooling," *Journal of Propulsion and Power*, Vol. 2, No. 2, 2008, pp. 249–270.

4. Vorgert, C. J., "Relating Film Cooling Performance Between Ambient and Near Engine Temperatures," Master's Thesis, Air Force Institute of Technology, 2017.

5. Lynch, R. A., "Investigation of Thermal Scaling Effects for a Turbine Blade Leading Edge and Pressure Side Model," Master's Thesis, Air Force Institute of Technology, 2019.

6. Bergman, T., Lavine, A., Incropera, F., and Dewitt, D., *Fundamentals of Heat and Mass Transfer*, Wiley, 7th ed., 2011.

7. Bryant, C. E., Wiese, C. J., Rutledge, J. L., and Polanka, M. D., "Experimental Evaluations of the Relative Contributions to Overall Effectiveness in Turbine Blade Leading Edge Cooling," *Journal of Turbomachinery*, Vol. 141, No. 4, 2018, pp. 041007.

8. Rutledge, J. L., Polanka, M. D., and Bogard, D. G., "The Delta Phi Method of Evaluating Overall Film Cooling Performance," *Journal of Turbomachinery*, Vol. 138, No. 7, 2016, pp. 071006.

9. Albert, J. E. and Bogard, D. G., "Measurements of Adiabatic Film and Overall Cooling Effectiveness on a Turbine Vane Pressure Side With a Trench," *Journal of Turbomachinery*, Vol. 135, No. 5, 2013, pp. 051007.

10. Thole, K., Sinha, A., Bogard, D., and Crawford, M., "Mean temperature measurements of jets with a crossflow for gas turbine film cooling application," *Third International Symposium on Transport Phenomena and Dynamics of Rotating Machinery (ISROMAC-3)*, , No. January 1992, pp. 69–86.

11. Rutledge, J. L. and Polanka, M. D., "Computational Fluid Dynamics Evaluations of Unconventional Film Cooling Scaling Parameters on a Simulated Turbine Blade Leading Edge," *Journal of Turbomachinery*, Vol. 136, No. 10, 2014, pp. 101006.

12. Wiese, C. J., Bryant, C. E., Rutledge, J. L., and Polanka, M. D., "Influence of Scaling Parameters and Gas Properties on Overall Effectiveness on a Leading Edge Showerhead," *Journal of Turbomachinery*, Vol. 140, No. 11, 2018, pp. 111007.

13. Fischer, J. P., Rutledge, J. L., McNamara, L. J., and Polanka, M. D., "Scaling Flat Plate, Low Temperature Adiabatic Effectiveness Results Using The Advective Capacity Ratio," *ASME Turbo Expo*, GT2019-90997, Phoenix, Arizona, USA, 2019, pp. 1–13.

14. Polanka, M. D., Rutledge, J. L., Bogard, D. G., and Anthony, R. J., "Determination of Cooling Parameters for a High-Speed, True-Scale, Metallic Turbine Vane," *Journal of Turbomachinery*, Vol. 139, No. 1, 2016, pp. 011001.

15. Gritsch, M., Schulz, A., and Wittig, S., "Adiabatic Wall Effectiveness Measurements of Film-Cooling Holes With Expanded Exits," *Journal of Turbomachinery*, Vol. 120, No. 3, 1998, pp. 549.

16. Schroeder, R. P. and Thole, K. A., "Adiabatic Effectiveness Measurements for a Baseline Shaped Film Cooling Hole," *ASME Turbo Expo*, Vol. 5b, GT2014-25992, Düsseldorf, Germany, 2014.

17. Hayes, S. A., Nix, A. C., Nestor, C. M., Billups, D. T., and Haught, S. M., "Experimental Investigation of the Influence of Freestream Turbulence on an Anti-Vortex Film Cooling Hole," *Experimental Thermal and Fluid Science*, Vol. 81, 2017, pp. 314–326.

18. Haven, B. A., Yamagata, D. K., Kurosaka, M., Yamawaki, S., and Maya, T., "Anti-Kidney Pair of Vortices in Shaped Holes and Their Influence on Film Cooling Effectiveness," *ASME Turbo Expo*, Vol. 3, 97-GT-045, Orlando, Florida, 1997, pp. 1–8.

19. Heidmann, J. D. and Ekkad, S., "A Novel Antivortex Turbine Film-Cooling Hole Concept," *Journal of Turbomachinery*, Vol. 130, No. 3, 2008, pp. 031020.

20. Dhungel, A., Lu, Y., Phillips, W., Ekkad, S. V., and Heidmann, J., "Film Cooling From a Row of Holes Supplemented With Antivortex Holes," *Journal of Turbomachinery*, Vol. 131, No. 2, 2009.

21. Ames, F. and Moffat, R., "Effects of Simulated Combustor Turbulence on Boundary Layer Heat Transfer," *AIAA/ASME Thermophysics and Heat Transfer Conference*, Seattle, Washington, 1990, pp. 11–17.

22. Cameron, C., Brouwer, J., Wood, C., and Samuelson, G., "A Detailed Characterization of the Velocity and Thermal Fields in a Model Can Combustor with Wall Jet Injection," *Journal of Engineering for Gas Turbines and Power*, Vol. 111, 1989, pp. 31–35.

23. Pope, S. B., *Turbulent Flows*, Cambridge University Press, 1st ed., 2000.

24. Schmidt, D. L. and Bogard, D. G., "Effects of Free-Stream Turbulence and Surface Roughness on Film Cooling Effectiveness," *ASME Turbo Expo*, Vol. 4, 96-GT-462, Birmingham, UK, 1996, pp. 1–7.

25. Baines, P. and Peterson, E., "An Investigation of Flow Through Screens," *Transactions of the American Society of Mechanical Engineers*, Vol. 73, No. 50-A-23, 1951, pp. 467–480.

26. Roach, P. E., "The Generation of Nearly Isotropic Turbulence By Means of Grids," , No. July, 1986, pp. 82–92.

27. Loehrke, R. I. and Nagib, H. M., "Control of Free-Stream Turbulence by Means of Honeycombs: A Balance Between Suppression and Generation," *Journal of Fluids Engineering*, Vol. 98, No. 3, 2010, pp. 342–353.

28. West, T., *The Ultimate Infrared Handbook for Research and Development Professionals*, FLIR Systems Incorporated, Portland, 2012.

29. Modest, M., *Radiative Heat Transfer*, Academic Press, 3rd ed., 2013.

30. Martiny, M., Schiele, R., Gritsch, M., Schulz, A., and Wittig, S., "In Situ Calibration For Quantitative Infrared Thermography," *QIRT*, 1997.

31. Tewaheftewa, J. T., "Investigation of Geometric and Thermal Scaling Effects on a Simulated Turbine Vane Leading Edge Model," Master's Thesis, Air Force Institute of Technology, 2018.

32. Dantec, *How to measure turbulence with hot-wire anemometers - a practical guide*, 2002.

33. Nickol, J., Mathison, R., Dunn, M., Liu, J., and Malak, M., "An Investigation of Coolant Within Serpentine Passages of a High-Pressure Axial Gas Turbine Blade," *Journal of Turbomachinery*, 2017.

34. Roach, P. E., "The Generation of Nearly Isotropic Turbulence by Means of Grids," *International Journal of Heat and Fluid Flow*, Vol. 8, No. 2, 1987, pp. 82–92.

35. Rathsack, T. C., "Examination of Flow Dynamics and Passive Cooling in an Ultra Compact Combustor," Master's Thesis, Air Force Institute of Technology, 2019.

36. Gritsch, M., Schulz, A., and Wittig, S., "Discharge Coefficient Measurements od Film-Cooling Holes With Expanded Exits," *Journal of Turbomachinery*, Vol. 120, No. 3, 1998, pp. 557–563.

37. Kays, W., Crawford, M., and Weigand, B., *Convective Heat and Mass Tramsfer*, McGraw-Hill, 4th ed., 2005.

38. Moffat, R. J., "Describing the Uncertainties in Experimental Results," *Experimental Thermal and Fluid Science*, Vol. 1, No. 1, 1988, pp. 3–17.

REPORT DOCUMENTATION PAGE

Form Approved
OMB No. 0704–0188

The public reporting burden for this collection of information is estimated to average 1 hour per response, including the time for reviewing instructions, searching existing data sources, gathering and maintaining the data needed, and completing and reviewing the collection of information. Send comments regarding this burden estimate or any other aspect of this collection of information, including suggestions for reducing this burden to Department of Defense, Washington Headquarters Services, Directorate for Information Operations and Reports (0704–0188), 1215 Jefferson Davis Highway, Suite 1204, Arlington, VA 22202–4302. Respondents should be aware that notwithstanding any other provision of law, no person shall be subject to any penalty for failing to comply with a collection of information if it does not display a currently valid OMB control number. **PLEASE DO NOT RETURN YOUR FORM TO THE ABOVE ADDRESS.**

1. REPORT DATE *(DD–MM–YYYY)*	2. REPORT TYPE	3. DATES COVERED *(From — To)*
26-03-2020	Master's Thesis	Sept 2018 — Mar 2020

4. TITLE AND SUBTITLE

EFFECTS OF HIGH FREESTREAM TURBULENCE AND CONDUCTION ON FILM COOLING EFFECTIVENESS OF SHAPED HOLES

5a. CONTRACT NUMBER

5b. GRANT NUMBER

5c. PROGRAM ELEMENT NUMBER

6. AUTHOR(S)

Macias, Richard A., Second Lieutenant, USAF

5d. PROJECT NUMBER

5e. TASK NUMBER

5f. WORK UNIT NUMBER

7. PERFORMING ORGANIZATION NAME(S) AND ADDRESS(ES)

Air Force Institute of Technology
Graduate School of Engineering and Management (AFIT/EN)
2950 Hobson Way
WPAFB OH 45433-7765

8. PERFORMING ORGANIZATION REPORT NUMBER

AFIT-ENY-MS-20-M-270

9. SPONSORING / MONITORING AGENCY NAME(S) AND ADDRESS(ES)

Richard J. Anthony DR-03 USAF AFMC AFRL/RQTT
1950 Fifth Street
WPAFB, OH 45433
(937) 255-6768
Email: richard.anthony.4@us.af.mil

10. SPONSOR/MONITOR'S ACRONYM(S)

AFRL

11. SPONSOR/MONITOR'S REPORT NUMBER(S)

12. DISTRIBUTION / AVAILABILITY STATEMENT

DISTRIBUTION STATEMENT A:
APPROVED FOR PUBLIC RELEASE; DISTRIBUTION UNLIMITED.

13. SUPPLEMENTARY NOTES

14. ABSTRACT

This investigation studied overall effectiveness for a cylindrical hole and a laidback fan-shaped hole over a range of coolant flow rates and freestream turbulence intensities. Increasing the turbulence intensity resulted in lower overall effectiveness values due to increased heat transfer coefficients. Increasing Reynolds number also decreased the overall effectiveness due to the increased external heat transfer coefficient. Increasing the internal heat transfer coefficient resulted in increased overall effectiveness due to lower temperatures in the coolant channel drawing heat from the external surface. Increasing the coolant flow rate resulted in lower airfoil temperatures upstream and downstream of the channel due to an increase in conductive heat flux through the airfoil. Conduction in the rig caused the temperature of the coolant to dramatically increase within a short distance. This implies that in a turbine engine, the density of the coolant entering the cooling holes is significantly lower than the density in the coolant line.

15. SUBJECT TERMS

Film Cooling, Turbine, Turbulence

16. SECURITY CLASSIFICATION OF:			17. LIMITATION OF ABSTRACT	18. NUMBER OF PAGES	19a. NAME OF RESPONSIBLE PERSON
a. REPORT	b. ABSTRACT	c. THIS PAGE			Dr. Marc D. Polanka, AFIT/ENY
U	U	U	U	146	19b. TELEPHONE NUMBER *(include area code)* (937) 255-3636, x4714; marc.polanka@afit.edu